PLANAR PEROVSKITE SOLAR CELLS WITH METAL OXIDE TRANSPORT LAYERS BY CO-EVAPORATION AND HYBRID VAPOR-SOLUTION SEQUENTIAL METHOD

A THESIS SUBMITTED TO
THE GRADUATE SCHOOL OF NATURAL AND APPLIED SCIENCES
OF
MIDDLE EAST TECHNICAL UNIVERSITY

BY

WIRIA SOLTANPOOR

IN PARTIAL FULFILLMENT OF THE REQUIREMENTS
FOR
THE DEGREE OF DOCTOR OF PHILOSOPHY
IN
MICRO AND NANOTECHNOLOGY

FEBRUARY 2020

Approval of the thesis:

PLANAR PEROVSKITE SOLAR CELLS WITH METAL OXIDE TRANSPORT LAYERS BY CO-EVAPORATION AND HYBRID VAPOR-SOLUTION SEQUENTIAL METHOD

submitted by **WIRIA SOLTANPOOR** in partial fulfillment of the requirements for the degree of **Doctor of Philosophy** i**n Micro and Nanotechnology, Middle East Technical University** by,

Prof. Dr. Halil Kalıpçılar
Dean, Graduate School of **Natural and Applied Sciences** _____

Prof. Dr. Almıla Güvenç Yazıcıoğlu
Head of the Department, **Micro and Nanotechnology** _____

Assist. Prof. Dr. Selçuk Yerci
Supervisor, **Micro and Nanotechnology, METU** _____

Assoc. Prof. Dr. Görkem Günbaş
Co-Supervisor, **Chemistry, METU** _____

Examining Committee Members:

Prof. Dr. Hüsnü Emrah Ünalan
Metallurgical and Material Eng, METU _____

Assist. Prof. Dr. Selçuk Yerci
Micro and Nanotechnology, METU _____

Prof. Dr. Ali Çırpan
Chemistry, METU _____

Assist. Prof. Dr. Talip Serkan Kasırga
Physics, Bilkent University _____

Assoc. Prof. Dr. Sinan Balcı
Photonics, İYTE _____

Date: 12.02.2020

I hereby declare that all information in this document has been obtained and presented in accordance with academic rules and ethical conduct. I also declare that, as required by these rules and conduct, I have fully cited and referenced all material and results that are not original to this work.

Name, Last name: Wiria Soltanpoor

Signature:

ABSTRACT

PLANAR PEROVSKITE SOLAR CELLS WITH METAL OXIDE TRANSPORT LAYERS BY CO-EVAPORATION AND HYBRID VAPOR-SOLUTION SEQUENTIAL METHOD

Soltanpoor, Wiria
Doctor of Philosophy, Micro and Nanotechnology
Supervisor: Assist. Prof. Dr. Selçuk Yerci
Co-Supervisor: Assoc. Prof. Dr. Görkem Günbaş

February 2020, 94 pages

The recent success in achieving beyond 25% efficiency with perovskite solar cells (PSC) has called for further upgrading the fabrication techniques to meet the scalability requirements of the photovoltaic (PV) industry. Co-evaporation and a hybrid vapor-solution technique have been shown to produce uniform and efficient planar PSCs. Therefore, in this study, co-evaporation method was optimized studying the partial pressure of the organic precursor. Later electron transport layers in n-i-p and p-i-n structures were addressed achieving 13.0% and 16.1% efficiencies, respectively. Besides, mixed-halide perovskites were fabricated following a hybrid sequential method focusing on the deposition rate of PbI_2 and a solution of methylammonium-halides to control the crystallization and morphology of the perovskite layer. This conferred efficiencies up to 19.8% in the case of $MAPbI_{3-X-Y}Br_XCl_Y$ with 90 hours of operational stability. This is an important measure towards scalability due to the uniform deposition of the first inorganic layer by vacuum-deposition. As another step towards the scalability of perovskite PV, radio frequency (RF) magnetron sputtering was devised to deposit NiO_X as a hole transport layer with

wide bandgap, matched band structure with perovskite, and stability. The effect of Ar-partial pressure, deposition rate on the optoelectronic properties of the sputtered NiO_X was investigated. The passivation of NiO_X using organic (Poly-TPD) and inorganic (CuO) materials boosted the overall efficiency of the PSCs by 2.2% and 1.2%, respectively. Finally, Cu doping NiO_X via co-sputtering enhanced the efficiency of the PSCs by 3%. This thesis provides a benchmark for applying scalable methods (from evaporation to sputtering) towards efficient PSCs.

Keywords: Perovskite, Co-evaporation, Partial pressure, Sputtering, Hybrid vapor solution

ÖZ

BIRLIKTE BUHARLAŞTIRMA VE HIBRIT BUHAR ÇÖZELTISI SIRALI YÖNTEMI ILE METAL OKSIT DELIK (HOLE) TAŞIMA KATMANLI DÜZLEMSEL PEROVSKIT GÜNEŞ HÜCRELERI

Soltanpoor, Wiria
Doktora, Mikro ve Nanoteknoloji
Tez Yöneticisi: Dr. Öğr. Üyesi Selçuk Yerci
Ortak Tez Yöneticisi: Doç. Dr. Görkem Günbaş

Şubat 2020, 94 sayfa

Perovskit güneş hücrelerinde yakın zamanda gösterilen %25'in üzerinde verimlilik elde etme başarısı, fotovoltaik (FV) endüstrisinin ölçeklenebilirlik gereksinimlerini karşılamak için imalat tekniklerini daha da geliştirmeyi gerektirdi. Birlikte buharlaştırma ve hibrit buhar çözeltisi tekniklerinin, düzgün ve verimli düzlemsel perovskit güneş hücreleri ürettiği gösterilmiştir. Bu sebeple, bu çalışmada, organik öncü maddenin kısmi basıncı çalışılarak, birlikte buharlaştırma metodu optimize edilmiştir. Daha sonra, n-i-p ve p-i-n yapılarındaki elektron taşıyıcı katmanlar araştırılarak %13,0 ve %16,1 verime sahip hücreler elde edilmiştir. Öte yandan, hibrit buhar çözeltisi metodu ile karışık halojenür perovskitler üretilmiş ve perovskit katmanının kristalleşme oranı ve morfolojisini kontrol etmek için PbI_2'nin kaplanma oranı ve metilamonyum halojenürün çözülme oranına odaklanılmıştır. Bu yöntem $MAPbI_{3-X-Y}Br_XCl_Y$ kulanılma durumunda %19,8 verimlilik ve 90 saatlik operasyonel kararlılıkla sonuçlanmıştır. Bu, ilk inorganik katmanın vakum biriktirme yöntemiyle homojen biriktirilmesinden dolayı ölçeklenebilirliğe yönelik önemli bir ölçüdür. Perovskit FV'nin ölçeklenebilirliğine bir başka adım olarak, geniş bant aralıklı ve perovskit ile eşleşen bant yapısıyla kararlı bir boşluk taşıma

katmanı olarak NiO_X'u kaplamak için radyo frekansı (RF) magnetron saçtırma yöntemi kullanılmıştır. Ar-kısmi basınç, birikme hızı ve Cu katkılamanın saçtırma ile büyütülmüş NiO_X'un optoelektronik özellikleri üzerindeki etkisi araştırılmıştır. NiO_X'un organik (Poli-TPD) ve inorganik (CuO) materyalleri kullanılarak pasive edilmesi perovskit güneş hücrelerinin verimliliklerini sırasıyla %2,2 ve %1,2 artırmıştır. Son olarak, birlikte saçtırma kullanılarak Cu katkılı NiO_X katmanı ile üretilen perovskit hücrelerinin verimlilikleri %3 iyileştirilmiştir. Bu tez yüksek verimli perovskit FV'lere yönelik ölçeklenebilirlik uygulamaları açısından (buharlaştırmadan saçtırmaya) bir referans ölçütü sağlamaktadır.

Anahtar Kelimeler: Perovskit, Birlikte buharlaştırma, Kısmi basınc, Saçtırma, Hibrit buhar çözeltisi

To my family

ACKNOWLEDGMENTS

I am really grateful to my Supervisor Asst. Prof. Dr. Selçuk Yerci for his kind understandings, critical guidance, zeal in high-quality research, endeavor for financial support, kindly exposing me to up-to-date international conferences and especially providing for my scientific visit to ICMol in the University of Valencia. His patience and energy made my transition possible from the theoretical studies to the experimental sciences.

I fully appreciate my co-advisor Assoc. Prof. Dr. Görkem Günbaş for his scientific feedbacks on chemistry, and his immediate support to provide required chemicals and practical resolutions. I appreciate his reputation to have a profound insight into the chemistry and the synthesis of materials.

I would like to offer my deepest gratitude to Prof. Dr. Henk J. Bolink for professional guidance and friendly support. I highly appreciate his nominal efficiency in scientific leadership and his kind confidence in me. I conducted my studies on the hybrid vapor-solution sequential method in his lab in ICMol.

I feel indebted to Prof. Dr. Raşit Turan for his fatherly support to supply the infrastructure for solar cell investigations, trusting me and other researchers to lead their studies. His endeavor to extend the photovoltaics in both lab-scale and industry-scale is invaluable.

I would like to thank all the past and current helpful members of APP and METU-Perovskite team including Wisnu Hadibrata for his training, Irem Özyurt, Onur Yılmaz, Arman Ayan, Can Özcan, Deniz Türkay, Damla Koçak, Umut Bekci, Dr. Mohsen Ameri, Bahri Eren Uzuner, Kerem Artuk, Naser Beyraghi, Necati Işık, Muhammet Mustafa Çodur, Buse Ünlü, Elif Cüce, Esra Bağ, Gizem Atakan, Gülsüm Güneş, Merve Derya Oflaz, Elif Kirdeciler, Figen Varlıoglu, and Zeynep Gözükara.

I offer my heartfelt gratitude to Gence Bektaş as a caring friend who stood by me day and night during experiments and characterizations, especially with long processes of p-i-n perovskite solar cells with sputtered NiO_X. He is a paragon of a true and workaholic scientist who is there to help rain or shine.

I am grateful to my friend Mehmet Koç who kindly taught me a lot of Optics. His intelligence and interest in problem-solving and caring attitude always motivated me. His kind character makes him a blessing to any community.

I am so thankful to my great friend Ilker Yıldız for being a kind and hardworking teammate in UPS/XPS studies. I appreciate his help in the characterizations of thin films.

I fully appreciate Mehmet Cem Şahiner as a friend and a lab mate who taught me chemistry. His deep knowledge in device physics, electronic systems and designs was merit for me. His impact on my studies on co-evaporation and hybrid vapor-solution method is unforgettable.

I would like to thank my friend Milad Ghasemi for his dedicated help in NiO_X sputtering and his positive attitude as a teammate. I fully appreciate his kind support during my foreign scientific visit.

I should thank Amir Zarean for his nonstop assistance in the perovskite lab. I appreciate his efforts in helping with fabrications and characterizations.

I am thankful to Dr. Hava Kaya for her kind support, useful comments, and cooperation during the experiments. I really appreciate her kind care for her teammates.

I am grateful to Konstantin Tsoi who helped with useful MATLAB code writing. This saved a lot of my time with data interpretations.

I would like to thank Salar Habibpur Sedani, Dr. Behzad Hoseini, and Mona Borra for their true friendship during my stay in Turkey. Salar trained me in Raman

spectroscopy and Mona gave training in AFM. My words are not enough to express my gratitude to Behzad and Salar who helped me get settled in Turkey.

I am grateful to Mustafa Unal for my training in EDX, his technical and scientific discussions. His positive attitude, contribution, and care reflect his true friendship.

I would like to thank Dr. Mete Gunoven for his patience and delicate with my training in EQE and UV-VIS spectroscopy.

I thank Hande Emine çiftpınar, Ergi Dönerçark, and Dr. Makbule Terlemezoglu for their kind support as great friends.

I should thank Murat Öztürk for his time and dedication to PL measurements and setup.

I also thank Dr. Bülent Arıkan for his very kind technical advice on materials and equipment. He was always there to help with lab supplies.

I need to thank Dr. Fırat Es and Dr. Hisham Nasser for their fruitful scientific discussions and help. Fırat trained me for cleanroom, HF and RCA cleaning procedures. Hisham gave me training in Ellipsometry and helped with SEM.

I would like to thank Dr. Arezoo Hosseini who trained me in spin-coating perovskite layer in a two-step fashion.

I would like to thank Dr. Pablo P. Boix for his patience and useful instructions during my stay in ICMol, Valencia. I appreciate his encouragement to follow my research themes.

I would like to thank Dr. Michele Sessolo and Azin Babaei for their confidence in me and their kind support.

I should thank Dr. Vahid Fallah Hamidabadi for his warm welcome and helping me settle in Valencia.

I would like to thank Jorge Ferrando as a nice friend and a professional technician who helped us in the kindest way possible.

I would like to thank Daniel Perez del Ray for his training in ICMol and a very kind company.

I should thank Dr. Vladimir S Chirvony for his useful instructions and attentive PL characterizations of perovskite layers.

I am so thankful to Dr. Francisco Palazon, Dr. Maria Monrabal, Dr. Lidon Gil-Escrig, Isidora Susic, Chris Dreessen, Dr. Kassio PS Zanoni, Ana M Igual-Muñoz, Laura Martínez-Sarti, Yousra El Ajjouri, and all the other scientists and friends in ICMol for their kind company and help.

I am so grateful to Prof. Dr. Hüsnü Emrah Ünalan for his priceless instructions and constructive criticisms throughout my Ph.D. dissertation studies.

I should thank Prof. Dr. Alpan Bek for his instructions on optics and AFM. I fully appreciate his positive encouraging attitude.

I appreciate the lessons I learned during the course taught by Prof. Dr. Burcu Akata Kurç, Prof. Dr. Nizami Hasanli, Asst. Prof. Dr. Selçuk Yerci, Prof. Dr. Hüsnü Emrah Ünalan, and Prof. Dr. Raşit Turan.

I would like to thank Prof. Dr. Mehmet Parlak for his attentive care for the cleanroom equipment and XRD maintenance. I appreciate his help to me and other students.

I need to thank Dr. Gönül Hızalan for her kind help and trust in the organic lab.

I would like to thank the nice staff of METU Central Laboratory especially Kaan Kirdeciler. and Sedat Canlı for their technical and meticulous help in SEM. I also thank Seçkin Öztürk and Pelin Paşabeyoğlu for their patience with accurate measurements.

I am thankful to Behrad Radfar, Asst. Prof. Dr. Hasan Hüseyin Güllü, Gamze kökbudak, Emre Demirezen, Yasin Ergunt, and all the other kind members of GÜNAM who kindly helped me during my studies in METU.

I appreciate Yucel Eke as a great technician and artist dedicated to help with the lab maintenance and to modify the equipment all the time.

I would like to thank the technicians in GÜNAM including Tayfun and Nevzat to help me in need.

The financial support was received from the Scientific and Technological Research Council of Turkey (TÜBITAK) under contract numbers of 213M761 and 315M360.

I have to express my sincere gratitude to my parents Saleh and Parizad for their love and warm unconditional support throughout my education and all aspects of my life. I should thank my brother Aria and my sister Zhina as the greatest friends from whom I received nothing but care and help. I feel indebted to my uncles Saeed and Aza for their help and love during hardships. My achievements would not have been possible without the company of my life mate Zeinab Eftekhari who supported me with a kind heart and great love.

TABLE OF CONTENTS

ABSTRACT v

ÖZ vii

ACKNOWLEDGMENTS x

TABLE OF CONTENTS xv

LIST OF TABLES xvii

LIST OF FIGURES xviii

LIST OF ABBREVIATIONS xxii

LIST OF SYMBOLS xxv

CHAPTERS

1 INTRODUCTION 1

1.1 Global warming and photovoltaics 1

1.2 Perovskite solar cells 5

1.3 Thesis outline 8

2 LARGE AREA CO-EVAPORATED PEROVSKITE SOLAR CELLS WITH OPTIMIZED ELECTRON TRANSPORT LAYERS 9

2.1 Co-evaporated perovskite solar cells 10

2.1.1 n-i-p structure perovskite solar cells using the optimized deposition parameters 13

2.1.2 $TiCl_4$ treatment of TiO_2 16

2.1.3 Bilayer of TiO_2 17

2.1.4 p-i-n perovskite solar cells 20

2.1.5 Large area perovskite solar cells 24

3 HYBRID VAPOR-SOLUTION SEQUENTIALLY DEPOSITED MIXED-HALIDE PEROVSKITE SOLAR CELLS 27
3.1 Hybrid vapor-solution sequential deposition 27
3.2 Results and Discussion 30
3.2.1 PbI_2 layer 30
3.2.2 Device fabrication 36
3.2.3 The effect of Br^- and Cl^- and their combination 39
3.3 Conclusions 50
4 SPUTTERED INTRINSIC AND DOPED NIO_X HOLE TRANSPORT LAYERS FOR PLANAR PEROVSKITE SOLAR CELLS 53
4.1 Introduction 53
4.2 Results and Discussions 55
4.2.1 Post-treatment of NiO_X and prerequisites 55
4.2.2 The effect of the deposition rate of NiO_X 59
4.2.3 The effect of Ar-partial pressure 62
4.2.4 Inorganic passivation of NiO_X 69
4.2.5 Doping NiO_X with Cu by co-sputtering 73
4.3 Conclusions 78
5 CONCLUSIONS AND OUTLOOKS 79
REFERENCES 83
CURRICULUM VITAE 93

LIST OF TABLES

TABLES

Table 2-1 The FWHM of the (110) crystal plane of MAPI-Cl shown in Figure 2-2b. 12
Table 2-2 The resultant average and best J-V characteristics following different times of $TiCl_4$ treatment. 17
Table 2-3 Summarized average and best-cell J-V characteristic data for the perovskite solar cells made of TiO_2 using different TTIP solution concentrations and sequences. 19
Table 2-4 Average and best (in parenthesis) J-V characteristic data for p-i-n perovskite solar cells with different NiO_X thicknesses. 21
Table 2-5 The average and best (in parenthesis) data for J-V characteristic data for perovskite solar cells with different C_{60} thicknesses. 23
Table 2-6 The J-V characteristic data measured in the reverse and forward scan for the best working perovskite solar cells with different active areas. 26
Table 3-1 J–V parameter values for the best devices corresponding to Figure 3-5e. 39
Table 3-2 The performance details corresponding to Figure 3-7d. 44
Table 4-1 Average J-V characteristic values for perovskite solar cells fabricated using NiO_X deposited under 2 and 4 mTorr of APP. 69
Table 4-2 Forward and reverse J-V data for the best cells presented in Figure 4-10e. 78

LIST OF FIGURES

FIGURES

Figure 1-1.1 The yearly amount of CO_2 in units of parts per million in the atmosphere. 2
Figure 1-2. The electricity supply of the world and their sources. 3
Figure 1-3 a) NREL efficiency chart for the emerging PV, b) NREL efficiency chart for perovskite and perovskite/Si tandem solar cells. 4
Figure 1-4 The structure of ABX_3 perovskite. 5
Figure 2-1 a) The vacuum chamber for co-evaporation of $PbCl_2$ (green cone) and MAI (yellow circles) which scatter around the chamber, b) MAI vapor pressure and deposition rate. 11
Figure 2-2 a) X-ray diffractograms for co-evaporated perovskite films under different MAI partial pressures, b) the (110) plane diffraction of the MAPI-Cl annealed in the air for different periods. 12
Figure 2-3 a) SEM image of the MAPI-Cl sample deposited under 5×10^{-5} Torr of MAI partial pressure and annealed for 30 minutes in the air, b) the absorbance (red) and photoluminescence spectra (blue) of the sample in (a). 13
Figure 2-4 a) GIXRD patterns measured at 0.3° incidence for FTO/TiO_2 deposited using TDIP-b and TTIP, b) SEM from the surface of FTO/TiO_2 deposited using TTIP, c) cross-sectional SEM of the sample in (b). 15
Figure 2-5 Cross-sectional SEM image of a full device using optimized bi-layer of TiO_2. 18
Figure 2-6 a) J-V curves for the best working perovskite solar cells made of TiO_2 using different TTIP solution concentrations and sequences, b) J-V curves measured in forward and reverse scans for the perovskite solar cell using 0.15 + 0.30 combination of TTIP. 19
Figure 2-7 J-V curves for the best working p-i-n perovskite solar cells with different NiO_X thicknesses. 21

Figure 2-8 J-V curves for the best working p-i-n perovskite solar cells with different C_{60} thicknesses. 23
Figure 2-9 a) The J-V curves for the best working perovskite solar cells with different active areas, b) the perovskite solar cell with three active areas held in my hand, c) The cross-sectional SEM image of the perovskite solar cell with 2.03 cm^2 of the active area. 25
Figure 3-1 a) XRD patterns for the PbI_2 layer deposited at 2.0-3.5 Å/s. SEM surface images of 250 nm PbI_2 layer deposited at a) 2.0 Å/s, b) 2.5 Å/s, c) 3.5 Å/s. The insets show the cross-sectional SEM images of the related sample. 32
Figure 3-2 AFM analysis for PbI_2 layer deposited at (a) 2 Å/s, (b) 2.5 Å/s, (c) 3.5 Å/s. d) RMS roughness values of the PbI_2 layer shown in a-c. 33
Figure 3-3 a) XRD pattern of the perovskite layers having the PbI_2 layer deposited at different rates. SEM surface and cross-sectional images of perovskites after conversion of PbI_2 layers at rates of (b,c) 2.0 Å/s, (d,e) 2.5 Å/s, (f,g) 3.5 Å/s. 35
Figure 3-4 Device structure used for perovskite solar cells and its corresponding cross-sectional SEM image. 36
Figure 3-5 a-d) Photovoltaic parameters of the perovskite solar cells made from PbI_2 layers deposited at different evaporation rates, e) J–V curves for the best devices made using PbI_2 deposited at different evaporation rates, f) Dark J–V curves for the best devices shown in e). 38
Figure 3-6 SEM surface and cross-sectional images for a, b) MAPI, c, d) MAPI-Cl, e, f) MAPI-Br, and g, h) MAPI-BrCl. 42
Figure 3-7 a) XRD patterns, b) Absorbance spectra, c) External quantum efficiency, and d) J–V curves for the perovskite solar cells with single, double and triple halides in the MA-halide solution. 43
Figure 3-8 XRD patterns for MAPI-BrCl with 5 and 10 mg of MACl. 45
Figure 3-9 a) Absorbance spectra of perovskite for different MABr:MAI molar ratio in the MA-halide solution, b) the absorbance edges of the samples in (a). 46

Figure 3-10 Photovoltaic parameters of the perovskite solar cells made with different MABr:MAI molar ratios between 0.36 to 0.71 in the MA solution. The amount of MACl was kept constant in all solutions.....47
Figure 3-11 The J–V characteristic curve and data for the champion cell with MABr/MAI molar ratio of 0.41.....48
Figure 3-12 Shockley-Queisser limit and average values for V_{OC} (a), J_{SC} (b), FF (c) and PCE (d). 49
Figure 3-13 Stability analysis for MAPI, MAPI-Cl, MAPI-Br, and MAPI-BrCl based on IV measurements taken under continuous one sun irradiance. 50
Figure 4-1 a) UPS measurements for fresh and 18 hours aged NiO_X/ITO, b) XPS for the samples in (a). 56
Figure 4-2 a) XRD patterns for as-deposited NiO_X/ITO and annealed NiO_X/ITO in the air at 300 °C. b) Perovskite solar cell configuration, c, d, e, f) all V_{OC}, J_{SC}, FF and PCE data for devices using as-deposited, annealed, coated with PTPD. 58
Figure 4-3 a) refractive indices of NiO_X/ITO deposited under APP = 4 mTorr, with different sputtering rates, b) Reflectance/transmittance measurement for the samples in (a), c) SCLC measurement for hole-only devices using NiO_X/ITO samples in (a), d) hole only device structure of the devices in (c), e) J-V of the best cells from samples in (a), f) cross-sectional SEM belonging to a cell in (e), g, h, I, j) all V_{OC}, J_{SC}, FF, and PCE data for devices using NiO_X/ITO samples in (a).....61
Figure 4-4 a) XRD patterns for NiO_X/ITO deposited under 4 and 16 mTorr of APP, b) refractive indices measured by spectroscopic ellipsometry for NiO_X/ITO samples deposited under APP of 2, 4, 6, and 16 mTorr, c) Reflectance/Transmittance for the samples in (b), d) Tauc plot for samples in (b), e) Absorbance spectrum for samples in (b), f) 1-R and the integrated Jph for full devices of (b) using 350 nm-thick perovskites, g) 1-R and the integrated Jph for full devices of (b) using 460 nm-thick perovskite. 65
Figure 4-5 a)SCLC measurement for the hole-only device using NiO_X/ITO prepared under different APPs, b) V_{TFL} values derived from (a), c) XPS regional

scan of the oxygen peak of the NiO_X/ITO samples in (a), d, e, f, g) all V_{OC}, J_{SC}, FF and PCE data for devices using NiO_X/ITO samples in (a). 68
Figure 4-6 a, b, c, d) all V_{OC}, J_{SC}, FF and PCE data for devices using CuO_X coated NiO_X/ITO samples with different CuO_X thicknesses, e) J-V for the best cells in (a), f) EQE spectra for the samples in (a). 71
Figure 4-7 a, b, c, d) all V_{OC}, J_{SC}, FF and PCE data for devices using SiO_2 coated NiO_X/ITO samples with different SiO_2 thicknesses, e) J-V for the best cells in (a), f) EQE spectra for the samples in (a). 72
Figure 4-8 a) XPS local peak for Cu depending on the different concentrations of Cu in NiO_X/ITO, b, c, d, e) all V_{OC}, J_{SC}, FF and PCE data for devices using Cu:NiO_X in (a). 74
Figure 4-9 a, b, c, d) all V_{OC}, J_{SC}, FF and PCE data for devices using different thicknesses of Cu:NiO_X/ITO samples. 76
Figure 4-10 a, b, c, d) all V_{OC}, J_{SC}, FF and PCE data for devices using NiO_X/ITO and Cu:NiO_X/ITO with 1.8% of Cu, e) Forward and reverse J-V for the best cells in (a). 77

LIST OF ABBREVIATIONS

ABBREVIATIONS	
AFM	Atomic Force Microscopy
APP	Argon Partial Pressure
a-Si	Amorphous Silicon
BCP	Bathocuproine
DSSC	Dye-Sensitized Solar Cells
EQE	External Quantum Efficiency
ETL	Electron Transport Layer
FTO	Flourine-doped Tin Oxide
FA	Formamidinium
FF	Fill Factor
FWHM	Full Width at Half Maximum
GIXRD	Grazing Incidence X-Ray Diffractometry
HTL	Hole Transport Layer
IEA	International Energy Agency
ITO	Tin-doped Indium Oxide
J-V	Current density-Voltage
J_{ph}	Photocurrent
J_{SC}	Short Circuit Current
LED	Light Emitting Diode
LiTFSI	Lithium bis(trifluoromethane sulfonyl)imide

MA	Methylammonium
MABr	Methylammonium Bromide
MACl	Methylammonium Chloride
MAI	Methylammonium Iodide
MAPI	Methylammonium Lead Iodide
PCE	Power Conversion Efficiency
PL	Photoluminescence
Poly-TPD	Poly(N,N'-bis-4-butylphenyl-N,N'-bisphenyl)benzidine
PPM	Parts Per Million
PV	Photovoltaics
QCM	Quartz Crystal Microbalance
RF	Radio-Frequency
RMS	Root Mean Square
SCLC	Space Charge Limited Current
SEM	Scanning Electron Microscopy
Spiro-OMeTAD	2,20,7,70-tetrakis-(N,N-dip-methoxyphenylamine)-9,9′-spirobifluorene
SQ	Shockley-Quiesser
TaTm	N4,N4,N4′,N4′-tetra([1,1′-biphenyl]-4-yl)-[1,1′:4′,1′-terphenyl]-4,4′-diamine
TBP	4-Tert-butyl pyridine
TCO	Transparent Conductive Oxide

TDIP-b	Titanium Diisopropoxide bis
TTIP	Titanium Tetraisopropoxide
UPS	Ultraviolet Photoelectron Spectroscopy
UV-VIS	Ultraviolet-Visible spectrum
V_{OC}	Open Circuit Voltage
V_{TFL}	Trap Filled Limit Voltage
XPS	X-Ray Photoelectron Spectroscopy
XRD	X-Ray Diffractometry

LIST OF SYMBOLS

SYMBOLS	
Å	Angstrom
Ag	Silver
Ar	Argon
Br	Bromine
CdTe	Cadmium Telluride
Cl	Chlorine
Co	Cobalt
Cu	Copper
CuO_X	Copper Oxide
e	Electronic charge
ε_0	Vacuum Permitivity
ε	Relative Dielectric Constant
I	Iodine
μ	Micro
λ	Lambda
MoO_X	Molybdenum Oxide
NiO	Nickel Oxide
n_{trap}	Trap Density
Ω	Ohm
Pb	Lead

$PbBr_2$	Lead Bromide
$PbCl_2$	Lead Chloride
PbI_2	Lead Iodide
Si	Silicon
SiO_2	Silicon Dioxide
Θ	Theta (degree)
TiO_2	Titanium Dioxide
$TiCl_4$	Titanium Tetrachloride

CHAPTER 1

INTRODUCTION

With the advent of the steam engine by Thomas Newcomen in 1712, the industrial revolution was inaugurated to promote the economy and lifestyle of human beings. However, over the last century, it lead to the accelerated demand for energy and in turn to the use of fossil fuels as a traditional energy source. The consumption of fossil fuels has increased the emission of greenhouse gases such as CO_2, leading to global warming and climate change. Therefore, alternative sources of energy such as photovoltaics (PV) are deemed necessary to depress the amount of CO_2 and to relieve the current status of the World atmosphere. In this thesis, our aim lies in the optimization of potentially scalable fabrication techniques of perovskite solar cells as a groundbreaking class of emerging PV.

1.1 Global warming and photovoltaics

The world's human population grew from 3 billion in 1960 to 7.8 billion in 2020 [1]. The growing standards of living and constant economic growth around the world has stimulated energy consumption from 10035 to 14050 million tonnes of oil equivalent over the period from 2000 to 2017 [2]. As another alarming fact, the emission rate of CO_2 has increased from 6 billion tonnes per year in 1989 to 32.5 billion tonnes per year in 2017 [2] such that in 2019 the amount of CO_2 exceeded 410 parts per million (ppm) in the atmosphere as shown in Figure 1-1.

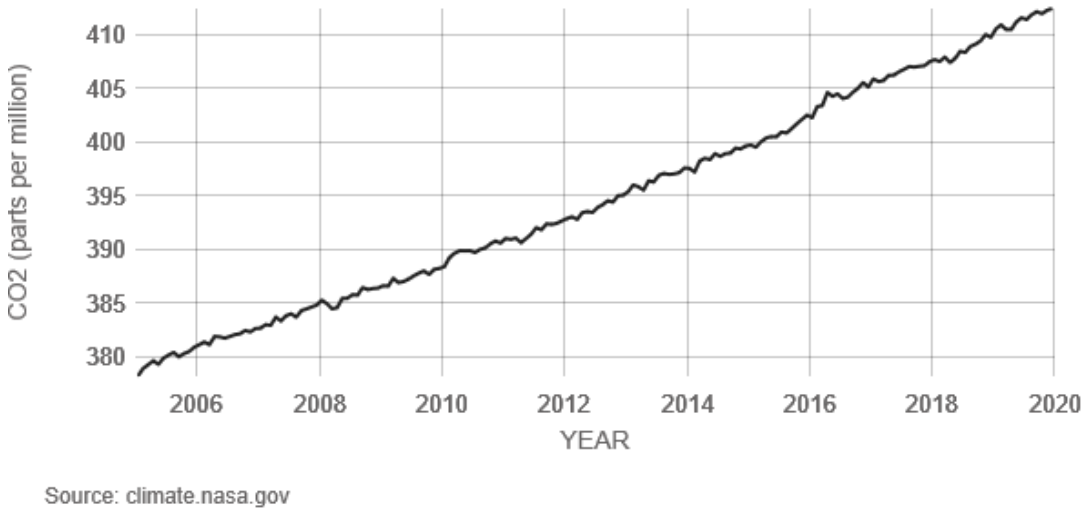

Figure 1-1.1 The yearly amount of CO_2 in units of parts per million in the atmosphere.

As one of the most malicious greenhouse gases, the escalated amount of CO_2 has lead to a global temperature rise of 1 °C from 1960 to 2020 [3]. To reduce the emission rate of CO_2, the energy demand and its clean generation must be balanced. That is why the need for renewable energy sources gets more and more highlighted. The share of renewable energy sources in the electricity supply of 2019 was 24.7% as shown in Figure 1-2. This number is forecast to be 40% in 2040, but it is not if it will be enough to halt global warming. According to International Energy Agency (IEA), among the renewable energy sources, photovoltaics (PV) is growing more popular due to its competitive optimization in sustainability [2].

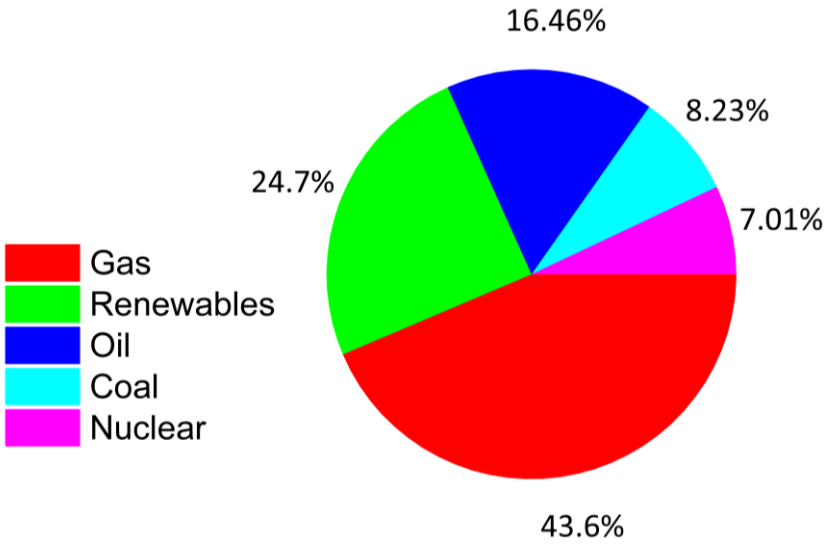

Figure 1-2. The share of the energy sources in global electricity consumption in 2019.

The photovoltaic effect was first discovered by Edmond Becquerel in 1839 and over the turn of the century in 1954, the first solar PV panel was launched based on Si. In the beginning, solar power was expensive limiting its usage to satellite applications. However, following the advances in fabrication procedures, the cost of energy supplied by the Si PV decreased from 76 US dollars per watt (US$/watt) in 1977 to 0.30 US$/watt in 2015 [4]. The first generation of solar cells was based on monocrystalline and polycrystalline Si making it a well-established industry that governs the PV market by 80%. In an attempt to reduce the material usage and cost, the second generation PV was proposed which is based on thin film technology such as amorphous Si and Cadmium Telluride (CdTe). To further utilize the Sun power via modern technologies, the third generation of PV has been under intense research. Multijunction solar cells, perovskite solar cells, organic solar cells, and quantum dot sensitized solar cells are some examples in this category. According to the efficiency chart of solar cells updated by the National Renewable Energy Laboratory (NREL) shown in Figure 1-3, the increase of efficiency has been the most rapid with perovskite solar cells among the emerging PV and other types of solar cells. The efficiency of this family of solar cells increased from 3.9% to 25.2% over only a

decade. This owes to the pioneering research and knowledge in other classes of PV especially dye-sensitized solar cells [5].

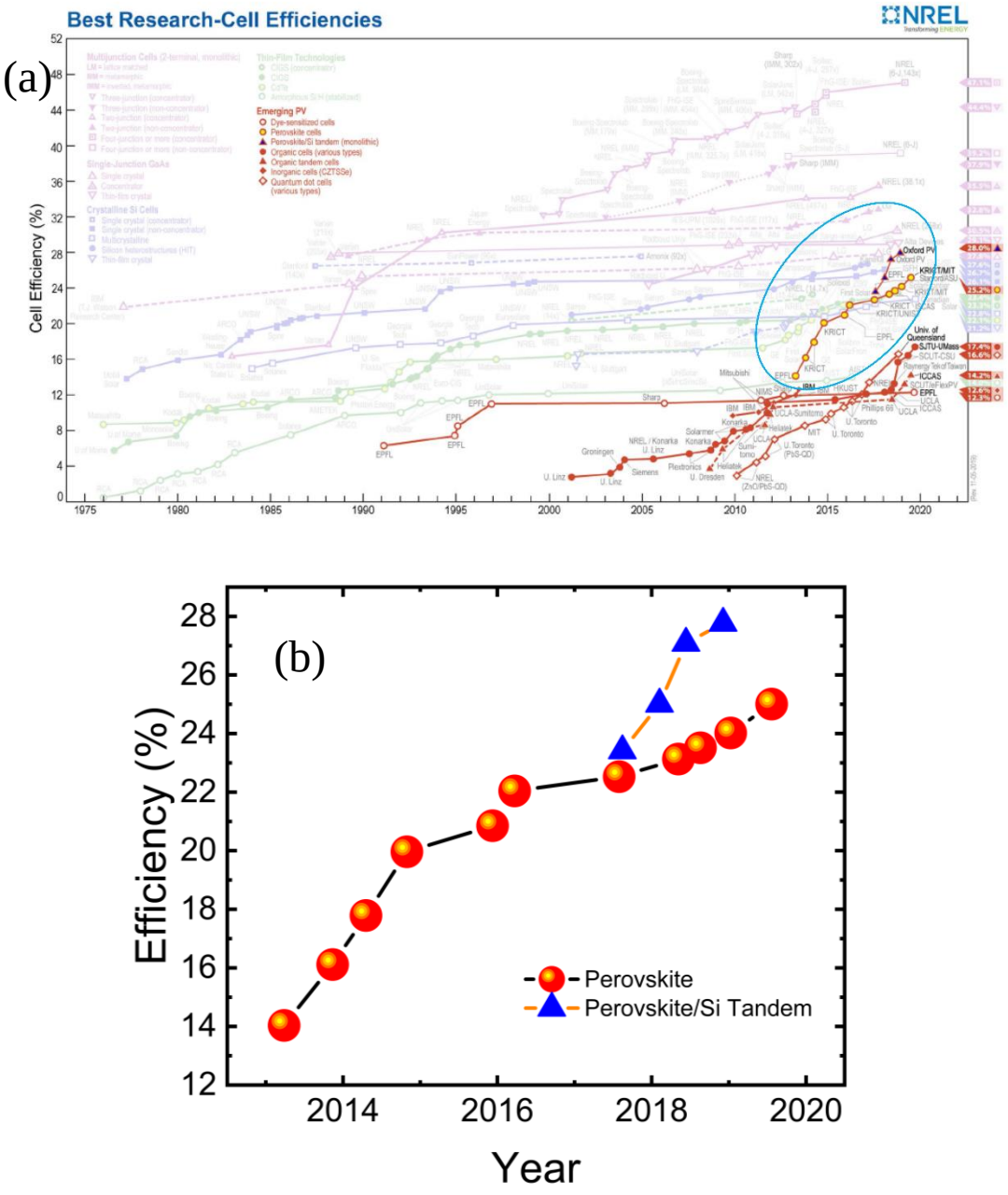

Figure 1-3 a) NREL efficiency chart for the emerging PV, b) NREL efficiency chart for perovskite and perovskite/Si tandem solar cells.

1.2 Perovskite solar cells

Perovskite was discovered in nature by Gustav Rose in the oxide form of $CaTiO_3$ in 1839 and was named after Russian mineralogist Lev Perovski. Organic inorganic metal halide perovskites usually have a chemical formula of ABX_3. A consists of organic methylammonium (MA), formamidinium (FA) or inorganic cations such as Rb or Cs. B is taken by Pb or Sn and the X site is typically occupied by I, Br or Cl halides as illustrated in Figure 1-4. The success in the application of perovskite absorbers in solar cells lies in their easy and cost-efficient fabrication processes. Perovskites possess excellent optoelectronic properties such as direct bandgap which can be tuned between 1.3 eV and 3.1 eV by changing the composition of A or X site [6]. The absorption coefficient of metal halide perovskites is in the range of 10^5 cm^{-1}[7]. Also, the exciton binding energy of $MAPbI_3$ (MAPI) has been reported to be as low as 37 meV which is comparable to the thermal energy of the cell under working condition [8]. Therefore, MAPI can plausibly be regarded as a semiconductor generating electrons and holes rather than excitons upon illumination. Besides, the charge carrier diffusion lengths exceed 1 μm [9].

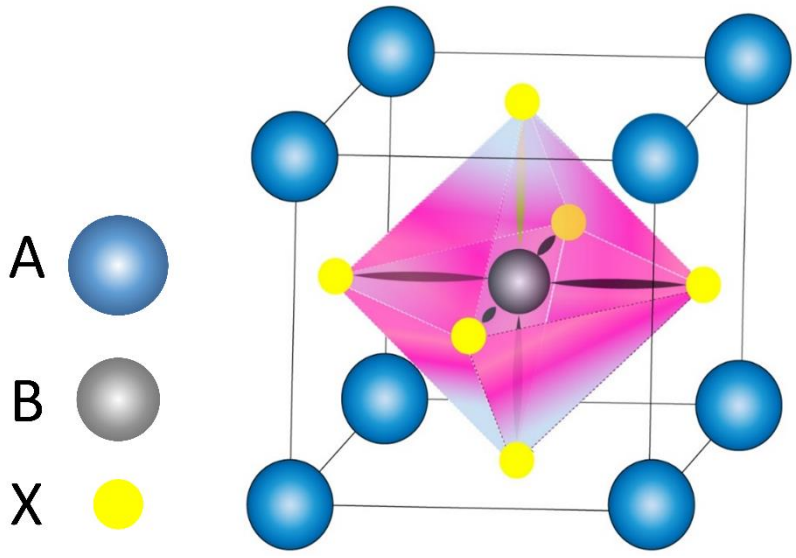

Figure 1-4 The structure of ABX_3 perovskite.

The first perovskite solar cell was born as a DSSC cell working with 3.9% efficiency [5]. Later, it was used by Park *et al* in a quantum dot sensitized cell exhibiting 6.5% efficiency. The first solid state perovskite solar cell was introduced by Snaith *et al* using a mesoporous structure with a solid phase hole transport layer demonstrating 10.9% efficiency in 2012 [10]. Later, metal halide perovskite was used as a thin film in a planar structure showing 12.2% efficiency due to its micron-scale charge carrier diffusion lengths [9]. Using planar structure for perovskite solar cells was a turning point in that, its application could be extended to larger area solar cells. Perovskite solar cells have been fabricated via a multitude of methods such as single step solution coating, two-step solution coating, two step vapor coating, vapor assisted solution coating, hybrid vapor-solution sequential coating, co-evaporation, chemical vapor deposition, pulsed laser deposition, doctor blade coating, slot-die coating, etc. Most of the record efficiencies reported for the perovskite solar cells have been achieved via the solution process. This is mainly due to the easier nondemanding routes in the solution process facilitating compositional control of the fabricated thin films. The two-step method was employed to get more reproducible results. Easy inexpensive processing along with efficiencies as high as 25.2% in single junction and 28% in perovskite/Si tandem devices already make perovskite solar cells a perfect candidate for the industrial application. The generated energy of perovskite solar cell modules is estimated to cost less than half of Si solar cells[1112]. However, two other crucial prerequisites to commercialize perovskite solar cells, are their scalability and stability. Co-evaporation has been successfully utilized to deposit uniform perovskite layers demonstrating efficiencies above 20.3% [13]. This methodology is discussed in the second chapter of the thesis. Since the deposition takes place in a high vacuum chamber (10^{-6} Torr), the role of the deposition pressure is used as a key parameter to obtain crystalline perovskite. The effect of post-annealing on the crystallinity of co-evaporated perovskite is intriguing and therefore was investigated in this thesis. The optoelectronic optimization of the perovskite solar cell depends not only on the perovskite layer but also on the transport layers used. Therefore, TiO_2 and C_{60} as electron transport layers need to be studied

systematically. Another potentially scalable deposition method to fabricate perovskite layers is a hybrid vapor-solution method in which the inorganic lead-halide compartment is first vacuum-deposited followed by solution coating of the organic compound[14]. The effect of the deposition rate of the lead-halide layer on the crystallinity and morphology of the perovskite film during the sequential method has not been studied yet. Also, the interdiffusion of the methylammonium-halide into the inorganic layer must be facilitated for the full reaction of the components. Therefore, we studied the effect of halide-mixing on the interdiffusion process and the outcoming photovoltaic properties of the perovskite layer. Another issue with the perovskite solar cells is their nonstable property which impedes their entry to the industry. The stability of perovskite solar cells has been improved to some extent during the recent years by stoichiometric modification, 2-dimensional (2D) perovskite layer onto the 3D layer, interface engineering, and encapsulation techniques. As a result, the lifetime of perovskite solar cells have reached 10000 hours [15]. We tried to improve the stability of the perovskite solar cells via halide-mixing during the vapor-solution technique. Apart from the absorber layer, the effect of the transport layers on the stability of the perovskite solar cells has been extremely important [16–18]. NiO_X, in particular, has been shown to improve the air-stability of perovskite solar cells [17]. The optimization of the NiO_X deposition technique is of prime importance for roll-to-roll productions. Therefore, we investigated the deposition parameters of NiO_X during a radio-frequency (RF) sputtering to optimize the optoelectronic properties of NiO_X as a hole transport layer in perovskite solar cells. In addition, the effect of doping the NiO_X layer with Cu during a co-sputtering process has not yet been studied in perovskite photovoltaics. Besides, since the passivation of NiO_X with organic and inorganic materials has shown better band-alignment of NiO_X with the perovskite layer, it is interesting to explore novel organic or inorganic materials to passivate NiO_X [19–21].

1.3 Thesis outline

The second chapter of the thesis addresses co-evaporation as a method to fabricate perovskite solar cells in two different configurations. TiO_2 and C_{60} as electron transport layers (ETL) were systematically optimized leading respectively to 13.0% and 16.1% efficiencies. Also, the co-evaporated perovskite was tested in the large active area perovskite solar cells with 6.0% and 5.5% efficiencies with 1.00 cm^2 and 2.03 cm^2 areas. In the third chapter of the thesis, we propose the employment of methylammonium bromide (MABr) and methylammonium chloride (MACl) as additives to facilitate the interdiffusion process and to control the crystallization of mixed halide perovskite during the hybrid vapor-solution sequential method. The resultant perovskite solar cells exhibited a maximum of 19.8% efficiency and stable performance under 1 Sun illumination. In the fourth chapter, the optimal radio frequency (RF) magnetron sputtering conditions for NiO_X as a hole transport layer (HTL) in perovskite solar cells are thoroughly discussed. The interface of perovskite/NiO_X was modified by organic and inorganic compounds promoting the reproducibility of the resultant perovskite solar cells. Sputtered Cu doped NiO_X was used for the first time in perovskite solar cells boosting the efficiency of the devices by 2.1% on average compared to the intrinsic NiO_X. Chapter five presents a summary of the concluding remarks as well as the future outlooks.

CHAPTER 2

LARGE AREA CO-EVAPORATED PEROVSKITE SOLAR CELLS WITH OPTIMIZED ELECTRON TRANSPORT LAYERS

Co-evaporation as a method to deposit planar film was first introduced by Snaith *et al*. in 2013 [22]. The perovskite was conformal and exhibited 15.4% efficiency. They optimized the deposition rates of $PbCl_2$ and MAI as the inorganic and organic sources to form $CH_3NH_3PbI_{3-X}Cl_X$ (MAPI-Cl). The record efficiencies for co-evaporated perovskite have been reported by Bolink *et al* where the deposition rates of PbI_2 (0.5 Å/s) and MAI (1 Å/s) were optimized to fabricate perovskite solar cells with 20.3% efficiency [13]. I was involved in a study with the same group to use double inorganic sources of PbI_2 and $PbCl_2$ to fabricate 16% efficient MAPI-Cl based solar cells[23]. Such nice results stem from a pure phase perovskite without residual solvents deposited uniformly. Therefore, co-evaporation is a nice candidate to construct perovskite solar cells in large areas. In section 2.1, an optimization of the co-evaporation method is carried out to fabricate a highly crystalline perovskite layer. In sections 2.1.2-3, the fabrication and systematic optimization of solution-processed TiO_2 as electron transport layer is presented which resulted in 11.5% efficiency of perovskite solar cells in the n-i-p structure. Later, the transport layers in p-i-n structure (NiO_X and C_{60}) are optimized demonstrating perovskite solar cells with 16.3% efficiency as presented in sections 2.1.4-6. The p-i-n structure was used to fabricate large area perovskite solar cells showing 5.5% and 6.0% efficiencies with 2.03 cm^2 and 1.00 cm^2 of the active area as shown in section 2.1.6.

2.1 Co-evaporated perovskite solar cells

To fabricate perovskite films, $PbCl_2$ and MAI were used as the inorganic and organic sources, respectively. While $PbCl_2$ was purchased from Sigma-Aldrich, MAI was synthesized by reacting 60 mL of methylamine (40% in methanol) and 80 mL of hydroiodic acid (57 wt% in water) in a 250 mL round-bottom flask containing 150 mL absolute ethanol at 0 °C. Before adding the HI and CH_3NH_2, the ethanol-containing flask was kept stirring at 0 °C for 30 minutes under an Argon environment. Then, CH_3NH_2 was added to the flask followed by the dropwise addition of HI. The solution was kept stirring for 2 hours at 0 °C. The precipitate was recovered by putting the solution on a rotary evaporator at 50 °C. The yellowish raw product of CH_3NH_3I was washed with diethyl ether once. Later, the powder was dissolved in ethanol and was recrystallized 3 times. MAI was collected and dried at 60 °C in a vacuum oven for 24 hours. To fabricate perovskite films, the substrates were transferred to a chamber which was evacuated to 5×10^{-6} Torr of base pressure. The deposition rate of $PbCl_2$ was monitored by a gold-coated quartz crystal microbalance (QCM). Since slow deposition rates let the vapor molecules have enough time to migrate over the surface of the substrate and find the best place in terms of the lowest energy, the deposition rate of $PbCl_2$ was kept at 0.3 Å/s throughout the co-evaporations. The evaporation of MAI however, is not easy to control due to its omnidirectional evaporation as illustrated in Figure 2.1a. The evaporated MAI molecules randomly scatter and occupy the volume of the vacuum chamber. Figure 2.1b shows the evaporation rate of MAI and the pressure change inside the chamber during the deposition. According to this figure, the deposition rate of MAI follows the MAI partial pressure. Other research groups have also used MAI partial pressure to control the deposition rate of MAI [24,25].

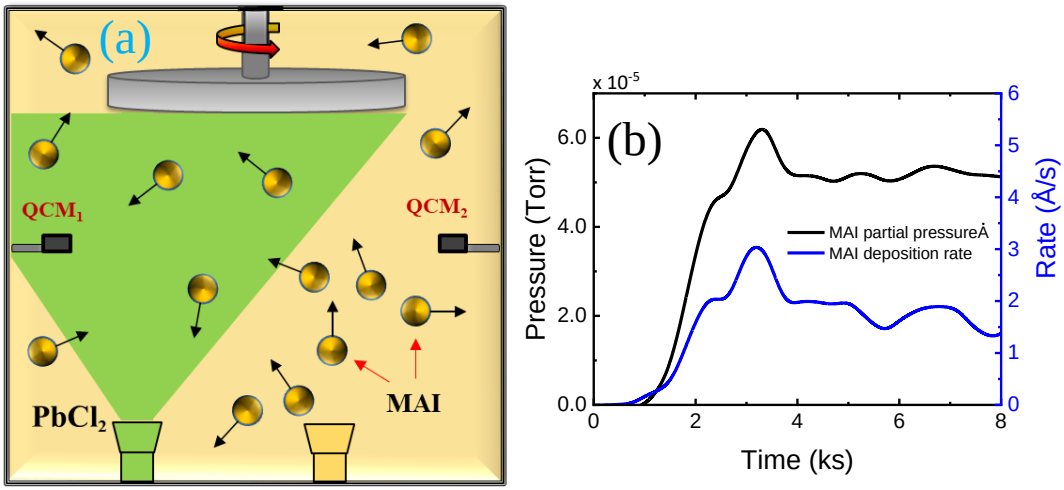

Figure 2-1 a) The vacuum chamber for co-evaporation of $PbCl_2$ (green cone) and MAI (yellow circles) which scatter around the chamber, b) MAI vapor pressure and deposition rate.

We used glass substrates to study the crystallinity and optical properties of perovskite. Keeping the deposition rate of $PbCl_2$ constant at 0.3 Å/s, the MAI partial pressure was varied among 4×10^{-5}, 5×10^{-5}, and 6×10^{-5} Torr. Figure 2-2 depicts the XRD patterns for the resultant glass/MAPI-Cl films. The diffractions at 2θ of 14.3°, 28.5°, 31.3°, and 40.5° respectively correspond to the (110), (220), (310), and (224) crystal planes of perovskite [26]. According to the XRD results, the MAPI-Cl made under 4×10^{-5} Torr of MAI partial pressure exhibited strong diffraction at 2θ = 12.6° belonging to (100) crystal plane of PbI_2 [26]. Therefore, the film is a mixture of perovskite and PbI_2 phases. Among all, the MAPI-Cl fabricated under 5×10^{-5} Torr of MAI partial pressure demonstrated the most intense (110) diffraction peak indicating its superior crystallinity over the other samples. Apart from the deposition parameters, there have been numerous reports regarding improved crystallinity of perovskite by post-treatments such as annealing. Therefore, we annealed the perovskite film in the air for different periods tracking the full width at half maximum (FWHM) of (110) peak at 2θ = 14.3°. FWHM of a specific peak in the XRD pattern is inversely proportional to the crystallite size. According to Scherer's formula (Equation 2.1), the smaller the FWHM, the larger the grains.

$$D = (0.94 \times \lambda) / (\beta \times \cos(\theta)) \quad (2.1)$$

Where, D is the crystallite size in nm, λ denoted the employed X-ray $k\alpha_1$ beam wavelength (0.1542 nm), and β is FWHM. The results have been summarized in Table 2-1. 30 minutes of annealing the perovskite film resulted in the narrowest FWHM indicating larger crystallites. The scanning electron microscope (SEM) image of the perovskite surface shows perovskite grains larger than 500 nm as shown in Figure 2-3a. The UV-Visible (UV-Vis) spectroscopy of the fabricated perovskite exhibits a sharp absorption at λ = 780 and photoluminescence (PL) peak at λ = 760 nm as shown in Figure 2-3b. In short, the XRD, UV-Vis spectroscopy, SEM and PL analyses indicate a pure crystalline phase of perovskite film with a sharp absorption at its bandgap (E_g). Therefore, the solar cells presented in the next sections of this chapter are constructed using the optimized perovskite film here.

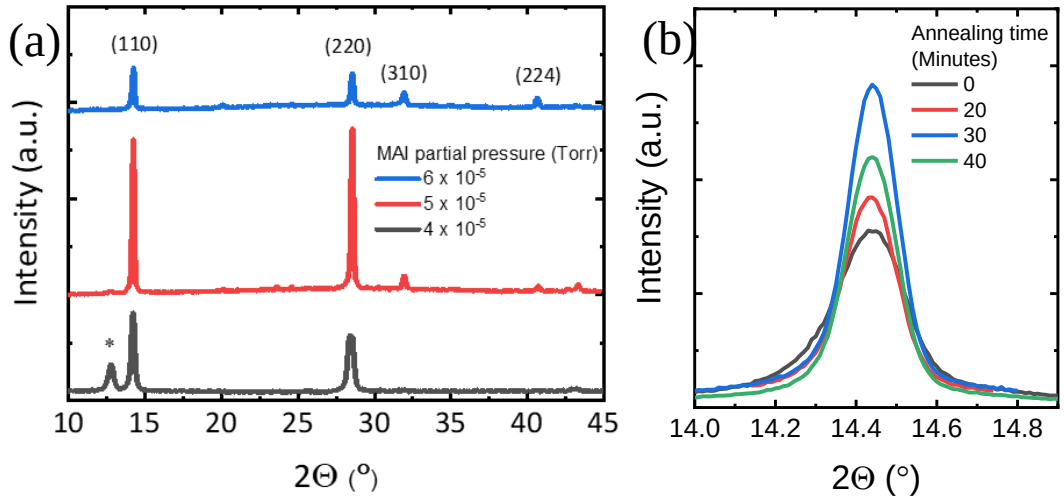

Figure 2-2 a) X-ray diffractograms of co-evaporated perovskite films under different MAI partial pressures, b) the (110) plane diffraction of the MAPI-Cl annealed in the air for different periods.

Table 2-1 The FWHM of the (110) crystal plane of MAPI-Cl shown in Figure 2-2b.

Annealing time (minutes)	**0**	**20**	**30**	**40**
(110) FWHM (°)	**0.22**	**0.16**	**0.14**	**0.15**

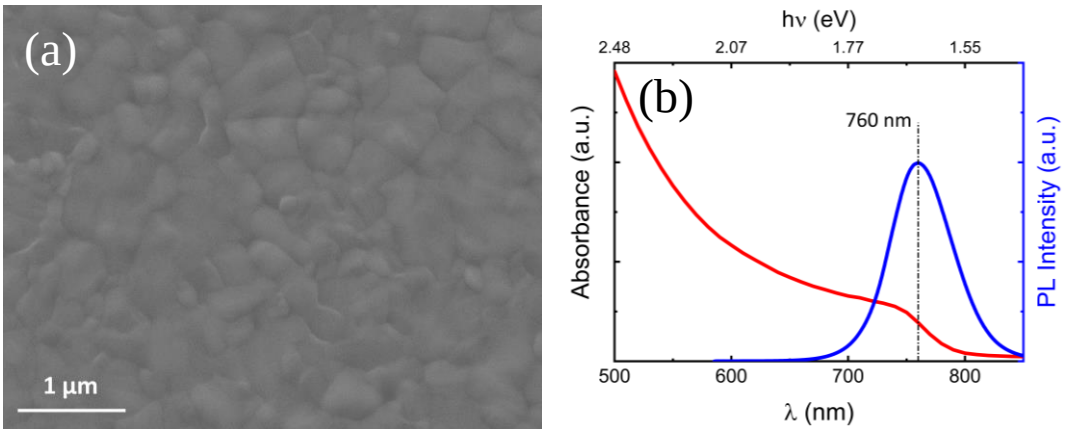

Figure 2-3 a) SEM image of the MAPI-Cl sample deposited under 5×10^{-5} Torr of MAI partial pressure and annealed for 30 minutes in the air, b) the absorbance (red) and photoluminescence spectra (blue) of the sample in (a).

2.1.1 n-i-p structure perovskite solar cells using the optimized deposition parameters

Depending on the light incident side of perovskite solar cells, they are categorized into n-i-p or p-i-n structures. In the n-i-p configuration, the light incident side of the substrate is transparent conductive oxide (TCO)/electron transport layer (ETL). While in p-i-n configuration, the substrate is TCO/hole transport layer (HTL). TiO_2 has been one of the most popular ETLs in the n-i-p perovskite solar cells due to its wide bandgap and matched conduction band with MAPI. TiO_2 can be fabricated using various techniques such as spin coating, radiofrequency magnetron sputtering, electrodeposition, spray pyrolysis, atomic later deposition (ALD), etc. In the current study, we focused on the optimization of TiO_2 film deposited via spin coating. For this purpose, we investigated the crystallinity of TiO_2 deposited using titanium diisopropoxide bis (TDIP-b) and titanium tetraisopropoxide (TTIP). As the substrate, fluorine-doped tin oxide (FTO) coated glass was purchased from Pilkington (NSG TEC^{TM} 7 with RS = 7 Ω sq^{-1}) and was washed using 10-minute sonication in acetone, 2 vol.% hellmanex in H_2O and isopropanol, consecutively. Later, the substrates were

treated by UV-ozone plasma for 15 minutes to remove any organic contamination and to increase the hydrophilicity of the surface. A 0.3 M solution of TDIP-b or TTIP with 13 mM HCl in 1-butanol, was spun at 1500rpm for 6 seconds followed by 3000 rpm for 30 seconds. Then it was heated at 150 °C for 10 minutes before annealing at 500 °C for 30 minutes. Grazing incidence XRD (GIXRD) analysis (shown in Figure 2-4a) at a grazing incidence of 0.3° shows TiO_2 diffractions at 25.3°, 36.1°, 48.1°, and 54.0° attributed to (101), (004), (200) and (105) planes which are indicative of crystalline TiO_2 in anatase phase [27]. The (101) peak is more intense in TTIP as compared with TDIP-b. Besides, the full width at half maximum (FWHM) of (101) peak is 0.90° for TDIP-b and 0.56° for TTIP. In view of these results and Scherrer's formula (Equation 2.1), the TiO_2 made using TTIP has higher crystallinity which ensures fewer grain boundaries within TiO_2 and thereby more efficient charge transport.

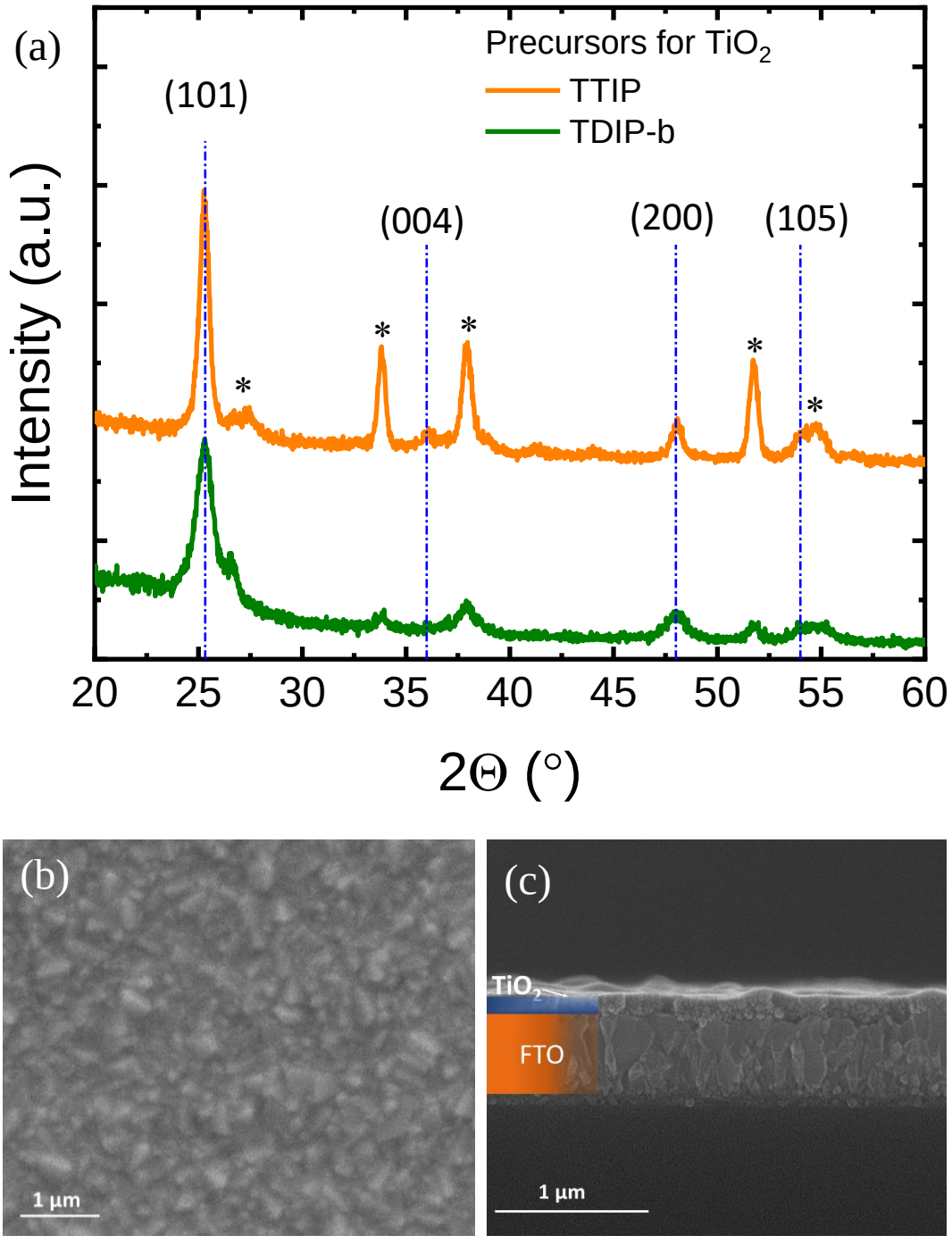

Figure 2-4 a) GIXRD patterns measured at 0.3° incidence for FTO/TiO_2 deposited using TDIP-b and TTIP, b) SEM from the surface of FTO/TiO_2 deposited using TTIP, c) cross-sectional SEM of the sample in (b).

2.1.2 $TiCl_4$ treatment of TiO_2

The interface between perovskite and TiO_2 layer is of critical importance to fulfill the charge extraction efficiency of TiO_2. $TiCl_4$ treatment has been shown to fill in the cracks on the surface of TiO_2 and to depress its work function resulting in lower charge recombination at the perovskite/TiO_2 interface [28]. For this purpose, TiO_2/FTO substrates are typically immersed in a hot deionized (DI) water bath containing 0.05 M $TiCl_4$ and later annealed at 500 °C for 30 minutes before using as the substrate in perovskite solar cells. In the literature, the treatment is performed for 30 minutes at 70 °C [29]. In this section, 20, 30, 45 and 60 minutes of TiCl4 treatment were compared in full perovskite solar cells shown in Figure. Therefore, the $TiCl_4$ treated TiO_2/FTO substrates were coated by co-evaporated MAPI-Cl (discussed in section 3.1). As HTL, 2,20,7,70-tetrakis-(N,N-dip-methoxyphenylamine)-9,9′-spirobifluorene (Spiro-OMeTAD, 73.2 mg mL^{-1} of anhydrous chlorobenzene) was spin-coated at 2000 rpm for 20 seconds onto the substrates to form 200 nm thick layer. Spiro-OMeTAD was doped with 4-tert-butyl pyridine (TBP, 11.4 μL), lithium bis(trifluoromethane sulfonyl)imide (LiTFSI, 12 μL) solution (520 mg mL^{-1} of acetonitrile) and 7.2 μL of FK 209 Co(III) TFSI (stock solution 375 mg mL^{-1} of acetonitrile) [30]. Finally, a 100 nm thick Ag was vacuum-deposited (base pressure of 5 x 10^{-6} Torr) to form the top electrode. According to the J-V characteristics of the full devices (Table 2-2), 45 minutes of $TiCl_4$ treatment resulted in the best average fill factor (FF), open circuit voltage (V_{OC}) and power conversion efficiency (PCE).

Table 2-2 The resultant average and best J-V characteristics following different times of $TiCl_4$ treatment.

$TiCl_4$ treatment time (minutes)		20	30	45	60
V_{OC} (mV)	Ave.	1009.0	1001.0	1064.7	1040.7
	Best	1027.7	1040.5	1088.1	1052.2
J_{SC} (mA/cm^2)	Ave.	9.3	10.4	11.3	12.1
	Best	14.2	12.9	14.1	14.5
FF (%)	Ave.	63.0	61.2	71.1	63.9
	Best	61.3	61.1	67.7	59.2
PCE (%)	Ave.	5.9	6.4	8.6	8.1
	Best	9.0	8.2	10.4	9.0

2.1.3 Bilayer of TiO_2

Since the surface of FTO is rough with root mean square roughness (R_{rms}) of 16-50 nm [31], a single solution coating of TiO_2 might result in uncoated areas of FTO leading in charge recombination sites at MAPI-Cl/TiO_2 interface. Therefore, the TTIP solution was spin coated twice to form the final TiO_2 layer. For this purpose, three molarities of TTIP solution were considered: 0.1, 0.15 and 0.3 M with five different sequence-combinations of the first and second TTIP solutions. The substrates were later annealed at 500 °C for 30 minutes, treated by $TiCl_4$ for 45 minutes, annealed at 500 °C for another 30 minutes and finally were used to make full MAPI-Cl solar cells explained in section 3.2. A cross-sectional SEM of a finished device is given in Figure 2-5. The J-V curves for the best working devices in each TTIP sequence

category and average J-V characteristic values have been demonstrated in Figure 2-6a and Table 2-3. According to these results, the initiation of spin coating of TTIP with 0.15 M followed by 0.3 M solution coating resulted in the highest average J_{SC} (16.4 mA/cm^2, best: 17.8 mA/cm^2) and therefore highest average PCE (10.2%, best: 11.5%) compared to other combinations. Although the TiO_2 layer was optimized, the resultant devices showed hysteresis as shown in Figure 2-6b. A solar cell is hysteretic if it shows different J-V characteristics depending on the sweeping direction of voltage during the measurement.

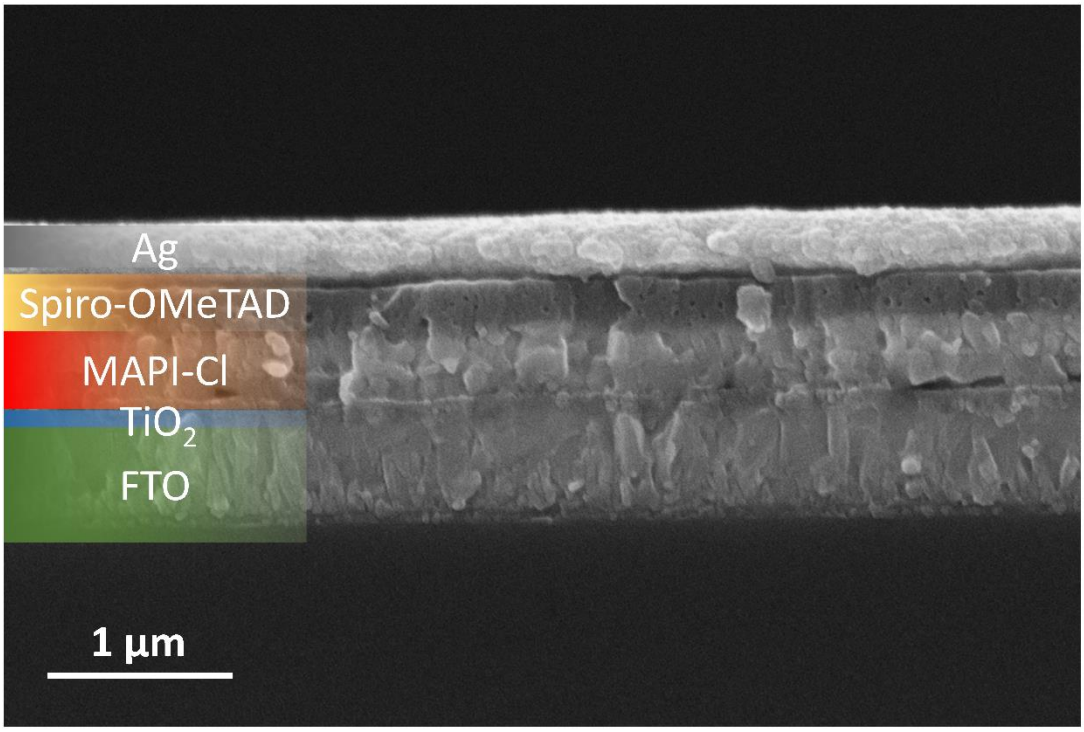

Figure 2-5 Cross-sectional SEM image of a full device using optimized bi-layer of TiO_2.

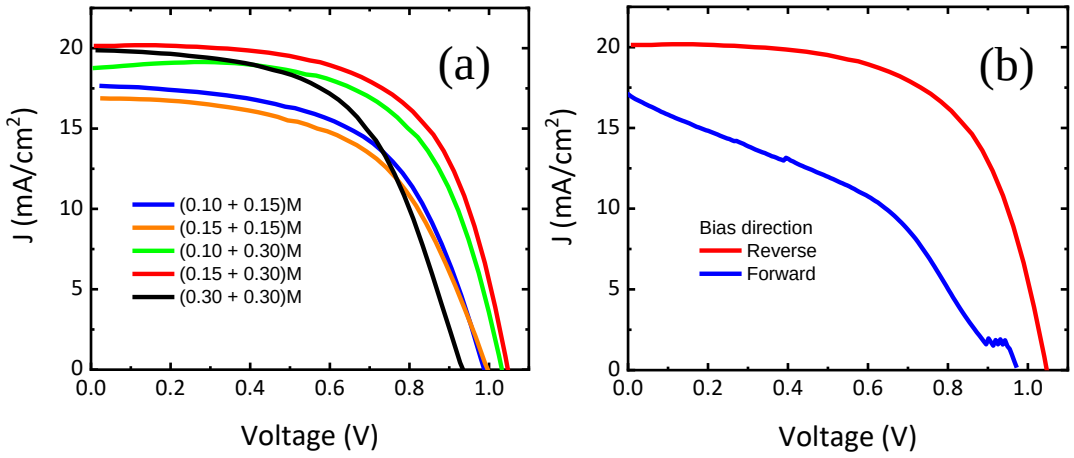

Figure 2-6 a) J-V curves for the best working perovskite solar cells made of TiO_2 using different TTIP solution concentrations and sequences, b) J-V curves measured in forward and reverse scans for the perovskite solar cell using 0.15 + 0.30 combination of TTIP.

Table 2-3 Summarized average and best-cell J-V characteristic data for the perovskite solar cells made of TiO_2 using different TTIP solution concentrations and sequences.

TTIP solution order (M)		**V_{OC} (mV)**	**J_{SC} (mA/cm²)**	**FF (%)**	**PCE (%)**
(0.10+0.15)	Ave.	1002.7	16.1	56.0	9.0
	(Best)	(988.3)	(17.6)	(57.3)	(10.0)
(0.15+0.15)	Ave.	984.7	16.5	52.2	8.5
	(Best)	(998.2)	(16.8)	(57.3)	(9.5)
(0.10+0.30)	Ave.	1017.1	15.8	63.5	10.2
	(Best)	(1031.7)	(18.7)	(62.4)	(12.0)
(0.15+0.30)	Ave.	990.4	18.6	63.0	11.6
	(Best)	(1046.3)	(20.1)	(61.9)	(13.0)
(0.30+0.30)	Ave.	949.9	18.0	56.5	9.7
	(Best)	(936.5)	(19.9)	(56.6)	(10.5)

2.1.4 p-i-n perovskite solar cells

The p-i-n configuration of perovskite solar cells has been popular due to non-hysteretic behavior as compared to the n-i-p structure. Moreover, since there is typically no need for high-temperature fabrication steps in contrast to compact TiO_2 (500 °C as discussed in section 2.1.3), the p-i-n configuration is a good candidate with unresistant-to-heat TCO/glass or flexible substrates making it an industrially attractive choice. The structure used in this thesis has been shown in Figure. In this structure, all the layers are deposited using vacuum deposition. As a result, it will be shown viable in the large active area (2.03 cm^2) solar cells in this subsection. As substrates, NiO_X/tin-doped indium oxide (ITO) was used. NiO_X layer was deposited using radiofrequency (RF) magnetron sputtering to form a uniform layer. The optoelectronic properties and the optimization of sputtered NiO_X have been thoroughly studied in Chapter 4. Here, a range of previously reported optimized parameters has been employed to sputter NiO_X [32]. Therefore, an argon partial pressure of 20 mTorr with a deposition rate of 1 nm/min was used to deposit NiO_X. As ETL a layer of fullerene (C_{60}) is evaporated at a rate of 0.5 Å/s (base pressure of 5×10^{-6} torr) atop ITO/NiO_X/MAPI-Cl followed by 7 nm thick Bathocuproine (BCP) vacuum deposition (at a rate 0.5 Å/s and base pressure of 8×10^{-6} torr) as a hole blocking layer [33,34]. The thicknesses of NiO_X and C_{60} are optimized before usage in large area perovskite solar cells. Starting with NiO_X, a 20 nm thick C60 was used throughout the experiments [35]. The thicknesses of sputtered NiO_X were chosen as 40, 65 and 90 nm. The resultant effects were probed in the performance of full perovskite solar cells as exhibited by J-V characteristic data in Figure 2-7 and Table 2-4.

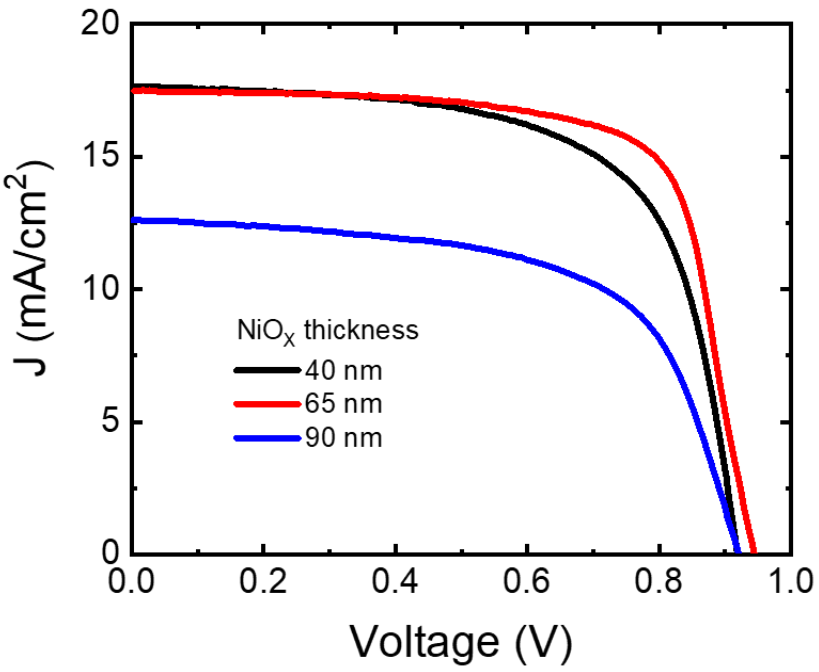

Figure 2-7 J-V curves for the best working p-i-n perovskite solar cells with different NiO_X thicknesses.

Table 2-4 Average and best (in parenthesis) J-V characteristic data for p-i-n perovskite solar cells with different NiO_X thicknesses.

NiO_X thickness (nm)	**Voc (mV)**	**Jsc (mA/cm^2)**	**FF (%)**	**PCE (%)**
40	931.6 ± 9 (919.5)	17.0 ± 0.7 (17.7)	60.4 ± 3.4 (65.5)	9.5 ± 0.7 (10.7)
65	949.8 ± 12.6 (945.1)	16.9 ± 0.8 (17.5)	68.3 ± 4.6 (72.2)	10.9 ± 0.8 (11.9)
90	922.2 ± 11.2 (921.6)	12.2 ± 0.3 (12.6)	59.6 ± 1.6 (61.8)	6.6 ± 0.3 (7.2)

According to the J-V characteristic data for the perovskite solar cells, 65 nm thick NiO_X resulted in the highest average V_{OC} (949.8 mV) and FF (68.3%). The average J_{SC} in the case of 40 nm thick NiO_X, was the highest, but it exhibited low V_{OC} (931.6 mV) and FF (60.4%). In sum, the highest average (10.9%) and best (11.9%) PCE was achieved when NiO_X was 65 nm thick. To further optimize the p-i-n solar cells, the thickness of C_{60} as the ETL was also triggered. We tested the effect of 10 to 50 nm of C_{60} thickness on the performance of the full devices. The J-V plots for the best working devices in each category are shown in Figure 2-8. Also, Table 2-5 summarizes the average and best J-V characteristic data for the solar cells. When C_{60} was 10 nm, the resultant devices showed the lowest average V_{OC} (982.1 mV). On the other hand, 50 nm thick C_{60} resulted in the lowest average FF (46.8%) indicating increased resistance of C_{60} at this thickness. The best overall J-V characteristics and highest average efficiencies (12.2% and 12.5%) were achieved when C_{60} was 20 nm and 30 nm thick. Especially, the champion solar cell worked with 16.1% efficiency. In conclusion, the thickness of C_{60} must be in the range of 20 to 30 nm to achieve the highest efficiencies in perovskite solar cells employing C_{60} as the ETL. This is also in agreement with previous studies [23,36].

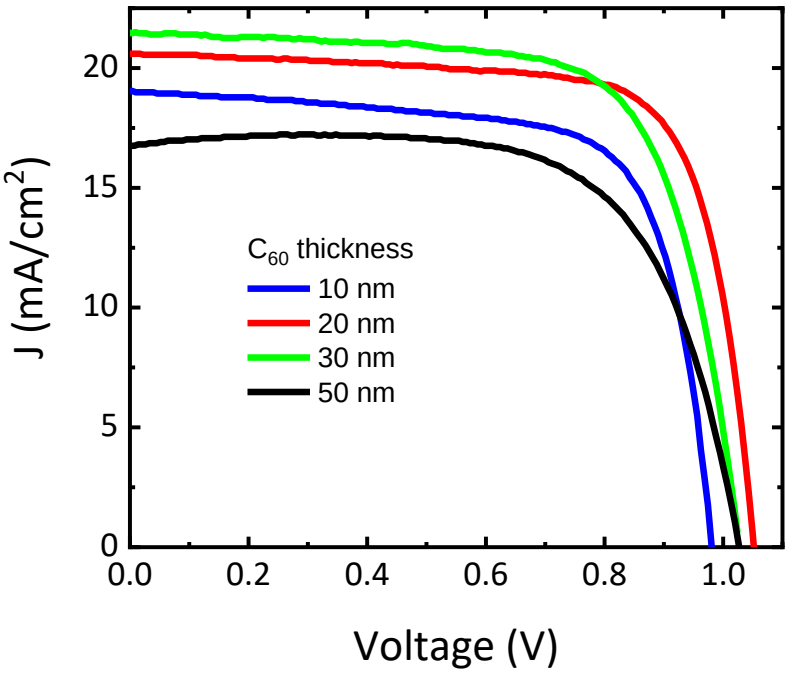

Figure 2-8 J-V curves for the best working p-i-n perovskite solar cells with different C_{60} thicknesses.

Table 2-5 The average and best (in parenthesis) data for J-V characteristic data for perovskite solar cells with different C_{60} thicknesses.

C_{60} thickness (nm)	**V_{OC} (mV)**	**J_{SC} (mA/cm^2)**	**FF (%)**	**PCE (%)**
10	982.1 (980.1)	16.3 (19.0)	61.0 (71.0)	9.8 (13.2)
20	1002.0 (1051.4)	17.9 (20.5)	68.1 (74.6)	12.2 (16.1)
30	1000.2 (1027.9)	18.8 (21.3)	66.7 (70.6)	12.5 (15.5)
50	1001.9 (1026.5)	16.0 (16.6)	46.8 (68.8)	7.5 (11.7)

2.1.5 Large area perovskite solar cells

Since the p-i-n configuration of the perovskite solar cells used in this chapter were fabricated using vacuum depositions, we chose this structure for the large area cells. Also, this configuration demonstrated higher efficiencies (16.1%) as compared to the n-i-p structure (PCE = 13.0%) with the co-evaporated perovskite solar cells made in our lab. Therefore, the large active area (1.00 cm^2 and 2.03 cm^2) perovskite solar cells were fabricated using the optimized parameters for the p-i-n structure such as 65 nm thick sputtered NiO_X and 25 nm thick C_{60}. Also, more conductive ITO substrates (Rs = 7 Ω aq^{-1}) were employed to reduce the probable series resistance arising from ITO with Rs = 15 Ω aq^{-1}. The J-V curves and data are shown in Figure 2-9a and Table 2-6. Smaller area cells (0.05 cm^2) were also fabricated on the same substrates for comparison. The substrate containing different active areas of perovskite cells is shown in Figure 2-9b. The cross-sectional SEM image of the device is given in Figure 2-9c showing a 560 nm thick perovskite layer in the device. The devices showed close efficiencies in forward and reverse sweeping direction indicating minimal hysteresis. As the active area increased from 0.05 cm^2 to 2.03 cm^2, the average FF dropped from 60.1% to 47.4%. Also, there was a drop in the average V_{OC} and J_{SC} by 46.6 mV and 2.5 mA/cm^2, respectively. The drops in the FF and J_{SC} are attributed to the increased series resistance of the solar cell due to the large area of bottom ITO (Rs = 7 Ω aq^{-1}). Despite the drop in the overall efficiency, large area perovskite solar cells were successfully fabricated demonstrating efficiencies of 6.0% and 5.5% with 1.0 cm^2 and 2.03 cm^2 of the active areas.

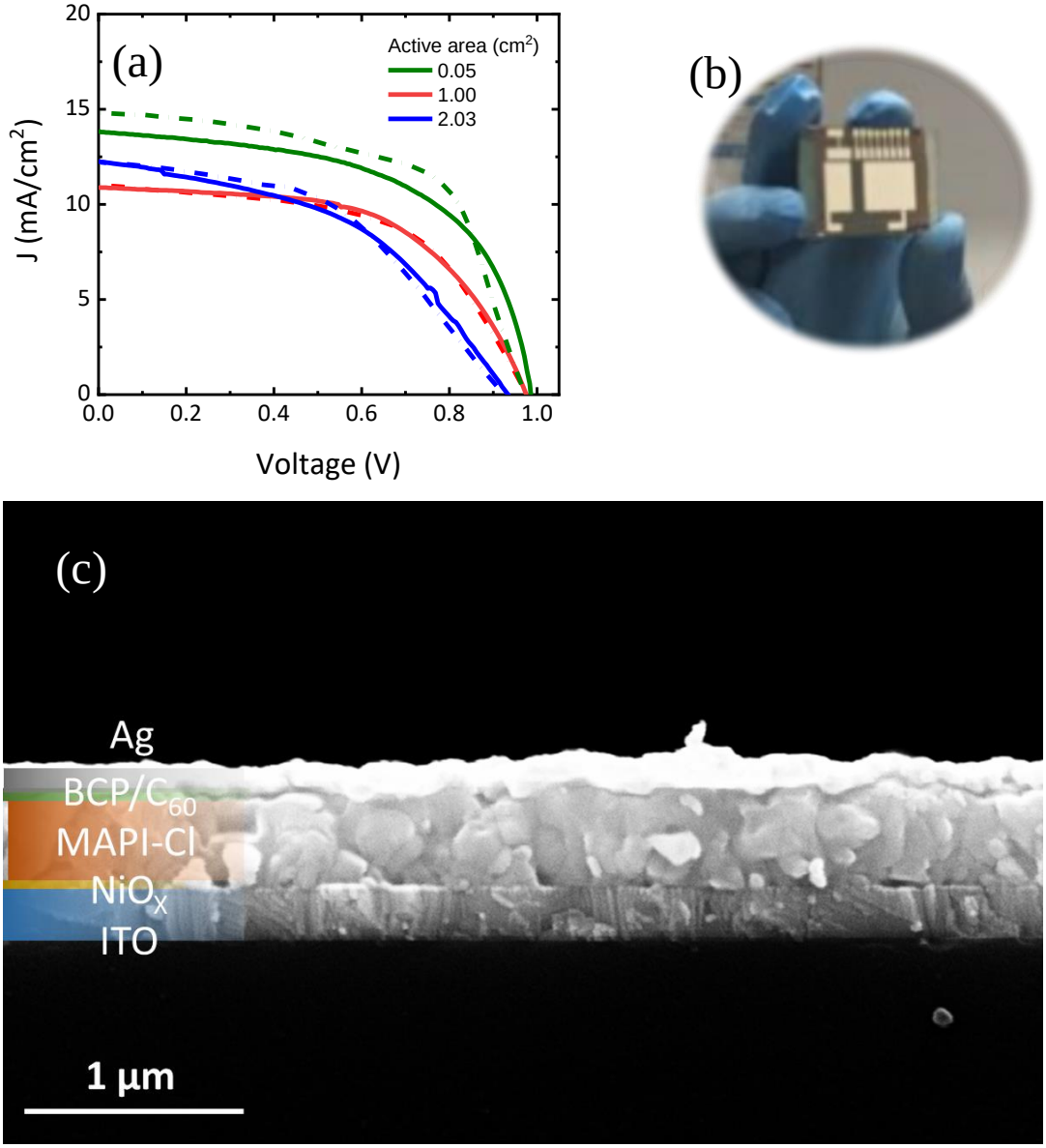

Figure 2-9 a) The J-V curves for the best working perovskite solar cells with different active areas, b) the perovskite solar cell with three active areas, c) The cross-sectional SEM image of the perovskite solar cell with an active area 2.03 cm^2.

Table 2-6 The performance details for the best working perovskite solar cells with different active areas corresponding to Figure 2-9a.

Active area (cm^2)	**Scan direction**	**V_{OC} (mV)**	**J_{SC} (mA/cm^2)**	**FF (%)**	**PCE (%)**
0.05	Forward	984.6	13.9	56.5	7.7
	Reverse	975.4	14.7	60.1	8.7
1.00	Forward	975.6	10.8	57.0	6.0
	Reverse	977.0	11.1	55.5	6.0
2.03	Forward	932.7	12.5	46.9	5.5
	Reverse	928.8	12.2	47.4	5.4

We argue that the second issue causing the efficiency drop with large active area perovskite solar cells is the reproducibility of the perovskite layer co-evaporated using a chamber with the substrate mounting unit opening to the air. The organic source used for the co-evaporation (MAI) is extremely hygroscopic and condensates onto the inner walls of the vacuum chamber during every deposition of the perovskite layer. Therefore, every deposition follows a different amount of MAI on the walls with different volume of adsorbed humidity. This made us suffer from the performance reproducibility of the perovskite solar cells. As a result, the chamber should be isolated from the air using an N_2 or Ar filled glovebox to make the co-evaporation more reproducible.

CHAPTER 3

HYBRID VAPOR-SOLUTION SEQUENTIALLY DEPOSITED MIXED-HALIDE PEROVSKITE SOLAR CELLS

The recent sky-rocketing performance of perovskite solar cells has triggered a strong interest in further upgrading the fabrication techniques to meet the scalability requirements of the photovoltaic industry. The integration of vapor-deposition into the solution process in a sequential fashion can boost the uniformity and reproducibility of the perovskite solar cells. Besides, mixed-halide perovskites have exhibited outstanding crystallinity as well as higher stability compared with iodide-only perovskite. Here the deposition rate of the PbI_2 layer was systematically optimized along with Br^- and Cl^- content at the solution deposition step of the sequential method towards rendering high and reproducible performance of the perovskite solar cells. Then the solution step was further inspected addressing MABr/MAI molar ratio and found to be 0.41 to minimize the deviation from the Shockley-Queisser limit at the corresponding bandgap. The introduction of MABr and MACl into the hybrid vapor-solution method showed a successful control over the crystallization and morphology of the perovskite layer which resulted in high efficiencies up to 19.8% in p-i-n devices exhibiting 90 hours operational stability under continuous illumination. The fabrication of triple halide perovskites using a hybrid vapor-solution method was shown to serve as an excellent choice towards scalable production techniques.

3.1 Hybrid vapor-solution sequential deposition

Lorem The unprecedented evolution of halide perovskites optoelectronics, achieving photovoltaic efficiencies beyond 25.2% [37] in less than 11 years, stems from their high absorption coefficients, long charge carrier diffusion lengths and adjustable

bandgaps [9,11,38-40]. In contrast with conventional methylammonium lead iodide ($CH_3NH_3PbI_3$ or MAPI), partial replacement of methylammonium (MA) with formamidinium (FA) and Cesium (Cs), has exhibited enhanced thermal, moisture and mechanical stability of the perovskite layer [41-44]. Also, including fractional bromide (Br^-) instead of iodide (I^-), has proven to boost the crystal formation, efficiency as well as the phase stability of perovskite [43,45]. A myriad of fabrication techniques for making potentially low cost yet high-quality perovskites have been developed which mainly include solution-based and/or evaporation techniques. The solution process has been popular due to the ease of stoichiometric control and low-cost nature. Thus, most of the reported record efficiencies have been achieved using wet chemical processes. In this category, in a single step perovskite fabrication method, where all the precursors are in the same solution, the crystallization of the perovskite film has been controlled using antisolvent technique and other post-treatments like heat or vacuum quenching [46]. However, typically the sequential deposition method, where each deposition step involves the use of a solution with some of the precursors, has been shown to result in more uniform pin-hole free perovskite layers [47,48]. Despite the simplicity of the solution process, it often lacks reproducibility and applicability to large-area solar cells [49]. On the other hand, techniques such as co-evaporation, render high uniformity and thickness control of the perovskite layer with nominal efficiencies above 20% [13,50]. All evaporated sequential method also proved as a promising method in achieving highly crystalline perovskite films with 17.6% efficiency [51]. In principle, evaporation-based methods are appealing since industrial-scale devices can be realized due to their high reproducibility and uniformity. However, it is not straightforward to construct multi-halide or multi-cation perovskites with stoichiometric precision. As a result, combining evaporation and solution in a sequential fashion called hybrid vapor-solution technique is expected to benefit from the advantages of both vapor deposition and solution process such as uniformity, time investment and simplicity altogether [52]. During the hybrid vapor-solution method, first, a layer of lead halide (PbX_2 with X = I, Cl) is vacuum deposited and then the organic component is

introduced by immersion into or by spin-coating an alcohol solution containing MA^- or FA^- halide[1448525354]. Vapor deposition of the inorganic PbX_2 ensures a uniform layer throughout the surface of the substrate. In addition, since the formation of the perovskite is accompanied by volume expansion of the initial PbX_2 layer, the final structure is a continuous pinhole-free perovskite film. This makes the method particularly interesting for roll-to-roll production procedures such as slot-die and spray coating[5556]. Recently, Rafizadeh *et al* used a hybrid vapor-solution method to fabricate planar MAPI-based devices with 18.9% efficiency in n-i-p structure[57]. Inasmuch as they used TiO_2 as the substrate, the evaporated PbI_2 layer was porous promoting its transformation into perovskite during the solution step. However, using TiO_2 in direct contact with perovskite typically results in hysteresis[58-60]. Applying organic inter/sublayers has widely been shown to mitigate the hysteresis [50,61-63]. Nevertheless, this was also shown to induce a nonporous compact PbI_2 layer [14]. Therefore, employing diffusive ions such as Br^- or Cl^- in the solution step, are deemed necessary to facilitate the conversion of the PbI_2 layer into perovskite. Besides, compared with MAPI, mixed halide perovskites have proven to possess larger charge carrier mobilities and longer diffusion lengths which can suppress the hysteresis [9]. Moreover, it was shown by Sun *et al* that the addition of Br^- and Cl^- enhances the crystallinity and photoluminescence quantum yield (PLQY) of the perovskite film [64].

Hence, we analyze the main crystallization and perovskite formation processes in each step of the sequential hybrid vapor-solution fabrication method. In the first step, we studied the effect of the deposition rate of the PbI_2 bottom layer on its roughness, which determines the subsequent crystallization of perovskite and device performance. During the second step, the inclusion of Br^-, Cl^- and their combination in the MA-halide solution, was thoroughly investigated which resulted in improved overall device performance up to 19.8% with V_{OC} above 1144.8 mV and FF more than 82% with no hysteresis. Such performance enhancement was shown to stem from the improved crystallinity of mixed halide perovskites and reduced nonradiative recombination within the structure of the perovskite solar cell [65]. While

Cl^- was effective to transform the initial PbI_2 layer into perovskite, the addition of Br^- was found to be essential for sustaining the operational stability.

3.2 Results and Discussion

3.2.1 PbI_2 layer

The initial PbI_2 layer can be deposited either by solution or evaporation during the two-step sequential method. Evaporation enables effective control over the thickness, crystallinity, and morphology of a highly pure PbI_2 layer without residual solvents. The quality of the final perovskite layer depends predominantly on the properties of the initial PbI_2 film [48]. After introducing the organic MA-halide solution, the reaction initially takes place at PbI_2 crystal defects and follows the Ostwald's step rule to reduce Gibbs free energy engendering perovskite [66]. The reaction between PbI_2 and MA-halide components starts by forming a capping layer of perovskite on top followed by a dissolution-recrystallization process and a series of PbI_2 grain migration within the film to form perovskite [67]. The crystallization of the capping layer at the surface is rapid and can impede the effective interdiffusion of the organic precursors into the integral bulk of the PbI_2 layer. To expedite the mass transfer of the organic compounds during the sequential method, many routes have been proposed such as adding ammonium acid iodide (AAI) derivatives to PbI_2 precursor [68], treating PbI_2 with chlorobenzene [69], introducing cyclohexane to MA-iodide solution to lower the solution polarity [70], and incorporating Cl^- during a multi-cycle dropping technique [71]. Fu *et al* showed that using poly-crystalline substrates such as TiO_2, ZnO, CdS, Zn(O,S) and FTO induces porous plate-like PbI_2 microstructures, while, amorphous substrates such as CuSCN, PEDOT:PSS and PCBM result in compact PbI_2 layers [14]. Conversion of compact PbI_2 into perovskite is challenging due to its dense structure. During the sequential approach, the inclusion of small halide ions such as Cl^- and Br^- has been shown to improve the mass transfer of MA compounds into the PbI_2 layer [64,72]. Therefore, we propose using

MACl and MABr to facilitate the diffusion of the organic solutes through the packed PbI_2 grains to effectively convert them into the perovskite layer. Here we focus on the effect of the PbI_2 sublimation rate, choosing 2.0, 2.5 and 3.5 Å/s, on the resulting PbI_2 layer and thereby on the perovskite film and the associated device performance. In particular, crystallinity and morphology were studied by X-Ray Diffractometry (XRD), Atomic Force Microscopy (AFM) and Scanning Electron Microscopy (SEM). As shown in Figure 3-1a, the vacuum deposited PbI_2 film (thickness = 250 nm) demonstrates 3 diffraction peaks at 2θ =12.7°, 25.5° and 38.6° belonging to the (100), (011), and (110) PbI_2 crystal planes, respectively. The PbI_2 layers deposited at different rates share common XRD patterns. The dominant (100) planar orientation is indicative of the preferential growth of PbI_2 grains perpendicular to the c-axis [73]. This is further shown by SEM images in Figure 3-1b-d, where the PbI_2 layer is in the form of smooth platelets packed along the horizontal plane irrespective of the deposition rate. However, according to AFM measurements in Figure 3-2a-d, the surface roughness of PbI_2 film increases slightly from Root Mean Square (RMS) values of 2.7 to 4.0 nm as the deposition rate is changed from 2.0 to 3.5 Å/s, respectively.

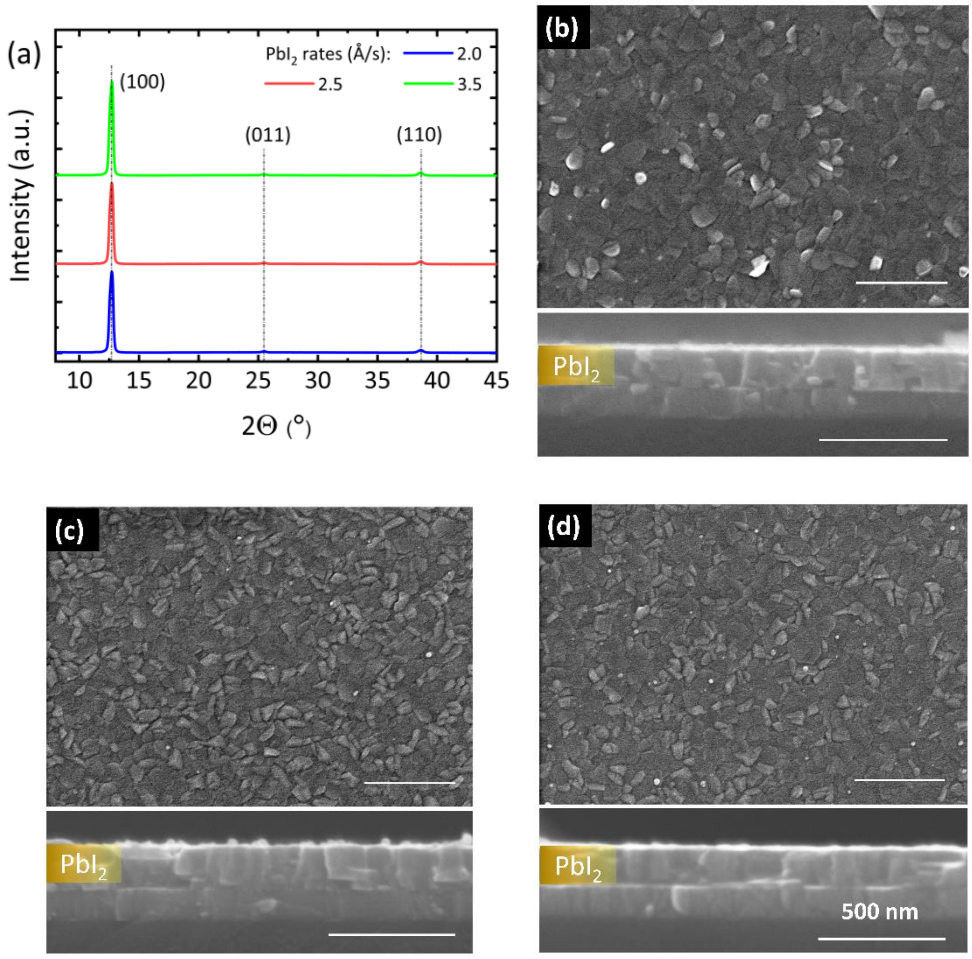

Figure 3-1 a) XRD patterns for the PbI_2 layer deposited at deposition rates of 2.0-3.5 Å/s. SEM surface images of 250 nm PbI_2 layer deposited at a) 2.0 Å/s, b) 2.5 Å/s, c) 3.5 Å/s. The insets show the cross-sectional SEM images of the related sample.

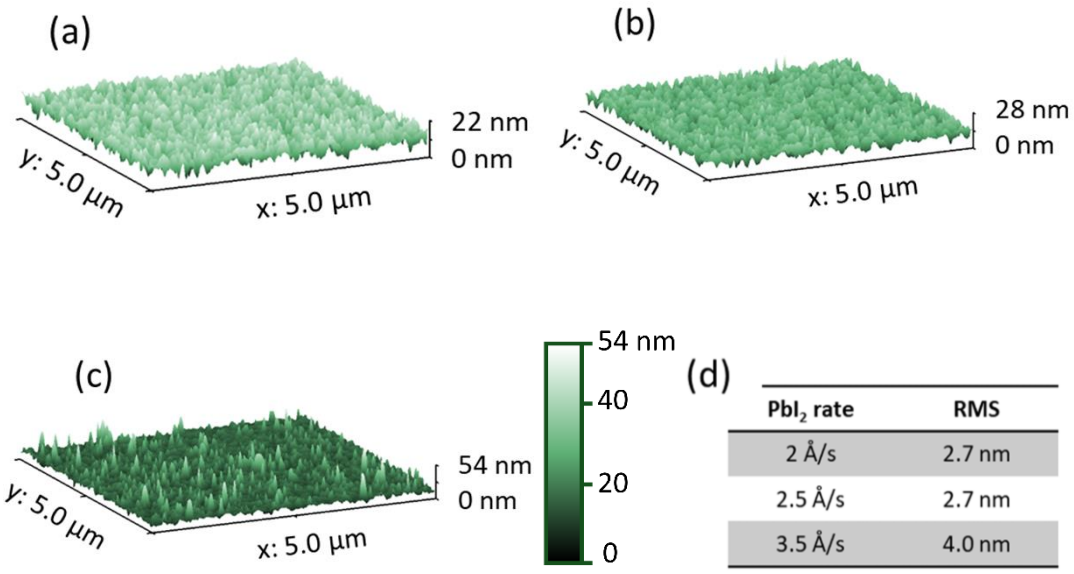

PbI_2 rate	RMS
2 Å/s	2.7 nm
2.5 Å/s	2.7 nm
3.5 Å/s	4.0 nm

Figure 3-2 AFM results for PbI_2 layer deposited at (a) 2 Å/s, (b) 2.5 Å/s, (c) 3.5 Å/s. d) RMS roughness values of the PbI_2 layer shown in a-c.

The perovskite layer was subsequently formed by spin-casting MA-halide solution containing MAI (35 mg), MABr (10 mg) and MACl (5 mg) in 1 ml of IPA. According to Figure 3-3a, when PbI_2 is deposited at 2.0 Å/s, there exists a PbI_2 diffraction peak at $2\theta=12.7^\circ$ in the diffractogram of the perovskite implying that the final perovskite layer is PbI_2 rich. However, the same peak is suppressed when the initial PbI_2 is sublimed at 2.5 Å/s, and it is eliminated when the deposition rate of PbI_2 is further increased to 3.5 Å/s, as shown in Figure 3-3a. This is attributed to the increased roughness of PbI_2 deposited at high rates (Figure 3-2d) and thereby more defects to initiate the reaction between MA-halide and PbI_2 platelets. In addition, as the deposition rate increases, the resultant film is likely to be more porous allowing for better impregnation of the MA-halides into the PbI_2 film. The surface and cross-sectional view of the perovskite layers depending on the initial deposition rate of PbI_2 are shown in SEM images in Figure 3-3b-g. The thickness of the final perovskite layer is 350 nm in all the samples. They present directional grains or boundaries which can hinder the charge carrier collection in the vertical orientation, a benchmark of MACl incorporation during perovskite fabrication [74]. However, the

surface morphology changes depending on the deposition rate of the initial PbI_2 layer. When the PbI_2 rate is 2.0 Å/s, bright platelets remain at the surface of the final perovskite (Figure 3-3b, c) which is speculated to be due to residual unreacted PbI_2, since heavy-atom regions appear with brighter contrast in the SEM images [65]. This is in line with the XRD analysis in Figure 3-3a, which shows a more intense PbI_2 peak when the deposition rate is 2.0 Å/s. The white flakes are in the form of scattered platelets throughout the surface. The perovskite layers formed out of PbI_2 deposited at higher rates of 2.5 and 3.5 Å/s are compact with micro-scale grains as demonstrated in Figure 3-3d-g. Bright regions are also detectable with higher rates of 2.5 and 3.5 Å/s shown with circles on the SEM images. Nevertheless, the number of PbI_2 platelets reduces with the deposition rate. Collectively, these results indicate more intercalation of PbI_2 with organic components as the deposition rate of PbI_2 increases.

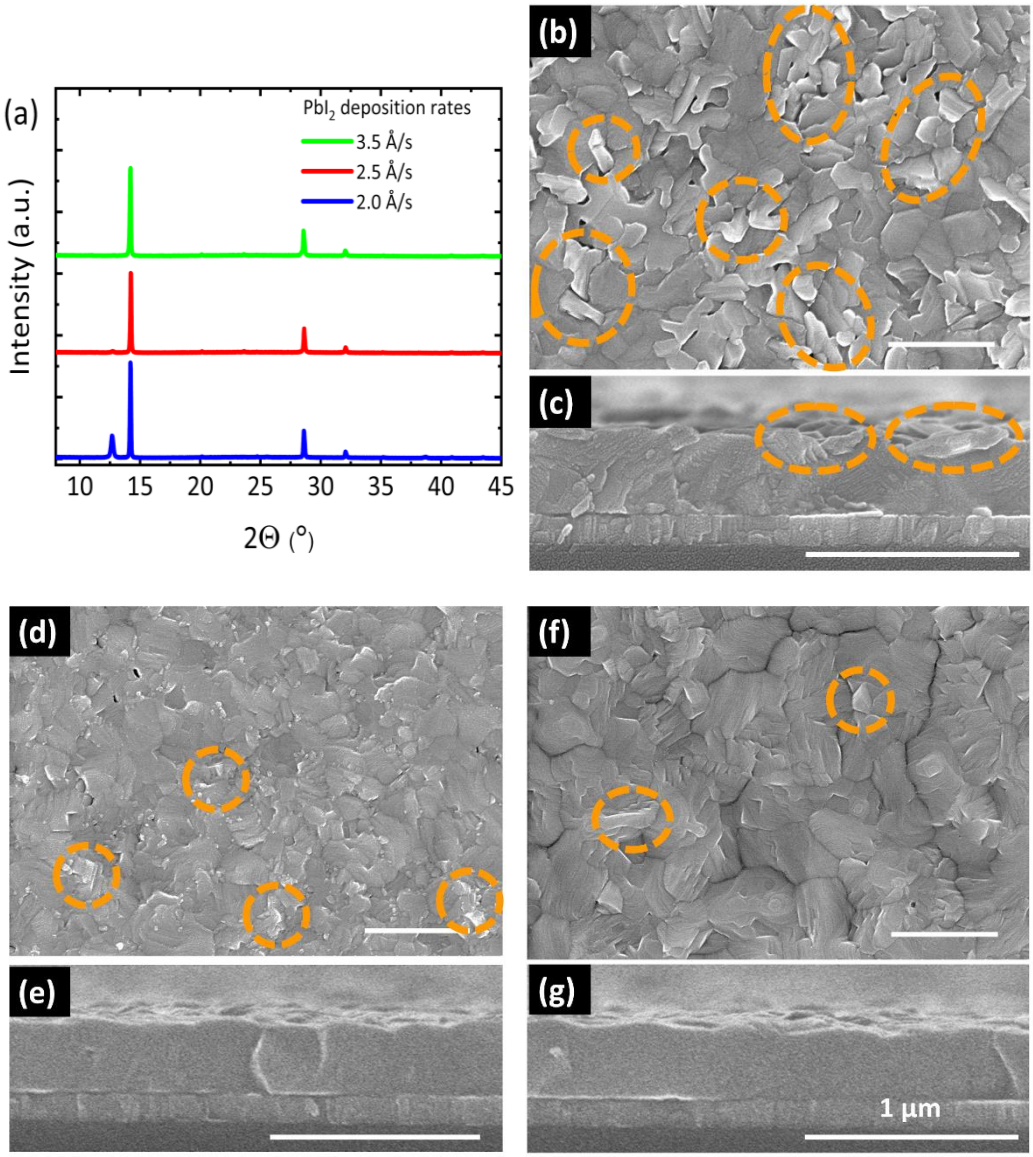

Figure 3-3 a) XRD pattern of the perovskite layers having the PbI_2 layer deposited at different rates. SEM surface and cross-sectional images of perovskites after conversion of PbI_2 layers at rates of (b,c) 2.0 Å/s, (d,e) 2.5 Å/s, (f,g) 3.5 Å/s.

The effect of the PbI_2 sublimation rate on the performance of the devices was studied in perovskite solar cells fabricated in the p-i-n configuration shown in Figure 3-4. In this structure, perovskite is sandwiched between N4,N4,N4′,N4′-tetra([1,1′-biphenyl]-4-yl)-[1,1′:4′,1′-terphenyl]-4,4′-diamine (TaTm)/ molybdenum oxide (MoO_X) as hole transport layer (HTL) and C_{60}/ bathocuproine (BCP) as electron

transport layer (ETL). All the transport layers were vacuum deposited as detailed in the Experimental Section.

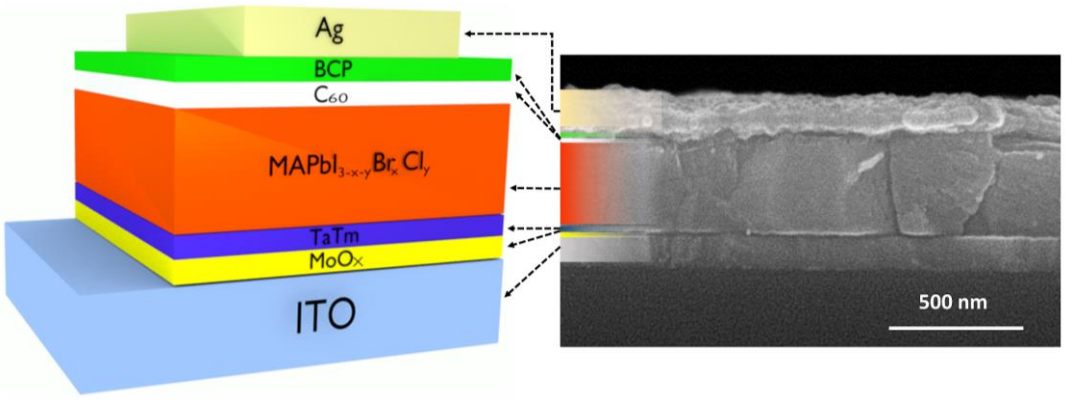

Figure 3-4 Device structure used for perovskite solar cells and its corresponding cross-sectional SEM image.

3.2.2 Device fabrication

The ITO-coated substrates were sonicated for 10 minutes successively in soap, deionized water, and isopropanol, followed by UV-ozone treatment for 15 minutes. Then, the samples were transferred into a vacuum chamber integrated into an N_2-glovebox. A 6 nm-thick MoO_X was thermally evaporated at a base pressure of 2×10^{-7} Torr onto the substrates followed by an annealing step at 100 °C for 10 minutes. Later, 10-nm thick TaTm was thermally deposited under a vacuum of 5×10^{-6} Torr, followed by 250 nm-thick PbI_2 at rates of 2.0, 2.5 and 3.5 Å/s for the rate study and 2.5 Å/s for the rest of the paper. The deposition rate was monitored using quartz crystal microbalance (QCM). Later, the MA-halide solution was spin-cast at 2100 rpm for 30 seconds on top of ITO/MoO_X/TaTm/PbI_2-coated substrates, which was followed by an annealing step at 100 °C for 45 minutes to form the perovskite layer. The substrates were washed twice by IPA and dried on a hot plate at 100 °C. Unless otherwise stated, the MA-halide solution consisted of MAI (35mg), MABr (10 mg) and MACl (5 mg) per 1 ml of anhydrous IPA. The perovskite coated

substrates were transferred into a vacuum chamber to deposit C_{60} and BCP (25 and 7 nm, respectively) as electron transport layers at a base pressure of 5×10^{-6} Torr. Finally, a 100 nm-thick Ag was deposited by thermal evaporation at a pressure of 2×10^{-7} Torr to form the electrode.

The current density–voltage (J–V) curves and their statistics are summarized in Figure 3-5 and Table 3-1. The highest average and record open circuit voltages (V_{OC} = 1102.7 mV and 1117.0 mV, respectively) were achieved for the lowest deposition rate of 2.0 Å/s. This is correlated with the excess unreacted PbI_2 at the interfaces of perovskite, which has been shown to passivate nonradiative recombination centers [75]. On one hand, as the deposition rate of PbI_2 increased from 2.0 to 3.5 Å/s, the average V_{OC} dropped monotonically from 1102.7 to 1020.8 mV as shown in Figure 3-5a. On the other hand, the average short circuit current (J_{SC}) increased from 20.3 to 21.7 mA/cm^2 as the deposition rate of PbI_2 increased from 2.0 to 2.5 Å/s, and dropped 0.2 mA/cm^2 when the deposition rate was 3.5 Å/s as given in Figure 3-5b. The increase in J_{SC} is likely because of better conversion of PbI_2 into perovskite as implied by the XRD analysis in Figure 3-3a. Above all, the highest average fill factor (FF = 77.4%) was measured when the deposition rate was 2.5 Å/s for PbI_2. As a result, the highest average efficiency of 18.1% and lowest parameter scattering were achieved when the sublimation rate of PbI_2 was 2.5 Å/s implying higher reproducibility. When the deposition rate was 3.5 Å/s, there seemed to be a higher current leakage according to the dark J–V curves presented in Figure 3-5f. This is rationalized by the formation of PbI_2 deficient perovskite as seen in Figure 3-3f-g. Excess PbI_2 as in the case of lower PbI_2 rates, can passivate the perovskite film and facilitate charge transportation [65]. As a result, considering the highest efficiencies and reproducibility, the deposition rate of PbI_2 was kept constant at 2.5 Å/s in the following sections.

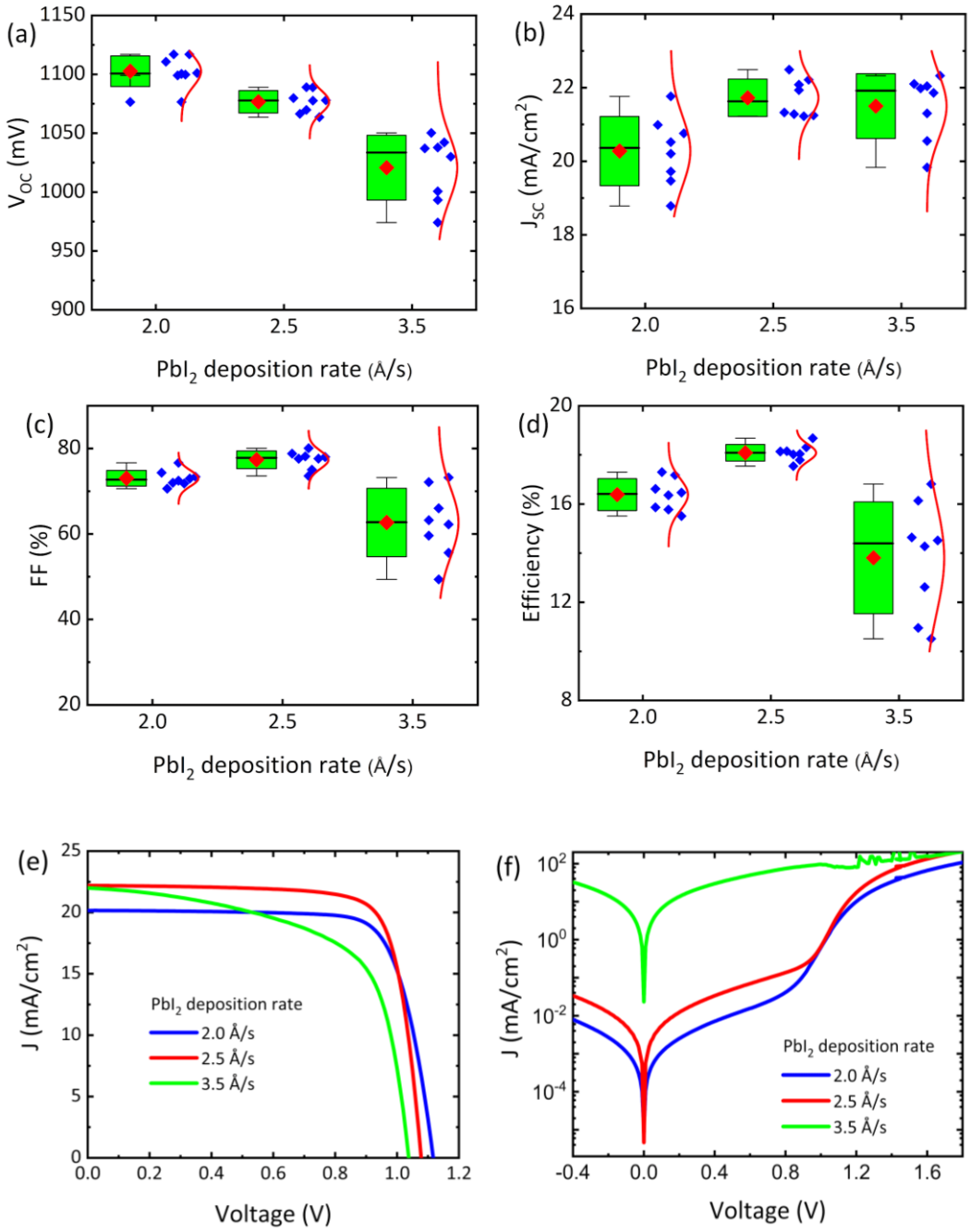

Figure 3-5 a-d) Photovoltaic parameters of the perovskite solar cells made from PbI_2 layers deposited at different evaporation rates, e) J–V curves for the best devices made using PbI_2 deposited at different evaporation rates, f) Dark J–V curves for the best devices shown in e).

Table 3-1 J–V parameter values for the best devices corresponding to Figure 3-5e.

PbI_2 rate(Å/s)	V_{OC} (mV)	J_{SC} (mA/cm^2)	FF (%)	PCE (%)
2.0	1117.0	20.2	76.7	17.3
2.5	1078.0	22.2	78.0	18.7
3.5	1042.3	22.0	73.2	16.8

3.2.3 The effect of Br^- and Cl^- and their combination

The effect of mixed halide incorporation in the perovskite structure was studied in terms of crystallinity, morphology, and the optical properties of the perovskite layer. The concentration of MAI (35 mg/ml) was kept close to the optimized range of previously reported studies [48,57]. We named the perovskite after the halides present in the MA-halide solution. When the solution is composed of MAI only, the resultant perovskite is denoted as MAPI. If MACl (5 mg/ml) or MABr (10 mg/ml) is added, the perovskite is named MAPI-Cl or MAPI-Br, accordingly. Provided both MACl (5 mg) and MABr (10 mg) are added, the perovskite is denoted as MAPI-BrCl. The surface and cross-sectional SEM images of MAPI, MAPI-Cl, MAPI-Br, and MAPI-BrCl are shown in Figure 3-6a-h. The corresponding XRD patterns, absorbance, EQE spectra, and J–V curves and data are presented in Figure 3-7a-d and Table 3-2. The perovskite layer was unsmooth with grains in the form of humps with heterogeneous sizes in MAPI (Figure 3-6a) which might be due to relatively high strain between the crystallites in MAPI [76]. Also, a 50 nm-thick PbI_2 layer remained

unreacted between MAPI and the bottom substrate as displayed in Figure 3-6b. The unreacted PbI_2 resulted in an intense XRD peak at 12.7˚ according to Figure 3-7a. Furthermore, according to External Quantum Efficiency (EQE) spectrum shown in Figure 3-7b, the device from MAPI suffered from minimal charge collection in the short wavelength region of the spectrum with a J_{SC} of 17.5 mA/cm^2 and from low FF (53.8%) (Figure 3-7d). These results suggest that the thickness of the unreacted PbI_2 layer at the light incident interface is excessive and acts as a charge collection barrier. According to Figure 3-7a, the PbI_2 (100) X-ray diffraction was less intense in the case of MAPI-Cl. Besides, as shown in Figure 3-7d, the thickness of the unreacted PbI_2 layer was reduced to ≈ 20 nm (i.e. much thinner compared with MAPI). The grains are more homogenous having a more preferential orientation compared to MAPI, as shown in Figure 3-6c-d. This is plausibly due to the inclusion of MACl, which can enhance the perovskite crystallization [77]. Moreover, Cl^- ion has a smaller ionic size (1.67 Å) than I^- (2.07 Å) [47] and therefore, Cl^- has higher diffusivity. Consequently, MACl improved the impregnation of MA-halide components into the compact PbI_2 layer in the case of MAPI-Cl. There is a considerable reinforcement in the absorbance with its edge blue-shifted from λ=780 nm to λ=750 nm as shown in Figure 3-7b. However, according to Figure 3-7c, the onset of charge collection of MAPI-Cl overlaps MAPI at λ=780 nm. This is attributed to the volatile nature of MACl. We argue that since the absorbance measurement was carried out immediately after perovskite formation, MACl was still integrated into the perovskite lattice. But it volatilized during the upcoming steps of the device fabrication which involves vacuum deposition of C_{60}, BCP, and Ag on top of the perovskite layer. In line with the EQE measurement shown in Figure 3-7c, the charge collection was enhanced significantly throughout the whole visible spectrum in contrast with MAPI. Also, there is a remarkable improvement in J_{SC} (21.3 mA/cm^2), V_{OC} (1146.3 mV), FF (77.3%) and PCE (18.9%) according to J–V curves in Figure 3-7d. These results show the beneficial role of MACl inclusion in an effective reaction between PbI_2 and MA-halide solutes. Similarly, the addition of MABr enhanced the transformation of the PbI_2 layer into perovskite, which is revealed by

the suppressed PbI_2 (100) diffraction in MAPI-Br diffractogram (Figure 3-7a). This is further proven by the cross-sectional SEM image in Figure 3-6f where no residual interfacial PbI_2 layer is traceable in contrast with MAPI and MAPI-Cl. According to the SEM image of the sample surface in Figure 3-6e, the crystallites appeared relatively small but uniform in the case of MAPI-Br. The enhanced conversion of the PbI_2 layer into perovskite is likely due to the more diffusive nature of Br^- than I^- into the PbI_2 layer [78]. As demonstrated in Figure 3-7b-c, the absorption edge is at λ=750 nm in both absorbance and EQE measurements for MAPI-Br, entailing strong and nonvolatile alloying of MABr (unlike MACl) in the perovskite structure. This is due to 7 times stronger bonding of Pb^{2+} with Br^- than I^- [79]. According to Figure 3-7b-d, MAPI-Br showed enhanced EQE and J–V characteristics in contrast with MAPI. The minimum PbI_2 (100) diffraction peak intensity was observed in MAPI-BrCl (Figure 3-7a). The grains appeared large, uniform, compact and perpendicularly oriented in MAPI-BrCl as shown in Figure 3-6g-h. Also, no visible trace of the unreacted PbI_2 layer at the bottom of the perovskite layer shows that the concurrent inclusion of Br^- and Cl^- in the MA-halide solution significantly improved the crystallization of perovskite. The absorbance of MAPI-BrCl surpassed the other types of perovskite with single/double halides (Figure 3-7b). According to Figure 3-7c, the EQE exceeded 90% demonstrating a superior J_{SC} of 22.1 mA/cm^2. MAPI-BrCl also showed higher FF (79.6%) and PCE (19.1%) as compared with MAPI, MAPI-Br, and MAPI-Cl (Figure 3-7d). Thus, the most efficient conversion of the PbI_2 layer into perovskite took place when the MA-halide solution contained MAI, MABr, and MACl altogether. Nevertheless, the highest V_{OC} (1146.3 mV) was achieved with MAPI-Cl. This is ascribed to the whiter phase PbI_2 regions on the surface of MAPI-Cl and a thin unreacted PbI_2 layer between the perovskite and the substrate [75] which is at the expense of J_{SC} loss as compared to MAPI-BrCl. The same holds for the relatively high V_{OC} (1107.1 mV) with thicker PbI_2 in the case of MAPI costing a dramatic loss in J_{SC} (17.5 mA/cm^2) and FF (53.8%). Considering all the observations above, we chose MAPI-BrCl as the champion perovskite type in this study as it showed successful utilization of MACl and MABr as recrystallizing

agents to fabricate perpendicularly oriented grains of perovskite with the highest efficiency.

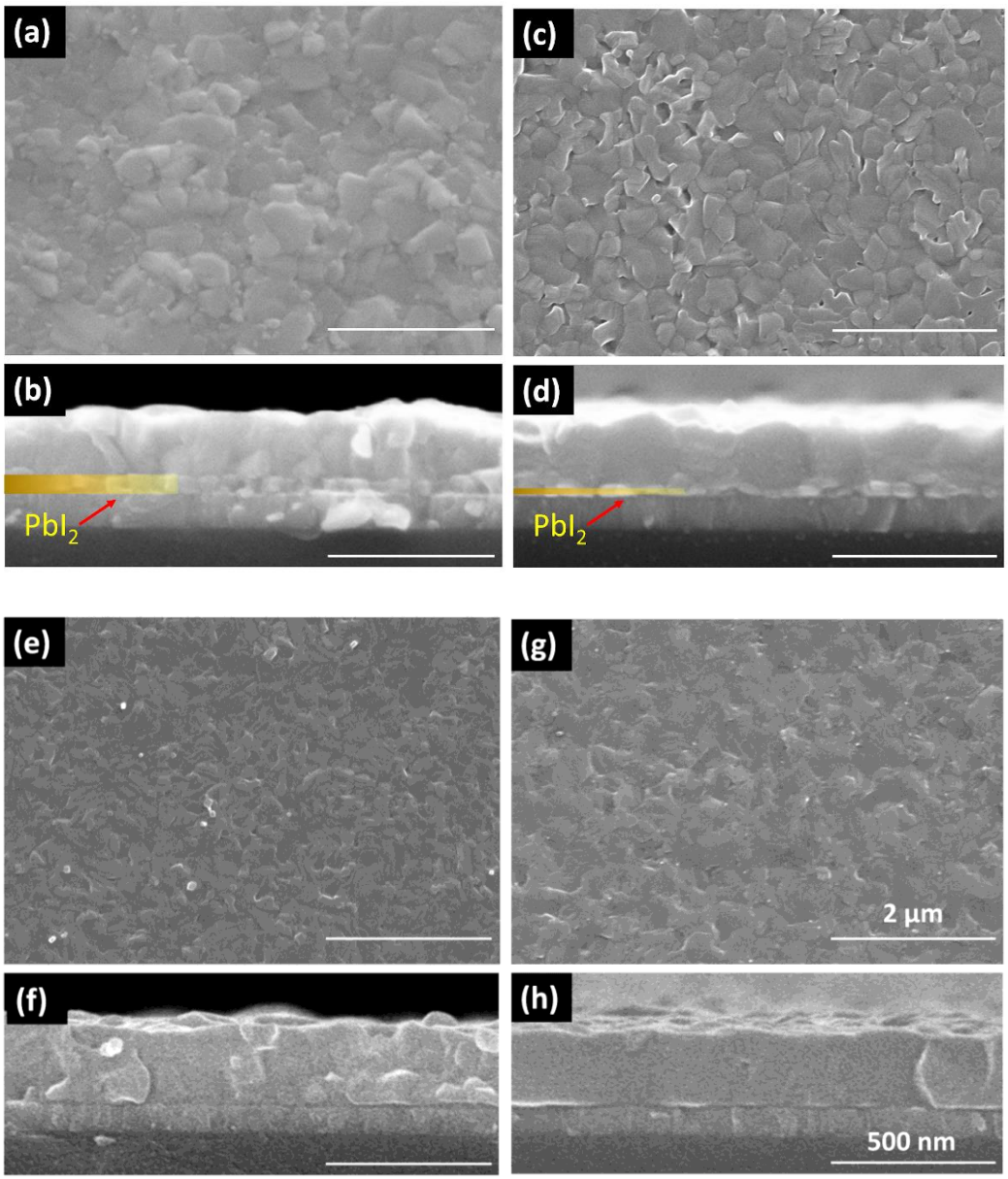

Figure 3-6 SEM surface and cross-sectional images for a, b) MAPI, c, d) MAPI-Cl, e, f) MAPI-Br, and g, h) MAPI-BrCl.

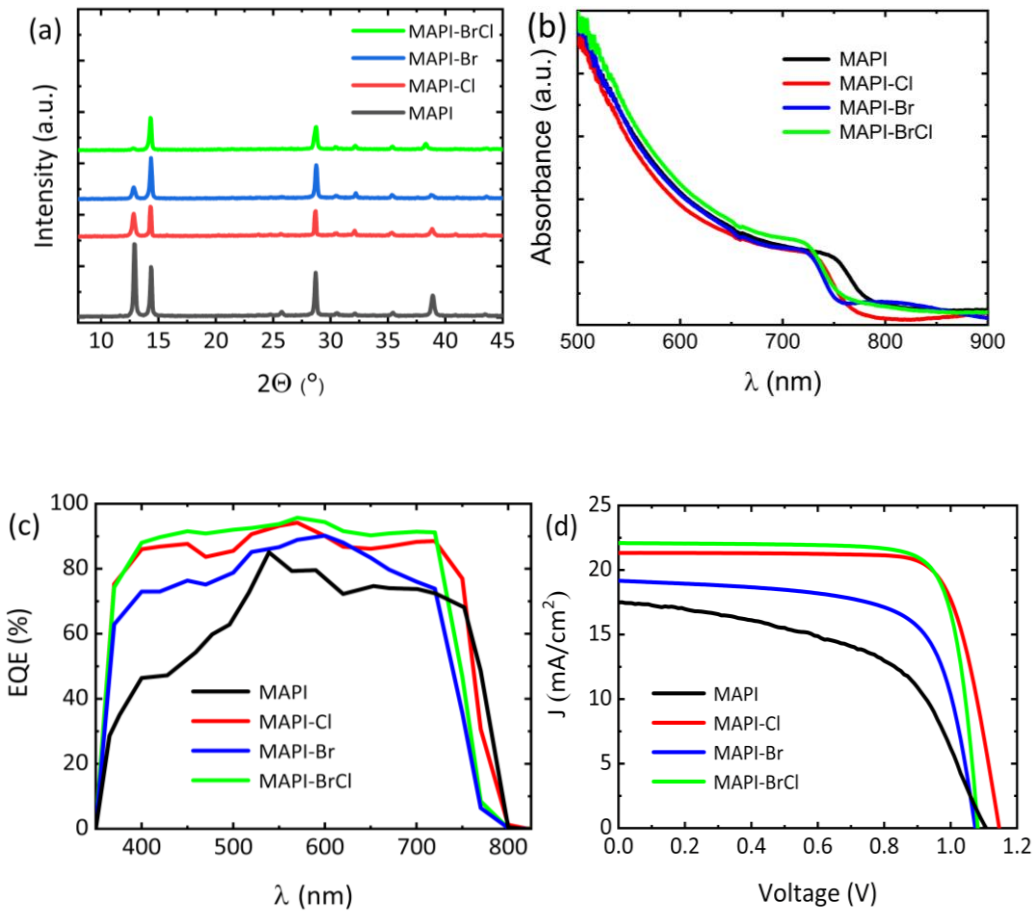

Figure 3-7 a) XRD patterns, b) Absorbance spectra, c) External quantum efficiency, and d) J–V curves for the perovskite solar cells with single, double and triple halides in the MA-halide solution.

Table 3-2 The performance details corresponding to Figure 3-7d.

Perovskite)	**Voc (mV)**	**Jsc (mA/cm^2)**	**FF (%)**	**PCE (%)**
MAPI	1107.1	17.5	53.8	10.4
MAPI-Cl	1146.3	21.3	77.3	18.9
MAPI-Br	1074.0	19.3	68.7	14.2
MAPI-BrCl	1081.9	22.1	79.6	19.1

The concentration of MACl was fixed at 5 mg/ml in all the MA-halide solutions as more quantities of MACl resulted in poor crystal structure with a PbI_2 rich perovskite layer according to XRD results shown in Figure 3-8. This is also in line with a previous study regarding MACl concentration [74].

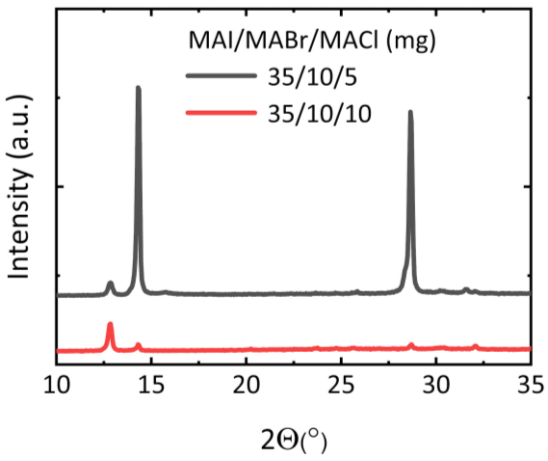

Figure 3-8 XRD patterns for MAPI-BrCl with 5 and 10 mg of MACl.

However, it was intriguing to investigate MABr/MAI molar ratio to better engineer the MA-halide solution to optimize the performance of MAPI-BrCl based perovskite solar cells. The MABr/MAI molar ratio was varied from 0.36 to 0.41, 0.46, 0.51, 0.56, 0.61 and 0.71. Increasing the ratio from 0.36 to 0.71 shifted the absorbance edge from 755 (1.64 eV) to 730 nm (1.7 eV) as shown in Figure 3-9a. According to Figure 3-9b, the amplitude of the blue-shift in the bandgap was not linear and varied when the molar ratio of MABr/MAI. The average associated V_{OC} increased from 1083.9 mV to a maximum value of 1136.7 mV as the MABr/MACl molar ratio increased from 0.36 to 0.56 (Figure 3-10), in agreement with the trend for the expected values based on Shockley-Queisser (SQ) limit at the associated bandgap of every MABr/MAI ratio (Figure 3-12). However, the magnitude of the difference between the SQ and average values ($V_{OC}^{SQ} - V_{OC}^{AVE}$) shown in Figure 3-12, increased more as the MABr/MAI ratio increased from 0.41 to 0.51. When the ratio was further increased to 0.71, not only the average V_{OC} dropped from 1136.7 to 1114.9 mV but also, $V_{OC}^{SQ} - V_{OC}^{AVE}$ increased. Since the minimum value of $V_{OC}^{SQ} - V_{OC}^{AVE}$ belongs to the MABr/MAI ratio of 0.41, one can claim that the non-radiative recombinations are minimal at this ratio. On the other hand, the trends in the average J_{SC}, FF, and PCE also, follow the predicted SQ trends based on the bandgap at each MABr/MAI ratio (Figure 3-12). The highest average J_{SC} (20.8 mA/cm^2) and FF (80.7%) were measured when the ratio was 0.41 and 0.61,

respectively. Above all, the minimum difference between the SQ limit and average values of V_{OC}, $J_{SC,}$ and PCE was measured when the ratio was 0.41. This is most likely representative of the suppressed non-radiative recombinations at the bulk and/or the interfaces when the ratio is 0.41. In addition, the minimum data scattering occurred at the same ratio in Figure 3-10 and Figure 3-12, which indicates the highest reproducibility. The best average efficiency (18.7 %) and record efficiency (19.8 %) were achieved when the ratio was equal to 0.41, as depicted in Figure 3-11.

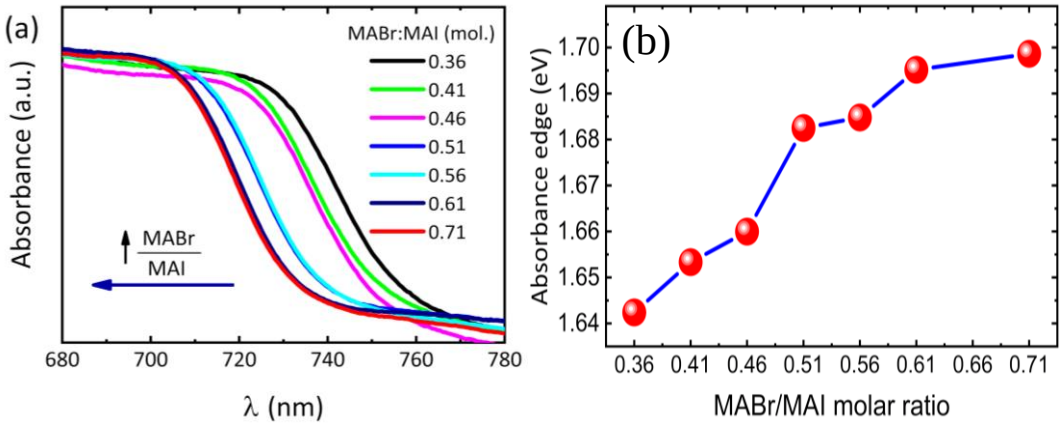

Figure 3-9 a) Absorbance spectra of perovskite for different MABr:MAI molar ratio in the MA-halide solution, b) the absorbance edges of the samples in (a).

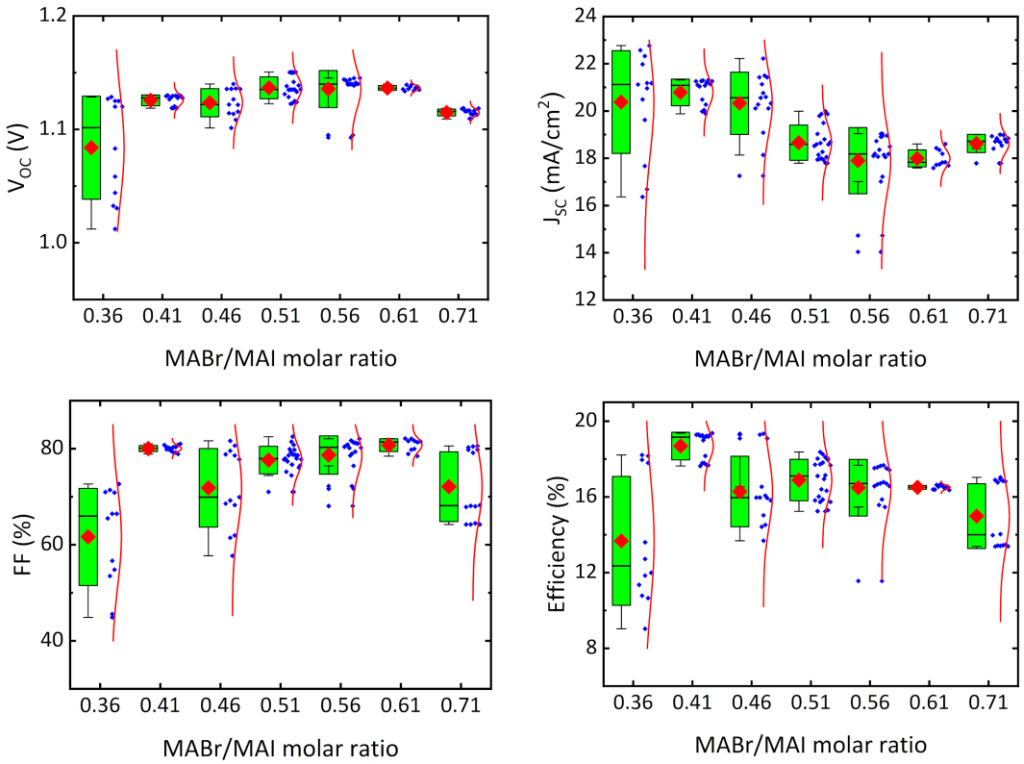

Figure 3-10 Photovoltaic parameters of the perovskite solar cells made with different MABr:MAI molar ratios between 0.36 to 0.71 in the MA solution. The amount of MACl was kept constant in all solutions.

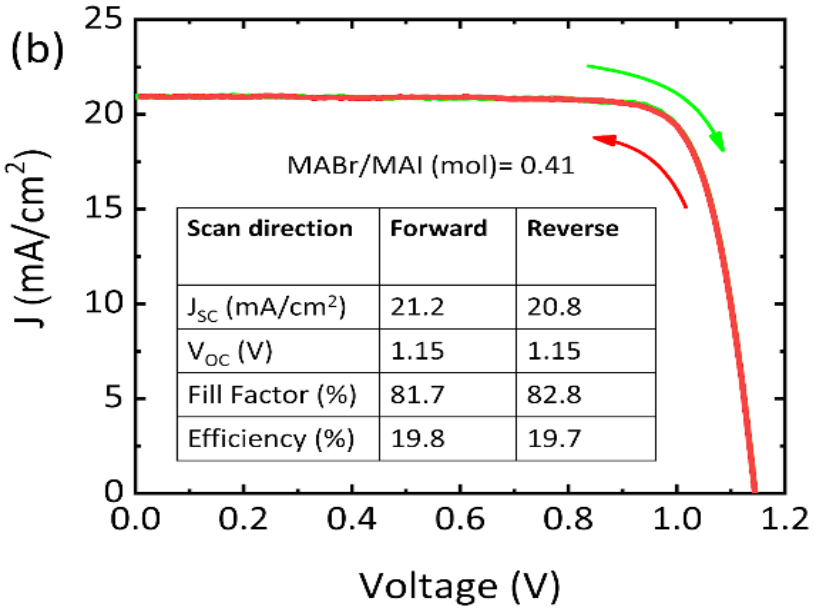

Figure 3-11 The J–V characteristic curve and data for the champion cell with an MABr/MAI molar ratio of 0.41.

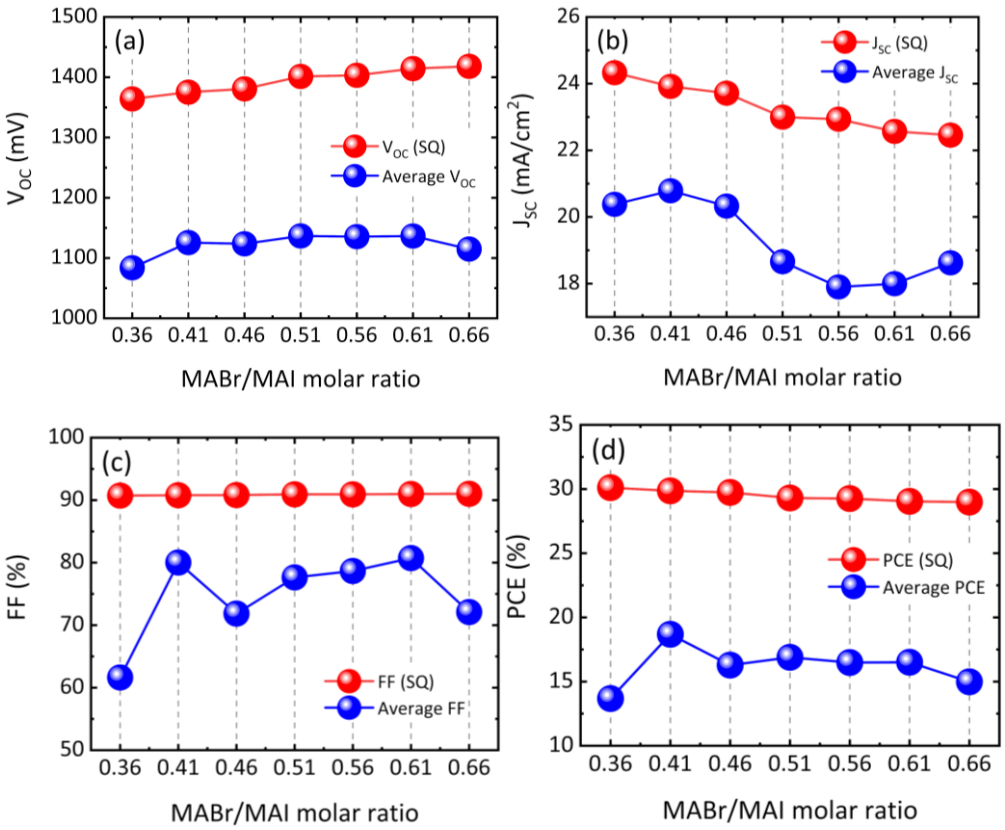

Figure 3-12 Shockley-Queisser limit and average values for V_{OC} (a), J_{SC} (b), FF (c) and PCE (d).

The stability of the encapsulated devices from MAPI-Br, MAPI-Cl, and MAPI-BrCl were measured tracking J–V characteristics of the devices every 15 minutes under constant 1 Sun illumination while held at room temperature. The results are shown in Figure 3-13. MAPI-Br and MAPI-BrCl respectively demonstrated maximum stability in all the J–V characteristic data with a 6% and 10% increase of their starting efficiency over 90 hours of constant operation. Conversely, MAPI-Cl turned out to be unstable due to J_{SC} and FF loss over time. Thus, despite the enhanced crystallization of perovskite and improved efficiencies of MAPI-Cl, the exclusion of Br- was at the expense of stability especially in the FF of the devices. In short, in view of the J–V data and stability analyses, the incorporation of both Br^- and Cl^- in the MA-halide solution was found to be optimal in achieving the best device performance as well as sustaining the device stability under working conditions which is in agreement with the previous studies [64].

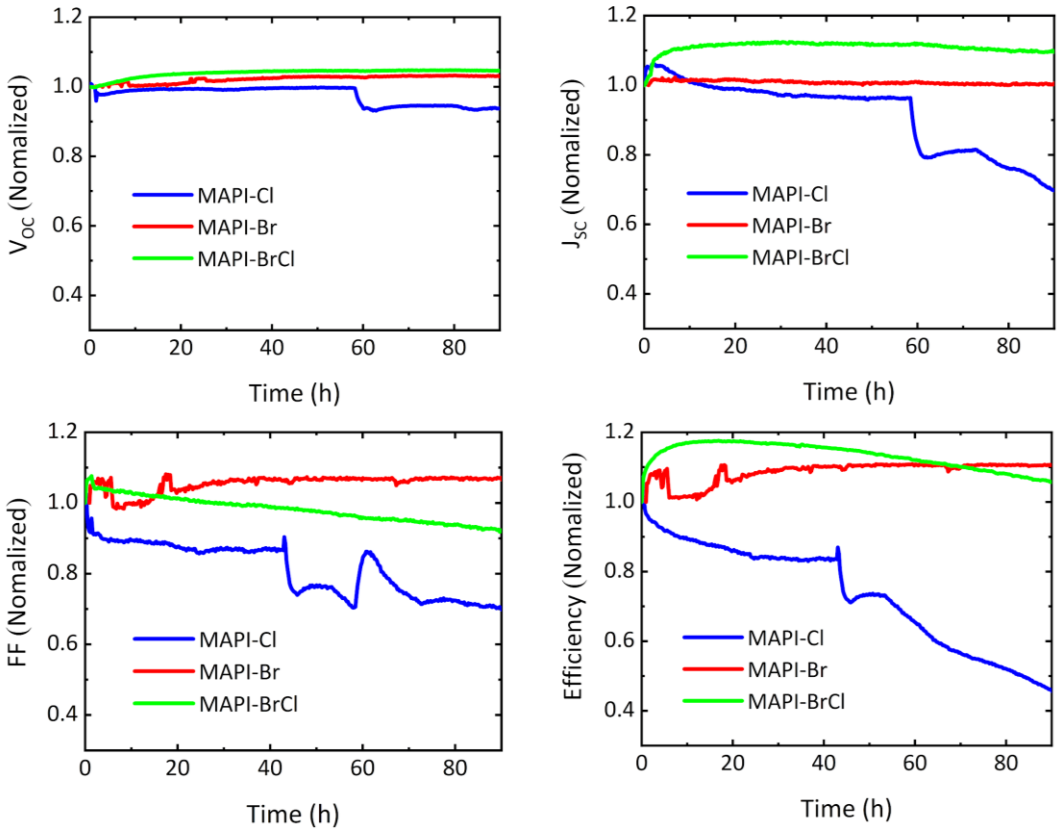

Figure 3-13 Stability analysis for MAPI, MAPI-Cl, MAPI-Br, and MAPI-BrCl based on IV measurements taken under continuous one sun irradiance.

3.3 Conclusions

In sum, mixed halide perovskite solar cells were successfully fabricated using a hybrid vapor-solution technique for the first time. A highly uniform perovskite layer was achieved owing to the vapor deposition of the initial PbI_2 layer in the first step. The addition of Br^- and Cl^- into the MA-halide solution during the second step ensured a robust permeation of MA-halide compounds into a dense PbI_2 film. It also provided effective control over the crystallization of perovskite with preferential grains and power conversion efficiencies as high as 19.8%. The highest reproducibility and minimum deviation from the expected SQ limit values were

accomplished through fine-tuning the MABr/MAI ratio in the MA-halide solution. The optimum performance/stability of the solar cells was achieved with the triple halide perovskite.

CHAPTER 4

SPUTTERED INTRINSIC AND DOPED NiO_X HOLE TRANSPORT LAYERS FOR PLANAR PEROVSKITE SOLAR CELLS

NiO_X as a hole transport layer has been extremely popular in p-i-n perovskite solar cells (PSCs) due to its wide bandgap, matched band structure with perovskite, and stability [80]. Radiofrequency (RF) magnetron sputtering is a technique offering control on the stoichiometry and morphology of the deposited thin films with doping capability, high purity, and reproducibility. As a result, it has been used as a scalable methodology to fabricate NiO_X films in PSCs during recent years. We used the same methodology here to fabricate an efficient NiO_X layer in planar PSCs. Our results showed that Ar-partial pressure (APP) during the sputtering defines the optical and electrical properties of NiO_X. Also, doping NiO_X with Cu was conducted during this study proving sputtered Cu doped NiO_X as an efficient HTL in PSCs.

4.1 Introduction

In the p-i-n configuration of PSCs, the hole transport layer (HTL) must fulfill both optical and electrical requirements to render high photovoltaic efficiencies. Therefore, the choice of the material, as well as the fabrication scheme, are extremely important. A variety of fabrication techniques for NiO has been used including sol-gel, combustion methods, pulsed laser deposition (PLD), atomic layer deposition (ALD), sputtering, e-beam evaporation and electrochemical deposition [81823283848586]. Among all, RF magnetron sputtering is one of the popular techniques mainly due to its straightforward application in the industry [87]. Also, sputtering outweighs other methodologies due to a multitude of advantages such as stoichiometric control, highly pure film products, thickness control, uniform coating over large areas and doping capability. To fabricate NiO film, different schemes of sputtering have been

used. For instance, a Ni layer was deposited using DC-sputtering and later, the film was oxidized using O_2 or O_3 flow treatment. Also, reactive sputtering using Ni target and O_2 flow has been used. Direct sputtering of NiO has been a favorable choice, as well. During NiO sputtering, the sputtering power and APP define the number of oxygen interstitials (I_O) and Ni vacancies (V_{Ni}) within the film which in turn, determine the optical, electrical and morphological properties of the final NiO_X layer. Islam *et al* changed the sputtering power to tune the work function of NiO_X [88]. In another study, the same group changed APP determining the ratios of Ni^{3+}/Ni^{2+} in the NiO_X lattice and thereby on the optical transmittance of NiO_X [32]. As an important inherent property of the magnetron sputtering, varying APP under a constant sputtering power entails a change in the deposition rate of the sputtered material. Besides, any minute change in the location or the angle of the target with respect to the substrate position, modifies the deposition rate, dramatically. To rule out such unwanted effects, we kept the rate constant tracking the effects of APP and sputtering power, independently. According to our studies, increasing APP from 2×10^{-3} torr to 16×10^{-3} Torr increased the Ni^{3+}/Ni^{2+} ratio and I_O count in the NiO_X lattice. Therefore, the conductivity of the final film increased with APP. However, it caused a decrease in the fill factor (FF) and V_{OC} of the corresponding PSCs. In addition, annealing the NiO_X layer was found effective in improving the FF of the PSCs [83,89]. The improvement was found irrelevant to the crystallinity of NiO_X. A thin layer of Poly-TPD atop the NiO_X enhanced the short circuit current (J_{SC}) of the PSCs. Annealing the NiO_X layer together with a Poly-TPD interlayer, improved the average PCEs by 2.5%. The effect of the NiO_X deposition rate was also studied. After defining the optimal rate and APP relying on the statistical J–V analysis, surface passivation of NiO_X by sputtered CuO and SiO_2 was investigated. Also, the effect of Cu dopant on the optoelectronic properties of the NiO_X layer was investigated. An atomic percentage of 1.8% for Cu within NiO_X, was found optimum with maximum V_{OC} and power conversion efficiencies (PCE).

In this chapter, X-ray photoelectron spectroscopy (XPS), X-ray diffractometry (XRD), Spectroscopic ellipsometry, UV–VIS spectrometry and space charge limited

current (SCLC) analysis were employed to characterize the sputtered undoped and Cu doped NiO_X layers. In the first section of the report, the effect of APP was investigated on the undoped NiO_X. Then, the effect of Cu dopant on NiO_X optoelectronic properties was studied.

4.2 Results and Discussions

4.2.1 Post-treatment of NiO_X and prerequisites

Although NiO has been a popular HTL enhancing the stability of perovskite solar cells, its surface is vulnerable to the ambient air. Ultraviolet photoelectron spectroscopy (UPS) was devised to measure the work function (ϕ) and valence band maximum (VBM) of the as-deposited and aged sputtered NiO_X/ITO as shown in Figure 4-1a. The NiO_X/ITO aged 18 hours in ambiance with a temperature of 27 °C and humidity of 38%. The work function decreases from 4.54 to 4.43 eV when NiO_X aged for 18 hours. Also, due to aging, the Fermi level difference with VBM shifts from 0.91 to 0.96 eV indicating a less p-type characteristic of the exposed NiO_X. According to the XPS measurement shown in Figure 4-1b, the concentration of carbon in NiO_X increased from 9.3 to 14.2% after aging. Therefore, we ascribe the reduction in ϕ and Fermi level-VBM difference, to the carbonaceous adsorptions to the surface of NiO_X. It has been suggested in the literature that the adsorbed hydroxyl groups are also responsible for such an effect. But since the O peak from surface OH-groups is concomitant with the bulk O from Ni_2O_3 at a binding energy of 531 eV, it is not possible to conclude if the sample is OH-rich or Ni_2O_3-rich during XPS measurements. For a better resolution, we suggest the usage of angle-resolved XPS (ARXPS) which can be the subject of a future study.

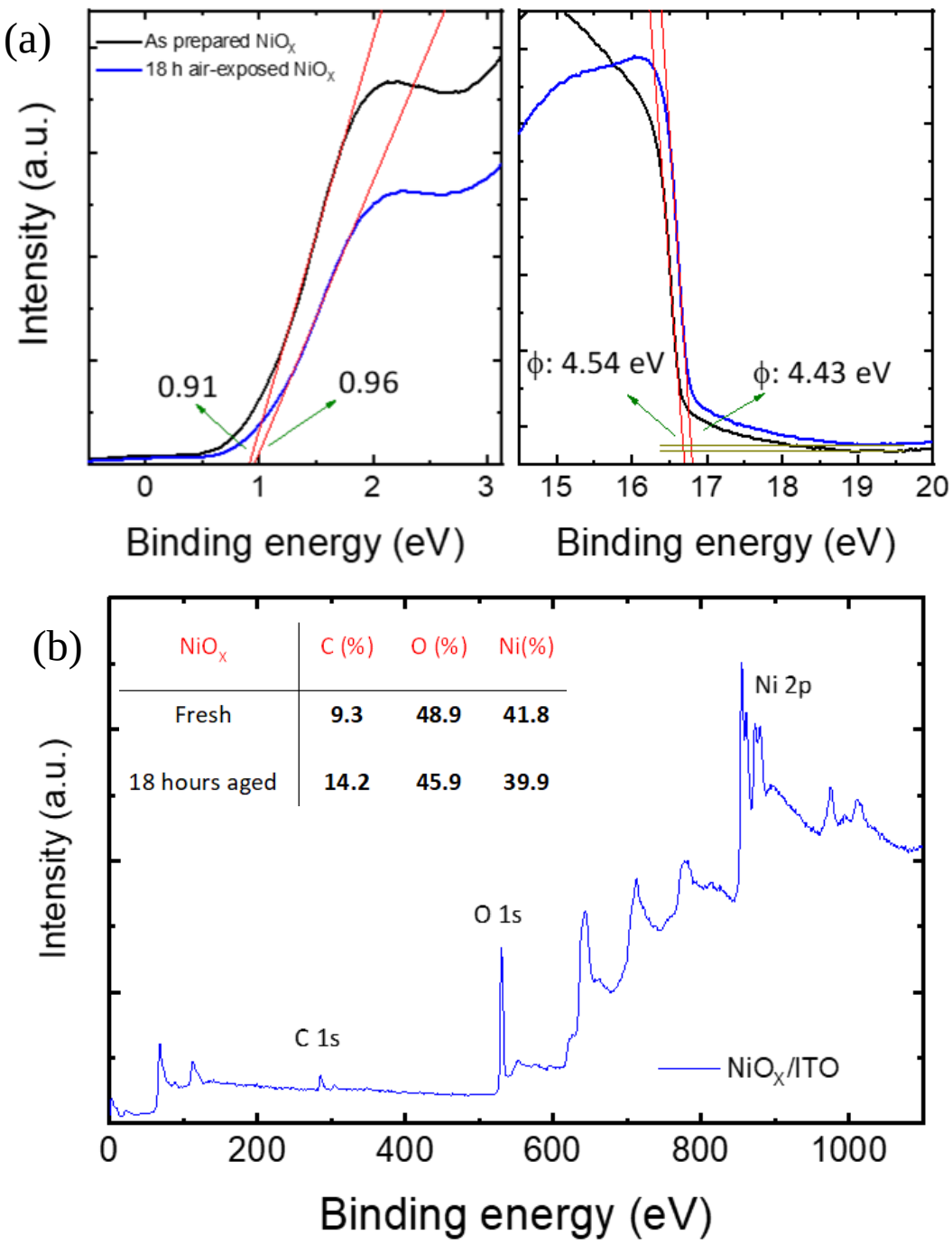

Figure 4-1 a) UPS measurement results for fresh and 18 hours aged NiO_X/ITO, b) XPS for the samples in (a).

Following the UPS results, it seems to be a must for post-treatments of NiO_X to sustain its electronic properties. Otherwise, any change in the temperature, humidity or ambiance carbon concentration may modify the surface electronic properties of NiO_X. Various organic materials have been proposed to passivate the surface of NiO_X such as F_6TCNNQ, PTZ, PFBT, n-Butylamine, SDBS, TMAH, DEA, PTAA, rGO and cysteine [19,20,89-95]. However, poly-TPD (PTPD) as a passivation layer for NiO_X has not been studied yet. Therefore, we studied the effect of annealing and surface coating NiO_X by PTPD to increase the reproducibility of the J-V characteristics of the resultant PSCs. The NiO_X samples were prepared by sputtering NiO_X at a rate of 1 nm/min under APP of 4 mTorr. The annealed samples were prepared by heating the samples at 300 °C in the air. As for PTPD /NiO_X/ITO, a chlorobenzene solution of 7 mg ml^{-1} was spin-coated atop NiO_X/ITO at 3000 rpm for 60 seconds and washed once with chlorobenzene. For studying the annealing effect, 200 nm thick NiO_X was used to increase the resolution of the XRD diffractions compared to ones coming from the bottom ITO. Annealing NiO_X was predominantly performed to remove hydroxyl or carbonaceous adsorbates from the surface of NiO_X and it did not change the crystallinity of NiO_X/ITO as evidenced by XRD results shown in Figure 4-2a. The perovskite solar cells were prepared in a p-i-n structure shown in Figure 4-2b. The perovskite layer was fabricated following the hybrid vapor-solution sequential approach. For this purpose, a 295 nm-thick PbI_2 layer was vacuum-deposited atop NiO_X/ITO followed by spin-casting an IPA solution containing MAI, MABr, and MACl. Therefore, the perovskite is denoted as MAPI-BrCl. Later, a 50 nm PCBM was formed by spin-casting a chlorobenzene solution. The samples were transferred into a vacuum chamber integrated into the glovebox and were finished by evaporating BCP (6 nm) and Ag (100 nm) as the top electrode. The J-V characteristics of the resultant devices are shown in Figure 4-2c-f. It is important to note that all J_{SC} values were corrected to the integrated external quantum efficiency (EQE) spectra.

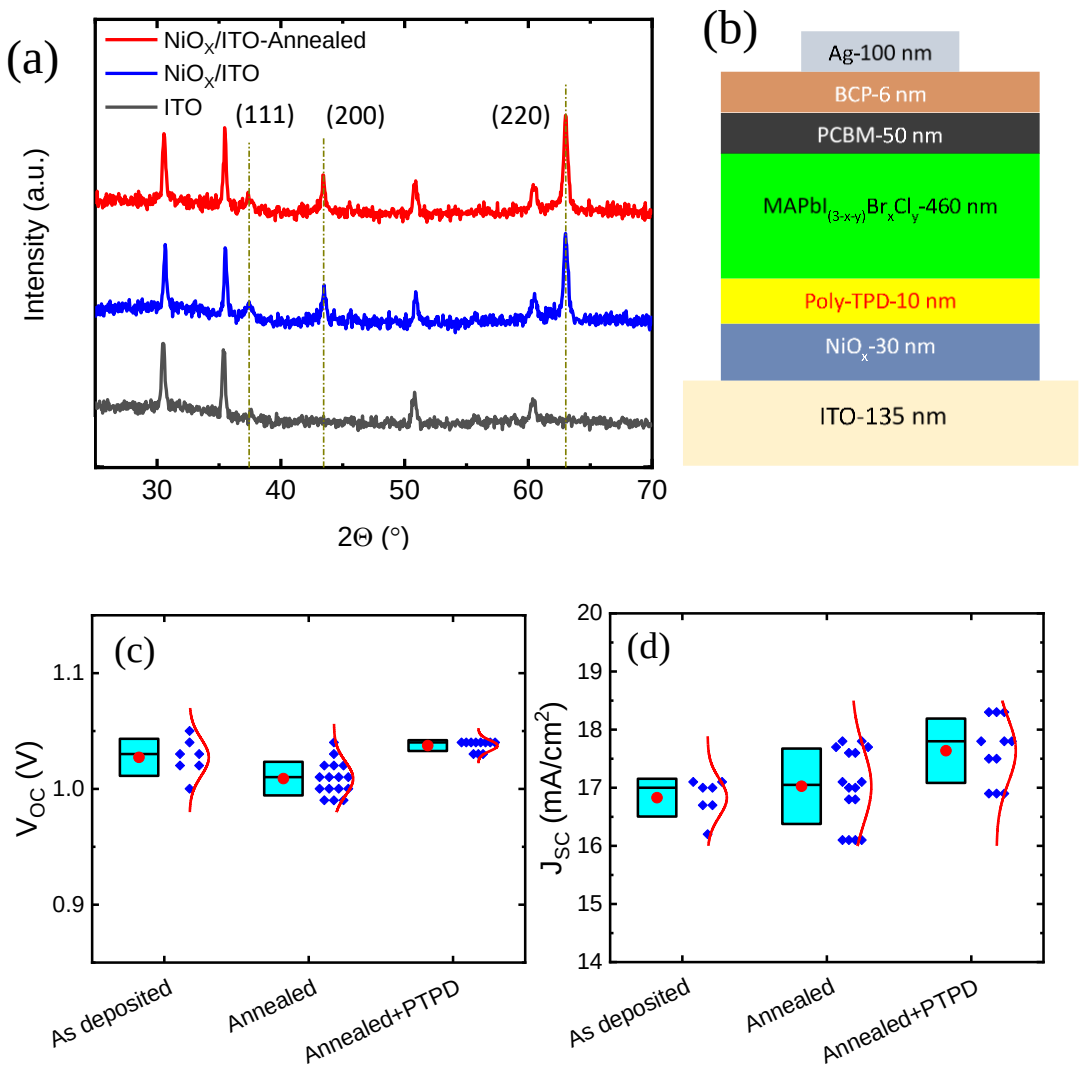

Figure 4-2 a) XRD patterns for as-deposited NiO_X/ITO and annealed NiO_X/ITO in the air at 300 °C. b) Perovskite solar cell configuration, c, d, e, f) all V_{OC}, J_{SC}, FF and PCE data for devices using as-deposited, annealed, coated with PTPD.

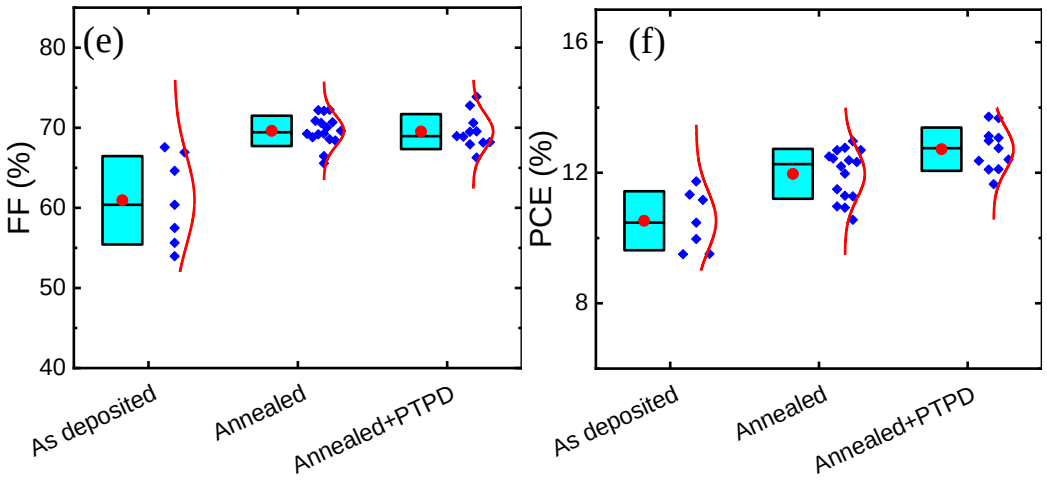

Figure 4-3 (continued).

According to Figure 4-2, annealing NiO_X improves the efficiency of the PSCs by improving the average FF from 60.9 to 70.0 %. When the annealed NiO_X samples were coated by PTPD, the average J_{SC} increased 0.6 mA/cm^2 indicating better charge collection efficiency compared to the samples without PTPD. Overall, annealing NiO_X followed by PTPD coating considerably boosted the average PCE by 2.2%. The detailed path explaining the mechanism of such improvements requires further XPS, UPS and AFM analysis, however, throughout the rest of the study all the deposited NiO_X samples were prepared following the optimization procedure presented in this section.

4.2.2 The effect of the deposition rate of NiO_X

The refractive indices of NiO_X (33 nm) deposited at 0.44, 0.70, 1.00 and 1.50 nm/min during RF magnetron sputtering under the same APP (4 mTorr) were measured using spectroscopic ellipsometry as shown in Figure 4-4a. The refractive index of NiO_X slightly increased with the deposition rate. Therefore, the optical transmittance/reflectance did not change significantly with the deposition rate of NiO_X. However, the electrical properties of NiO_X may change with the deposition

rate. According to SCLC measurements conducted for hole-only devices shown in Figure 4-4c, trap-filled limit voltage (the intersection of the two fitting lines in ohmic and trap-filled limit regions (V_{TFL})) does not change significantly with the rate. This indicates similar trap densities versus different deposition rates of NiO_X layers according to Equation 4.1. In the equation, n_{trap} denotes the trap density, ε is the relative dielectric constant of perovskite, ε_0 is the vacuum permittivity, e and L are the electronic charge and the thickness of the perovskite layer. However, the increase in the deposition rate of NiO_X under the same APP has been shown to decrease the work function (ϕ) of NiO_X/ITO. Islam *et al* proposed that this is due to an increase in the pH of the surface of NiO_X when deposited at high rates. They also showed that high deposition rates do not significantly change the crystallinity and surface morphology of NiO_X layers. The perovskite solar cells in the p-i-n structure shown in Figure 4-4f, were fabricated to investigate the effect of the NiO_X deposition rate on the optoelectronic performance of such devices. The J-V analyses for the best and all the devices are shown in Figure 4-4e-j. There is a slight drop in the average FF and J_{SC} when the deposition rate of the NiO_X is 1.5 nm/min. The average V_{OC} was the highest when the deposition rate was 0.5 nm/min. However, the difference between the deposition-rate ranges tried here is not significant.

$$N_{trap} = 2\varepsilon\varepsilon_0 V_{TFL}/(eL^2) \quad (4.1)$$

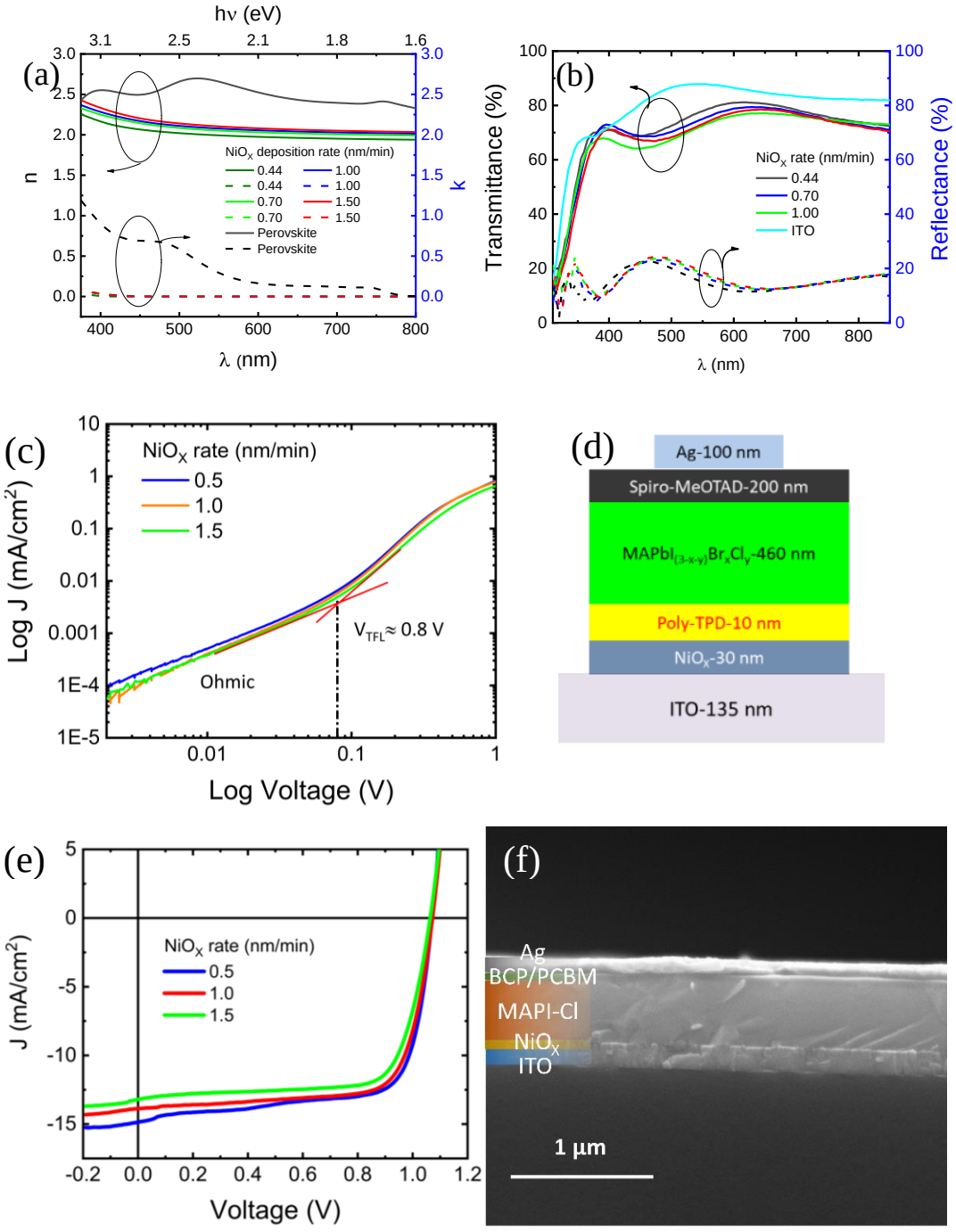

Figure 4-4 a) refractive indices of NiO_X/ITO deposited under APP = 4 mTorr, with different sputtering rates, b) Reflectance/transmittance measurement for the samples in (a), c) SCLC measurement for hole-only devices using NiO_X/ITO samples in (a), d) hole only device structure of the devices in (c), e) J-V of the best cells from samples in (a), f) cross-sectional SEM belonging to a cell in (e), g, h, I, j) all V_{OC}, J_{SC}, FF, and PCE data for devices using NiO_X/ITO samples in (a).

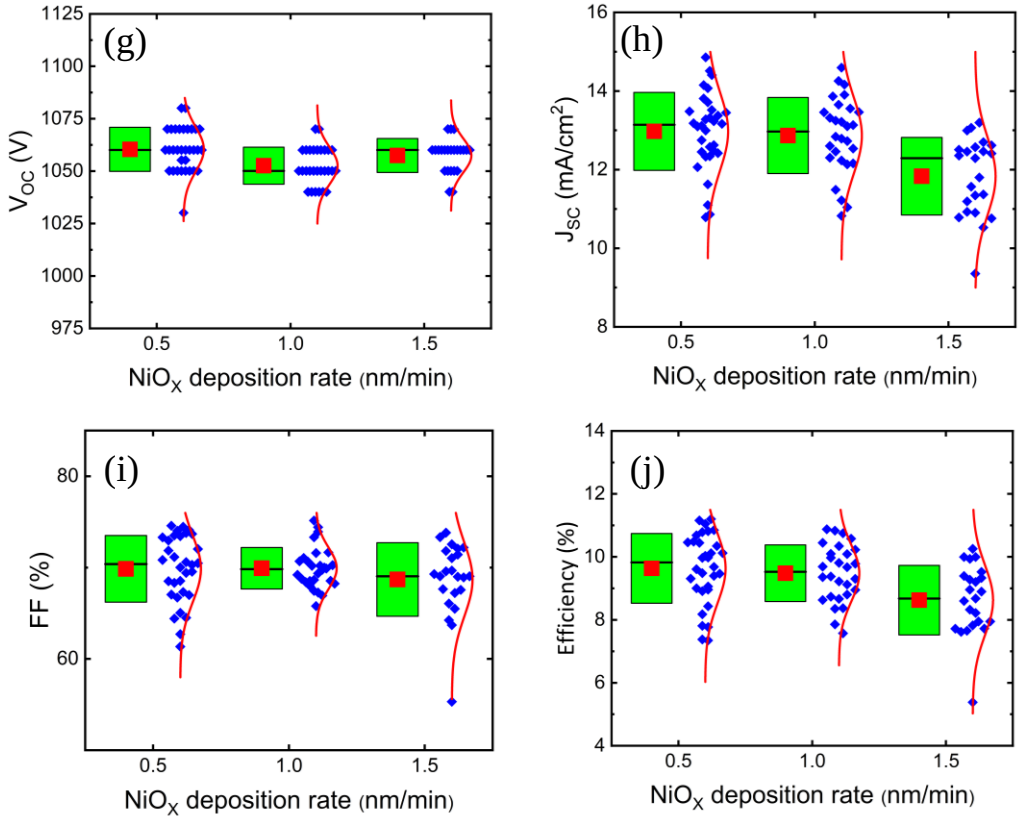

Figure 4-5 (continued).

4.2.3 The effect of Ar-partial pressure

The optoelectronic transitions in NiO as a p-type semiconductor are correlated with the energy states introduced by the intraband defects such as metal vacancies or oxygen interstitials. For instance, according to the density functional theory (DFT) calculations, nonstoichiometric NiO_X with Ni vacancies (V_{Ni}) has energy states within the bandgap at the vicinity of the valence band (VB). Therefore, Ni vacant NiO_X is equivalent to a p-type material [87]. The chemical description for the process of p doping of NiO is shown in Equation 4.2. The excess oxygen concurs with the generation of V_{Ni} and Ni^{3+}. V_{Ni} gets singly (V'_{Ni}) and doubly (V''_{Ni}) ionized creating holes in the lattice. Therefore, increasing V_{Ni} or equivalently the Ni^{3+}/Ni^{2+} ratio, not only modify the work function of NiO_X but also increases the carrier concentration. The APP has been shown to be the key parameter during RF magnetron sputtering

to tune the concentration of V_{Ni} within the lattice of NiO_X. Also, according to the XRD results in Figure 4-6a, the (200) diffraction peak at $2\theta = 42.6°$ is more intense in the case of NiO_X deposited at a low APP of 4 mTorr compared with 16 mTorr. This indicates a preference in (200) crystal orientation of NiO_X deposited at low APPs. If the sputtering power is kept constant, increasing the APP reduces the Ni^{3+}/Ni^{2+} ratio exacerbating the electrical properties of NiO_X. On the other hand, the transmittance of NiO_X/ITO improves with APP. As a result, there seems to be a certain degree of APP fulfilling both the optical and electrical requirements of NiO_X as an efficient hole transport layer (HTL) in a perovskite solar cell. Islam et al suggested an APP of 26 mTorr due to its high optical transmission and a thickness of 70 nm for optimal PCEs. To our knowledge, there are two crucial points usually overlooked in the literature regarding the optical characterization of NiO_X. Firstly, the mere transmittance measurement of NiO_X/ITO is not representative of the optical parasitic absorption of NiO_X as it may be overshadowed by the reflection losses of NiO_X/ITO. Therefore, in this study, depending on the sputtering APP, transmittance, reflectance and the consequent absorbance spectra for NiO_X/ITO were measured for an APP range between 2 and 16 mTorr as shown in Figure 4-6c, and e. On one hand, increasing APP reduces the absorbance of NiO_X/ITO. On the other hand, increasing APP intensifies the reflectance. Therefore, the loss in the transmittance of NiO_X/ITO is due to not only the parasitic absorption but also the reflection losses. It is worthwhile to note that the bandgap (Eg) of NiO_X increases from 3.54 to 3.69 eV when APP increases from 2 to 16 mTorr according to the Tauc-plot analysis shown in Figure 4-6d. The pronounced reflection loss with APP is elucidated following the Fresnel equation and the refractive index (n) of NiO_X measured by spectroscopic ellipsometry as shown in Figure 4-6b. The higher the refractive index difference between NiO_X and air ($n_{NiOx} - n_{air}$), the higher the reflection from NiO_X/ITO. n_{NiOx} decreases from 2.33 to 1.79 (λ= 632.8 nm) when the APP is increased from 2 to 16 mTorr. Since $n_{air} = 1$ (λ= 632.8 nm), the reflectance decreases with APP. Secondly, the optical properties of any layer to be used in a stacked optoelectronic device such as PSCs must also be analyzed according to the refractive indices of the adjacent

layers to account for the interferences in the sack [96]. Therefore, the refractive indices of perovskite rather than air were considered to explain the reflection losses from MAPI-BrCl/NiO_X/ITO as shown in Figure 4-6a. The minimum difference between the refractive index of NiO_X and MAPI-BrCl belongs to the NiO_X deposited at 2 mTorr. This difference maximizes with APP. Therefore, despite a slight increase in the parasitic absorption (discussed above), low APP is actually beneficial to diminish the reflection losses in the case of MAPI-BrCl/NiO_X/ITO. In short, we argue that the most straightforward method to determine the optimum NiO_X from an optical perspective is to measure the reflection of a full device consisting of all the layers. Therefore, we measured the reflection (R) off the Ag/BCP/PCBM/Perovskite/NiO_X/ITO stack with NiO_X deposited under different APPs and used Equation 4.3 to calculate the photocurrent (J_{ph}) as shown in Figure 4-6f.

$$2Ni^{2+} + (½)O_2 \rightarrow O^{2-} + 2Ni^{3+} + V_{Ni}$$

$$V_{Ni} \rightarrow \dot{V}_{Ni} + h^* \qquad (4.2)$$

$$\dot{V}_{Ni} \rightarrow \ddot{V}_{Ni} + h^*$$

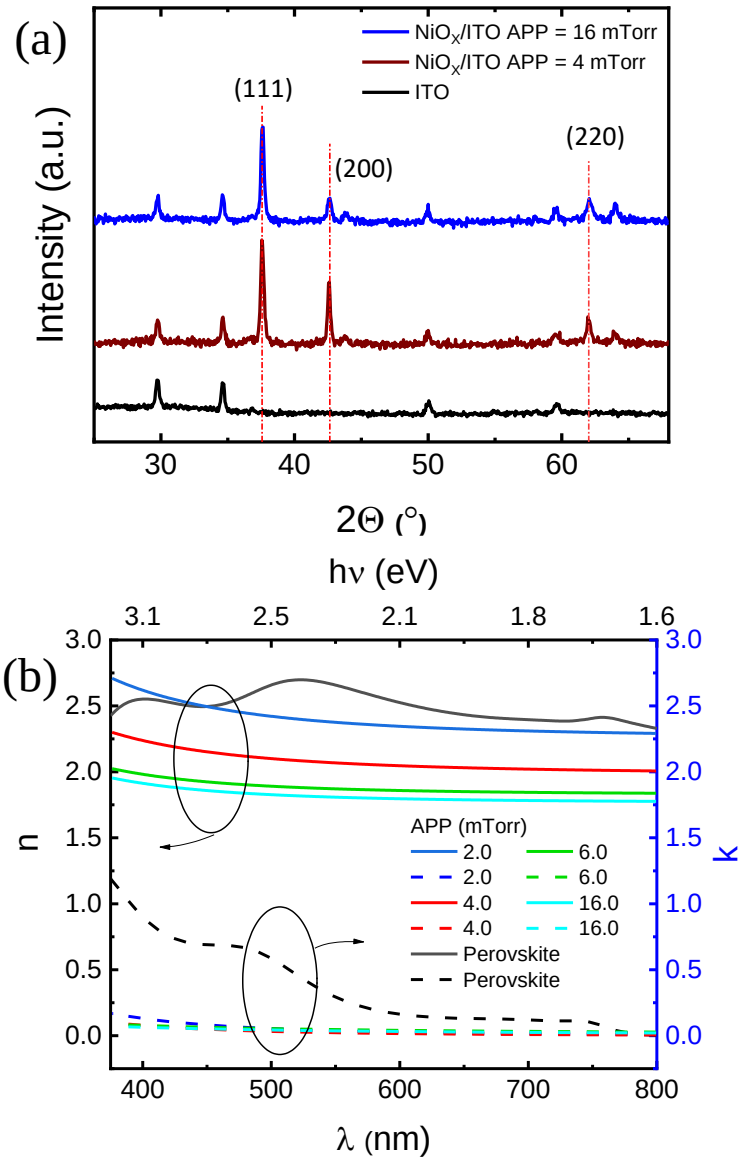

Figure 4-6 a) XRD patterns for NiO_X/ITO deposited under 4 and 16 mTorr of APP, b) refractive indices measured by spectroscopic ellipsometry for NiO_X/ITO samples deposited under APP of 2, 4, 6, and 16 mTorr, c) Reflectance/Transmittance for the samples in (b), d) Tauc plot for samples in (b), e) Absorbance spectrum for samples in (b), f) 1-R and the integrated Jph for full devices of (b) using 350 nm-thick perovskites, g) 1-R and the integrated Jph for full devices of (b) using 460 nm-thick perovskite.

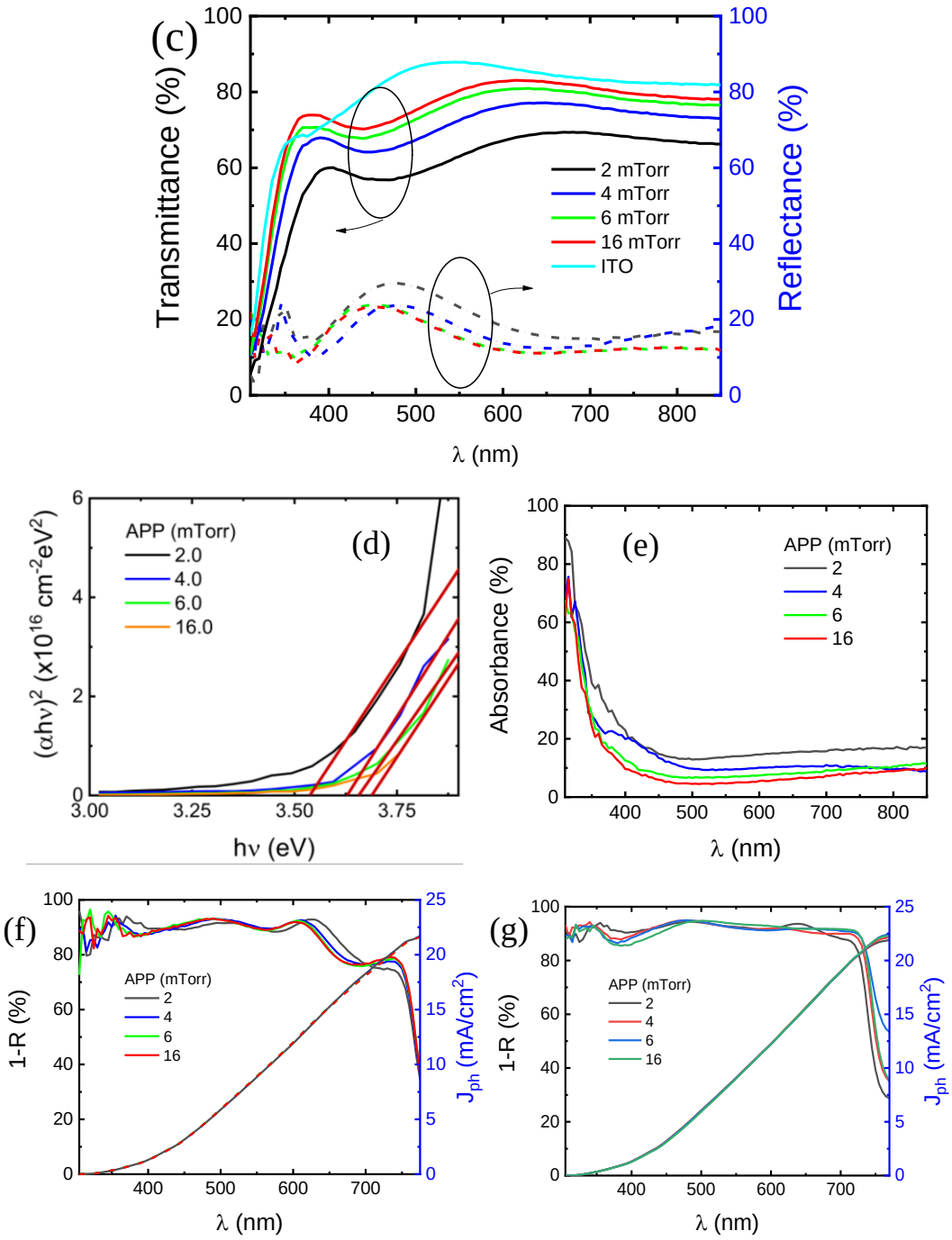

Figure 4-7 (continued).

$$Jph = q \int \varphi(\lambda)\,(1 - \mathrm{R}(\lambda))\,\mathrm{d}\lambda \qquad (4.3)$$

In the equation above, φ (λ) denotes the A.M 1.5 photon flux. As shown in Figure 4-6f, in the case of a 350 nm-thick perovskite layer, J_{ph} is 21.64 mA/cm^2 when APP

is 16 and 6 mTorr and increases only by 0.04 and 0.02 mA/cm^2 with reduced APP to 4 and 2 mTorr, respectively. But when the perovskite layer is 460 nm, the overall reflection loss is mitigated in the red spectrum. J_{ph} boosts from 21.92 to 22.36 mA/cm^2 when the APP is increased from 2 to 16 mTorr. The highest J_{ph} (22.53 mA/cm^2) is achieved when the APP is 6 mTorr as shown in Figure 4-6g. Therefore, strictly speaking, the reflection losses of NiO_X does not linearly follow the APP during RF magnetron sputtering. In sum, the electrical and interface properties of NiO_X deposited under different APPs seems to outweigh the optical properties. According to SCLC measurements for hole-only devices shown in Figure 4-8a-b, V_{TFL} increases dramatically from 0.085 to 0.305 V when the APP is changed from 2 to 16 mTorr. According to Equation 4.1, this corresponds to growing trap density with the APP. The Ni^{3+}/Ni^{2+} ratio during XPS measurements has widely been used in the literature to qualitatively evaluate the p-conductivity of NiO_X[32,97,83]. We argue that this measurement can be misleading. According to references [32], the NiO_X sample fabricated at low APPs (2 mTorr) has a higher Ni^{3+}/Ni^{2+} ratio. However, the oxygen peak at 531 eV binding with Ni^{3+} is less intense than the NiO_X sample deposited under 16 mTorr of APP as demonstrated in Figure 4-8c. This contradiction can be explained by the fact that XPS is based on the photoelectrons ejected from the top 5-10 nm of the sample surface. Provided the number of hydroxyls may differ from sample to sample due to their different surface properties, which would modify the oxygen and Ni peak shapes during XPS[98–100]. Therefore, for reliable interpretation of Ni^{3+}/Ni^{2+} ratio, angle-resolved XPS measurements are suggested. According to average J-V characteristic values shown in Figure 4-8d-g, the average V_{OC} decreases from 1.068 to 1.041 V when APP changes from 2 to 16 mTorr. The J_{SC} does not change considerably with the APP, but FF is highest at low APP = 2 mTorr. Therefore, the highest average PCE value was obtained with APP = 2 mTorr. The comparison between the APP of 2 and 4 mTorr was made in another batch with the results shown in Table 4-1. The devices made using NiO_X deposited under APP = 4 mTorr, outperformed APP = 2 mTorr exhibiting higher average V_{OC} and FF. The

low trap density in the case of low APP is plausibly the reason for the high average V_{OC} achieved with low APPs.

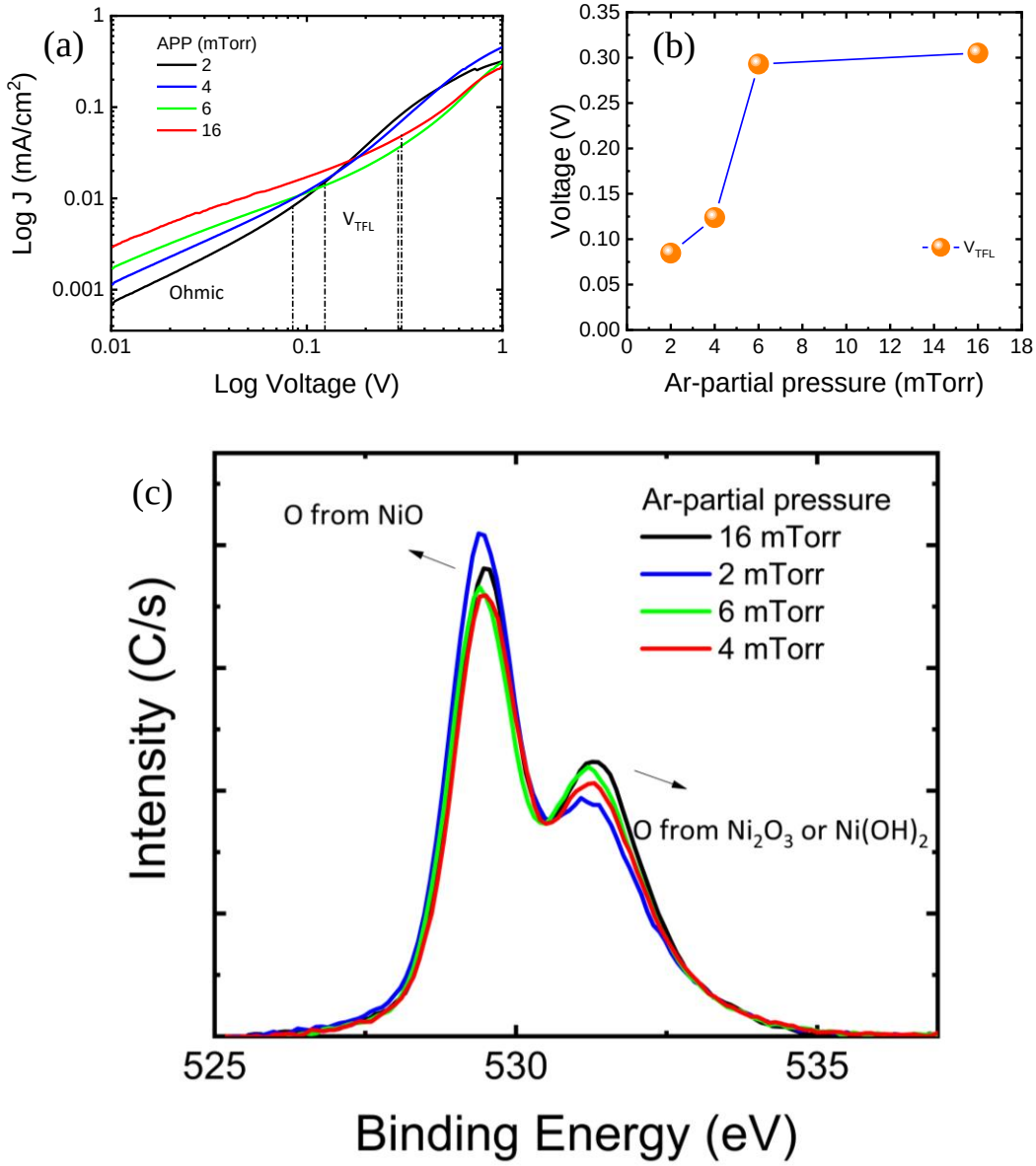

Figure 4-8 a) SCLC measurement for the hole-only device using NiO_X/ITO prepared under different APPs, b) V_{TFL} values derived from (a), c) XPS regional scan of the oxygen peak of the NiO_X/ITO samples in (a), d, e, f, g) all V_{OC}, J_{SC}, FF and PCE data for devices using NiO_X/ITO samples in (a).

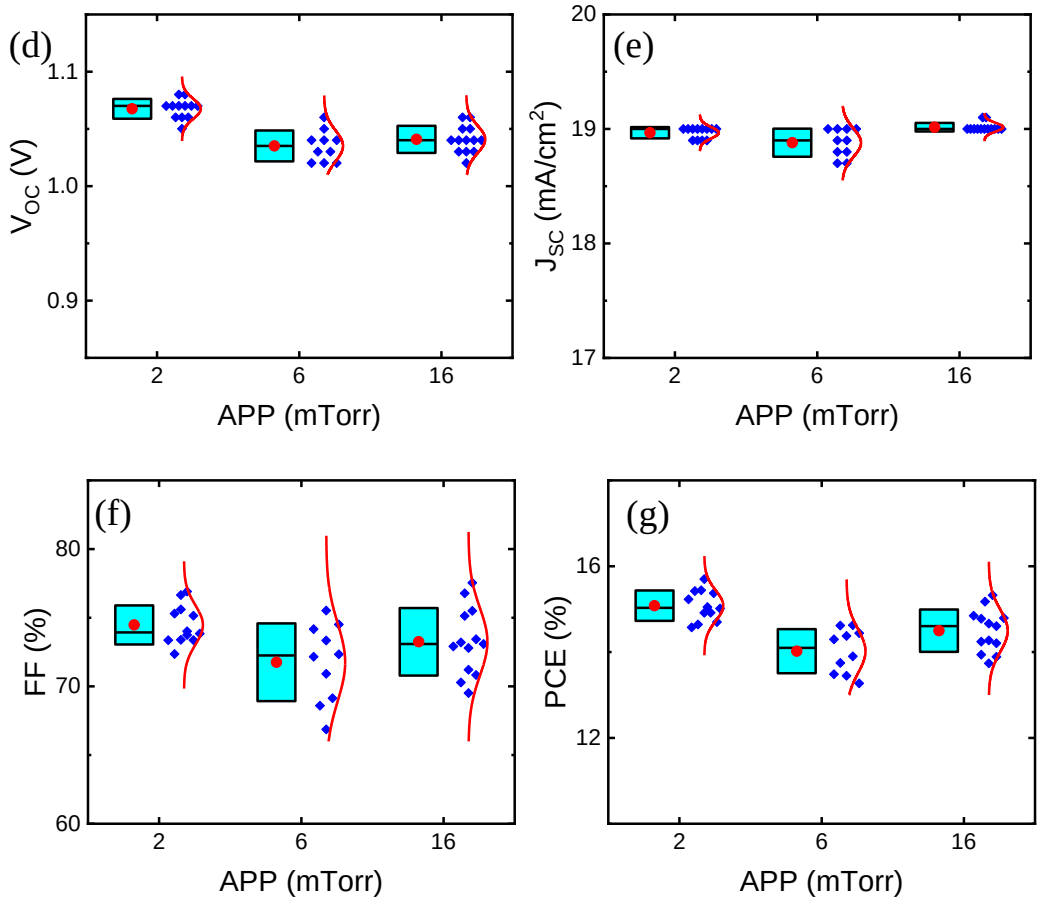

Figure 4-9 (continued).

Table 4-1 Average J-V characteristic values for perovskite solar cells fabricated using NiO_X deposited under 2 and 4 mTorr of APP.

APP (mTorr)	V_{OC} (V)	J_{SC} (mA/cm^2)	FF (%)	PCE (%)
2	1.024 ± 0.012	17.7 ± 0.2	65.3 ± 4.3	11.8 ± 0.9
4	1.039 ± 0.004	17.9 ± 0.3	69.9 ± 2.3	13.0 ± 0.5

4.2.4 Inorganic passivation of NiO_X

Aside from organic materials discussed in section 3.1, inorganic compounds have also been used to passivate NiO_X such as KCl, NaCl, CuI [21,101]. In this section, we

investigated the effect of in-situ deposition of a thin layer of SiO_2 and CuO atop 10 nm-thick NiO_X, on the performance of PSCs using J-V analysis. For this purpose, the thicknesses of SiO_2 and CuO were varied in the range of 0.5-1.5 nm and 0.5-2 nm respectively. Figure 4-10a-f shows the J-V and EQE results for the CuO/NiO_X. The average V_{OC} does not change considerably with CuO. 0.5 and 1 nm of CuO increases the average J_{SC} from 18.4 to 19.1 and 19.3 mA/cm^2, respectively. The average FF reaches a maximum (67.9) with 0.5 nm of CuO and drops with the thicker CuO layers which are due to the increased series resistance according to Figure 4-10e. Overall, due to an enhancement of J_{SC} and FF, the best average PCE (13.1 %) was achieved when CuO was 0.5 nm indicating a 1.5 % enhancement in average PCE compared to NiO_X without CuO on top.

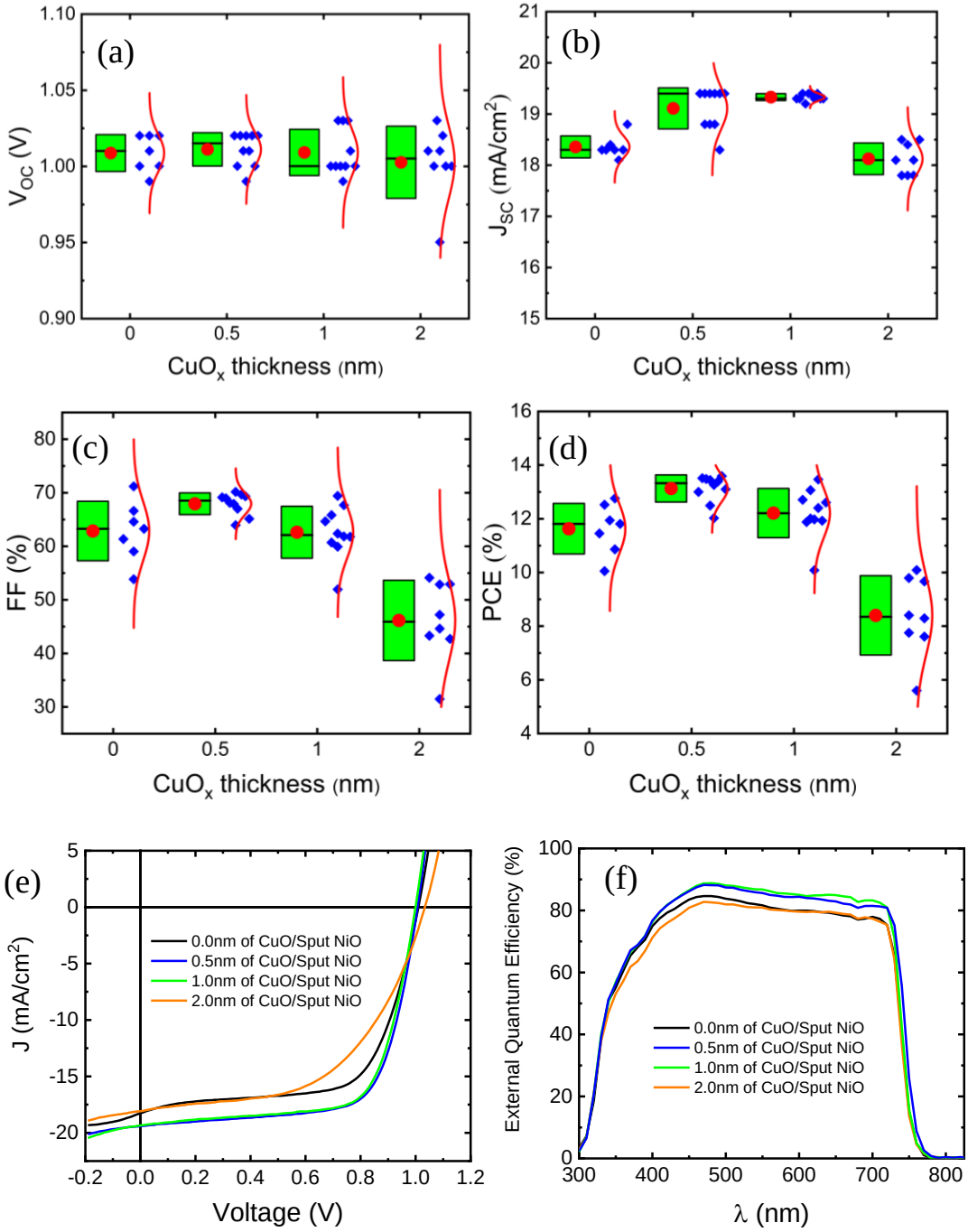

Figure 4-10 a, b, c, d) all V_{OC}, J_{SC}, FF and PCE data for devices using CuO_X coated NiO_X/ITO samples with different CuO_X thicknesses, e) J-V for the best cells in (a), f) EQE spectra for the samples in (a).

SiO_2 on top of NiO_X resulted in a drop in the average FF according to J-V characteristic results shown in Figure 4-11a-f. The FF dropped dramatically with

thicker SiO_2 layers. Therefore, SiO_2 was found unsuitable to passivate NiO_X to be used in PSCs

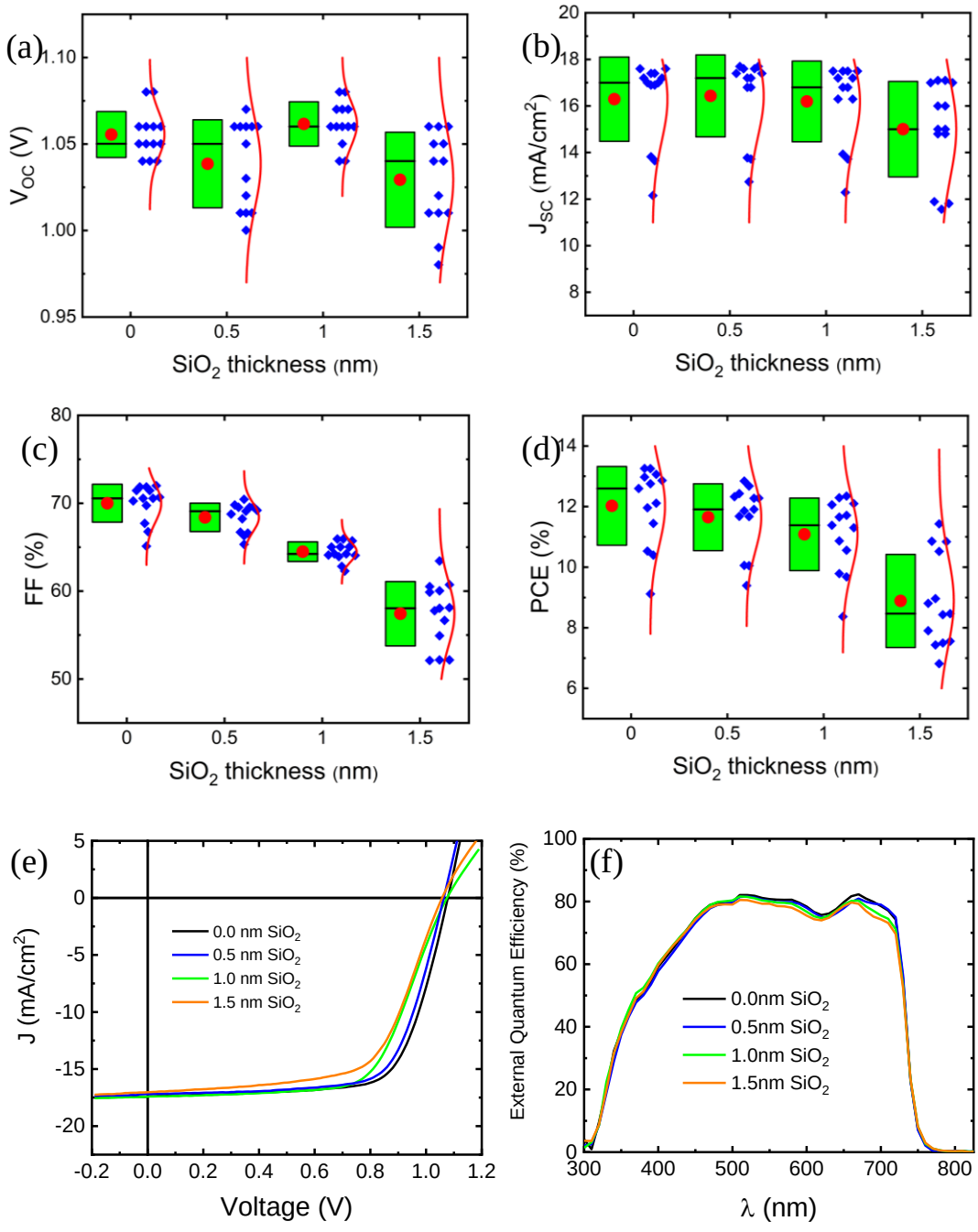

Figure 4-11 a, b, c, d) all V_{OC}, J_{SC}, FF and PCE data for devices using SiO_2 coated NiO_X/ITO samples with different SiO_2 thicknesses, e) J-V for the best cells in (a), f) EQE spectra for the samples in (a).

4.2.5 Doping NiO_X with Cu by co-sputtering

Another way to tune the work function and electrical properties of NiO_X is doping. NiO_X has been doped with various metals such as Ag, Co, Zn, Li, Cs, Mg, Cu, La, Y, Sr. Among all the dopants, Cu has been a favorite choice due to its facile integration in the NiO_X lattice and has rendered one of the highest PCE (20.3%)[81,87]. While many studies demonstrated mobility enhancement of Cu doped NiO_X (Cu:NiO_X) compared with intrinsic NiO_X, some other studies showed reduced mobilities[102]. Nevertheless, doping NiO_X with Cu, deepens its work function, increases its p-conductivity, promotes its charge carrier concentration, and even has improved the crystallinity of the upper MAPI layer[81,82,103,104]. Doping NiO_X during RF magnetron sputtering has not been employed in perovskite solar cells. Here, we doped NiO_X with Cu using a Cu target inside the sputtering chamber. The concentration of Cu was tuned using the rate ratios between Cu and NiO_X and was measured by XPS as shown in Figure 4-12a. Because of the high refractive index (~2.8 at λ = 632 nm) of Cu doped NiO_X (Cu:NiO_X), thicknesses above 20 nm is not optically efficient [96]. Therefore, in the first batch of solar cells, 5 nm-thick Cu:NiO_X were used to fabricate PSCs. The results are shown in Figure 4-12b-e.

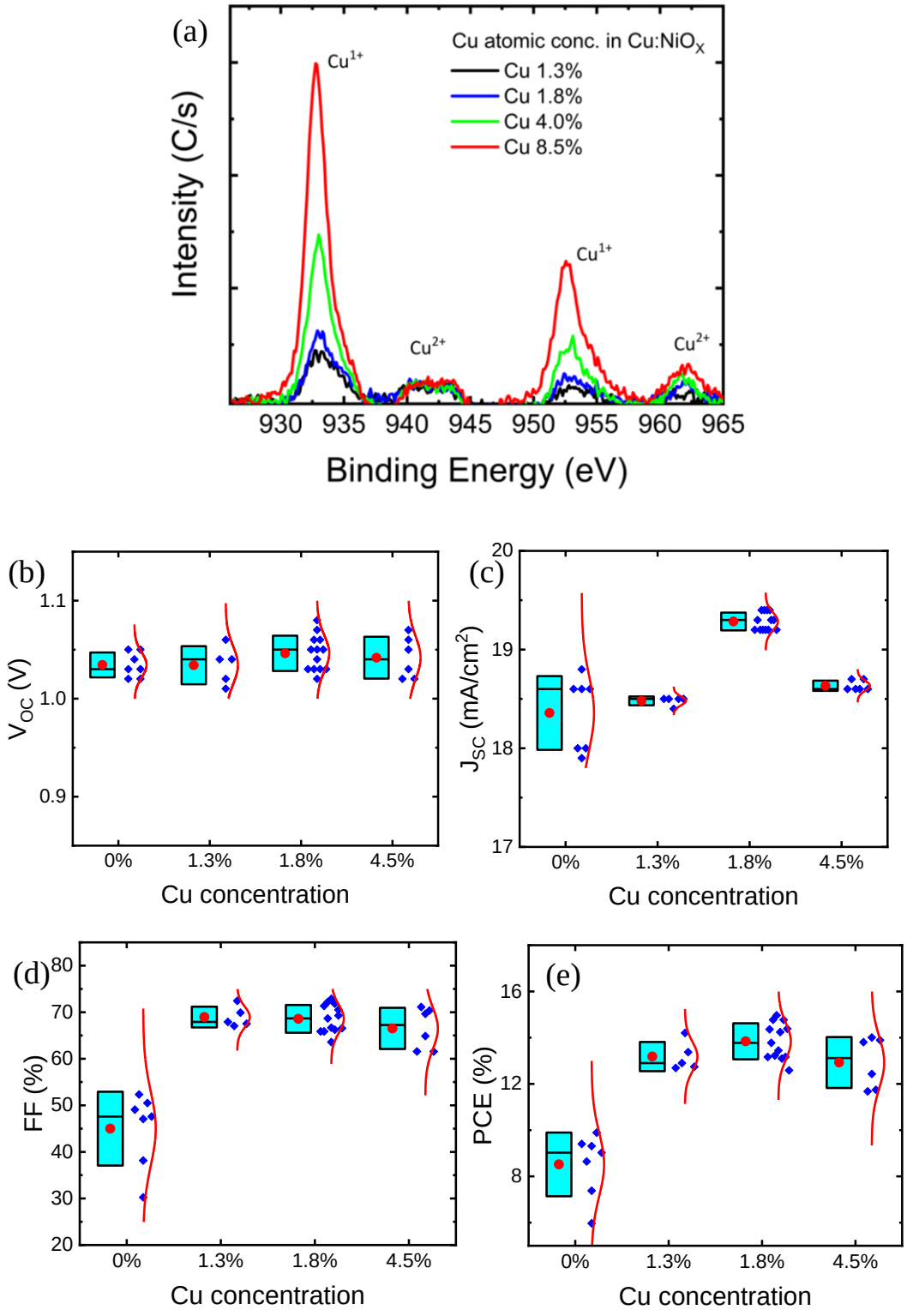

Figure 4-12 a) XPS local peak for Cu depending on the different concentrations of Cu in NiO_X/ITO, b, c, d, e) all V_{OC}, J_{SC}, FF and PCE data for devices using Cu:NiO_X in (a).

According to J-V characteristics in Figure 4-12, Cu doping increased the average J_{SC} and FF. The highest average J_{SC} (19.3 mA/cm^2) was demonstrated when the atomic concentration of Cu was 1.8%. Therefore, 1.8 atomic percent Cu was found as optimal with the highest average efficiencies (13.8%) as compared with the undoped and other Cu concentrations in Cu:NiO_X. However, the undoped NiO_X showed too low FF. Therefore, another experiment was designed with thicker Cu:NiO_X samples as shown in Figure 4-13. The average J_{SC} (19.0 mA/cm^2) and V_{OC} (1.050 V), increased (19.6/19.6 mA/cm^2) and (1.057/1.058 V) respectively when the thickness of Cu:NiO_X was reduced from 20 to 15 or 10 nm. Overall, the highest average PCE (15.0 %) was achieved with a thickness of 10 nm as compared with 20 nm (14.5 %) and 15 nm (14.9 %). Therefore, a thickness range of 10-15 nm is optimal for Cu:NiO_X as HTL in PSCs.

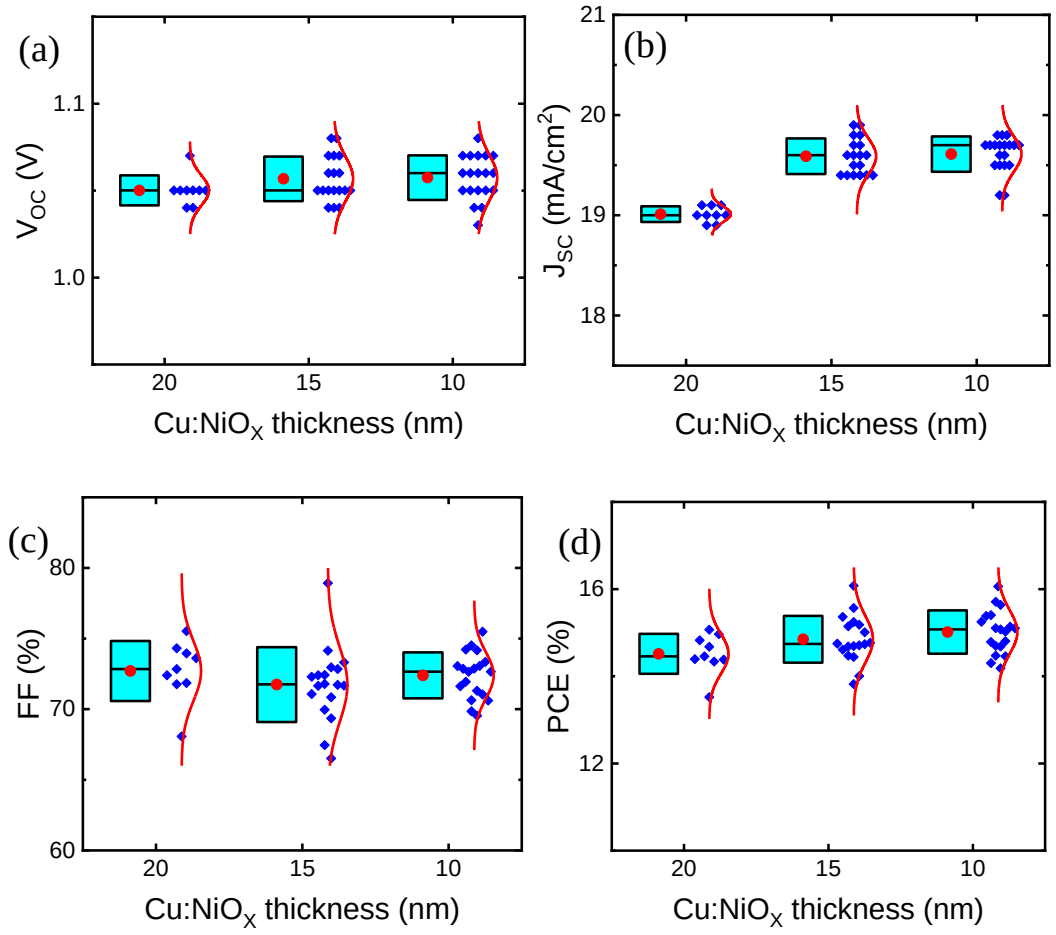

Figure 4-13 a, b, c, d) all V_{OC}, J_{SC}, FF and PCE data for devices using different thicknesses of Cu:NiO_X/ITO samples.

As another direct comparison between the performances of undoped NiO_X and Cu:NiO_X, another batch of cells was fabricated using 10 nm-thick NiO_X and Cu:NiO_X with the J-V data shown in Figure 4-14. The average J-V parameters were enhanced unanimously when doping NiO_X by 1.8% Cu. The improvement is considerable in the average J_{SC} which boosted from 17.5 in the case of NiO_X to 19.1 mA/cm^2 with Cu:NiO_X. The overall average PCE increased from 12.8 to 14.9 % following doping NiO_X. According to Figure 4-14 and Table 4-2, the devices worked with minimal hysteresis. A higher efficiency was achieved with Cu:NiO_X (16.3%) as compared with NiO_X with the best PCE of 13.3%.

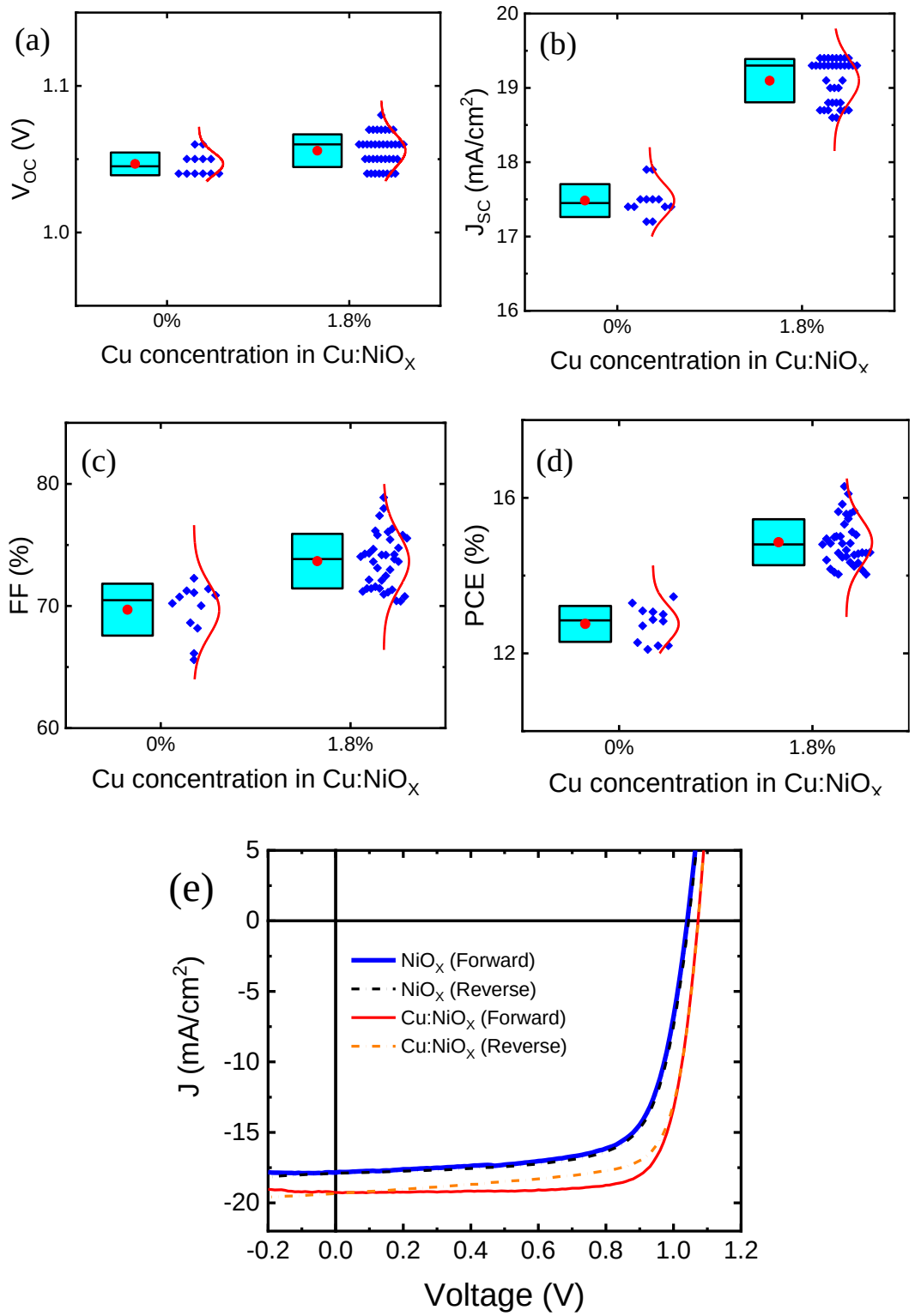

Figure 4-14 a, b, c, d) all V_{OC}, J_{SC}, FF and PCE data for devices using NiO_X/ITO and Cu:NiO_X/ITO with 1.8% of Cu, e) Forward and reverse J-V for the best cells in (a).

Table 4-2 Forward and reverse J-V data for the best cells presented in Figure 4-14e.

Best cells	V_{OC} (V)	J_{SC} (mA/cm^2)	FF (%)	PCE (%)
NiO_X	1.040	17.9	71.4	13.3
(reverse)	(1.040)	(17.9)	(72.3)	(13.5)
Cu:NiO_X	1.070	19.3	78.9	16.3
(reverse)	(1070)	(19.3)	(78.0)	(16.1)

4.3 Conclusions

In this chapter, we studied the effects of the sputtering rate and Argon partial pressure on the optoelectronic properties of sputtered NiO_X in full perovskite-based photovoltaic devices. The optical properties of NiO_X were elucidated considering the stack of NiO_X based stack of the solar cell. We propose the same discretion to study any film in optoelectronic devices. According to our studies, depositing NiO_X under APP of 4 mTorr resulted in the best solar cell performance. To understand, the interfacial properties of NiO_X UPS measurements are necessary. While annealing NiO_X improved the FF, coating NiO_X with Poly-TPD improved V_{OC} and J_{SC} of the devices. The deposition of 0.5 nm thick CuO_X on top of NiO_X enhanced the efficiency of the solar cells by improving the J_{SC} and FF of the devices. Coating NiO_X with SiO_2 resulted in the deterioration of FF and J_{SC} and therefore poor efficiencies. Doping NiO_X with 1.8 At% Cu by RF magnetron sputtering enhanced all the J-V characteristics especially 2.6% efficiency rise of the resultant perovskite solar cells.

CHAPTER 5

CONCLUSIONS AND OUTLOOKS

In this thesis, the industrially feasible techniques were employed to fabricate and optimize multi-layer perovskite solar cells. The co-evaporation of organic MAI and inorganic $PbCl_2$ was conducted in a high-vacuum chamber. While the deposition rate of $PbCl_2$ was monitored by a QCM, the deposition rate of MAI was shown to follow its vapor pressure inside the chamber. The crystallinity of MAPI-Cl perovskite was tracked optimizing MAI vapor pressure (5×10^{-5} Torr) while the $PbCl_2$ deposition rate was kept constant at 0.3 Å/s. The post-annealing of the samples at 100 °C further enhanced the crystallinity of the perovskite films. The solution deposition of TiO_2 was optimized in terms of the employed precursor and the $TiCl_4$ treatment. Also, the two-step precursor spin-casting was engineered to achieve the highest FF and J_{SC} of the resultant perovskite solar cells. The co-evaporated perovskite was successfully employed in both n-i-p and p-i-n structures. FTO/TiO_2/MAPI-Cl/Spiro-OMeTAD/Ag was used as the n-i-p structure yielding solar cells with 13.0% efficiency. The p-i-n structure is more attractive to use due to its low-temperature processing. All the constituent transport layers and the absorber layer were fabricated through vacuum-deposition resulting in conformal layer coverage over the entire area of the substrates. Therefore, this structure qualifies as integrable into scalable production with light-weight flexible substrates. The presented p-i-n stack can be adopted in tandem with the thin-film PV technologies such as a-Si or CIGS. In this work, ITO/NiO_X/MAPI-Cl/C_{60}/BCP/Ag was used as the p-i-n configuration optimizing the thickness of C_{60} to yield high efficiencies of 16.1%. When larger active areas of 1.00 cm^2 and 2.03 cm^2 were used, the devices worked with efficiencies of 6.0 % and 5.5 %, respectively. We attribute the drop in the efficiency with the larger area to arise from the increased series resistance of the bottom TCO and the nonreproducibility issues. To avoid the resistance issue, one future work can

be using perovskite solar cells in the form of a module [105]. To tackle the problem with the reproducibility, the mounting unit of the chamber used for perovskite by co-evaporation must be placed in an inert atmosphere such as N_2 or Ar isolated from the air [22,23,106].

The hybrid vapor-solution sequential method was upgraded in this thesis. The crystallization of the inorganic PbI_2 layer depends strongly on the bottom substrate forming porous morphology on crystalline substrates such as TiO_2 facilitating the interdiffusion process during the two-step method. However, when an organic layer is used as the substrate, the PbI_2 film takes a compact form limiting the thickness of the converted PbI_2 layer into perovskite. We used MABr and MACl as additives to overcome such conversion barriers making 460 nm thick perovskite layers using this method for the first time. Halide-mixing also improved the crystallization of the perovskite layer and the operational stability of the resultant devices. The ratios of MABr/MAI was successfully engineered to minimize the cell performance gap between the measured values and the Shockley-Quiesser limit corresponding to the bandgap of the perovskite layer. The optimized devices demonstrated 19.8% efficiency with 90 hours of stable performance. The method presented here benefits from the uniform coating of vacuum deposition making it industry-friendly. Furthermore, the solution step provided control over halide mixing which may not be as straightforward in vapor deposition. The spin-coating can be promoted into more versatile solution processes such as dip-coating or slot-die coating. Therefore, the hybrid vapor-solution sequential is a methodology expandible to roll-to-roll PV technologies. As a future study, mixed cation perovskites including Cs^+ and FA^+ can be realized using this methodology to elevate the stability of the devices facilitating the introduction of these solar cells into the market. In this concept, CsI and FAI can be dissolved in the halide solution. Alternatively, CsI can be co-evaporated with PbI_2 or $PbBr_2$ followed by a solution treatment containing FAI.

The scalability of the p-i-n perovskite solar cells was further triggered by focusing on the HTL. For one thing, a proven stable HTL namely NiO was chosen. Second, RF magnetron sputtering was employed as a popular technology in the industry to

deposit NiO_X thin films. In this regard, the Ar partial pressure (APP) was found to be the key parameter during the sputtering to define the crystallinity and optoelectronic properties of NiO_X. The refractive indices of NiO_X were investigated versus the APP providing a subtle insight into the optical properties of NiO_X. We proved that there is a trade-off between the parasitic and reflection losses to define the optical transmission of NiO_X leading to high photocurrents. Our results pinpoint the urge to study the optical properties of any thin film according to its adjacent media. The electronic trap density increased with the APP. We devised full perovskite solar cells proving low APP of 4 mTorr as optimal to fabricate NiO_X layers. The interfacial properties of NiO_X improved with annealing as the FF of the solar cells got enhanced. Besides, we showed for the first time that applying poly-TPD as an interlayer between the NiO_X and perovskite layers enhanced the V_{OC} and considerably improved the FF and charge collection efficiency of the final solar cells. We showed that while sputtered SiO_2 as an inorganic interlayer, degraded the FF and J_{SC}, 0.5 nm-thick CuO_X boosted the FF and J_{SC} of the employed solar cells. Doping NiO_X by Cu via co-sputtering was successfully attempted here to be used in perovskite solar cells. According to our results, 1.8 atomic percentage of Cu within the NiO_X improved the efficiency of the perovskite solar cells from 13.3 % to 16.3%. In sum, sputtering was demonstrated as a strong tool to effectively tune the crystal, optical, electrical, and interfacial properties of transport layers. The electrical properties of a film can also be upgraded by precise doping via co-sputtering. These results give a strong momentum to bring the perovskite solar cells closer to industrialization. We propose that these findings are universal and the optimized NiO_X layers can be used in Si cells with dopant-free asymmetric heterocontacts (DASH cells). As a future study, doping NiO_X with other elements such as Al, Zn, and W using co-sputtering can be explored to further improve the electrical conductivity and work-function of NiO_X. Also, sputtering alternative inorganic materials to in-situ passivate NiO_X before use is an interesting and potentially useful way out to upgrade the use of NiO_X as an efficient hole transport layer in heterojunction solar cells.

REFERENCES

1. World Population by Year - Worldometer. https://www.worldometers.info/world-population/world-population-by-year/. Accessed February 2, 2020.
2. Global Energy & CO_2 Status Report 2019 – Analysis - IEA. https://www.iea.org/reports/global-energy-and-co2-status-report-2019. Accessed February 2, 2020.
3. Global Temperature | Vital Signs – Climate Change: Vital Signs of the Planet. https://climate.nasa.gov/vital-signs/global-temperature/. Accessed February 2, 2020.
4. Righini GC, Enrichi F. Solar cells' evolution and perspectives: a short review. In: *Solar Cells and Light Management*. Elsevier; 2020:1-32. doi:10.1016/b978-0-08-102762-2.00001-x
5. Kojima A, Teshima K, Shirai Y, Miyasaka T. Organometal halide perovskites as visible-light sensitizers for photovoltaic cells. *J Am Chem Soc*. 2009;131(17):6050-6051. doi:10.1021/ja809598r
6. Comin R, Walters G, Thibau ES, Voznyy O, Lu ZH, Sargent EH. Structural, optical, and electronic studies of wide-bandgap lead halide perovskites. *J Mater Chem C*. 2015;3(34):8839-8843. doi:10.1039/c5tc01718a
7. Correa-Baena J-P, Anaya M, Lozano G, et al. Unbroken Perovskite: Interplay of Morphology, Electro-optical Properties, and Ionic Movement. *Adv Mater*. 2016;28(25):5031-5037. doi:10.1002/adma.201600624
8. Hirasawa M, Ishihara T, Goto T, Uchida K, Miura N. Magnetoabsorption of the lowest exciton in perovskite-type compound (CH3NH3)PbI3. *Phys B Phys Condens Matter*. 1994;201(C):427-430. doi:10.1016/0921-4526(94)91130-4
9. Stranks SD, Eperon GE, Grancini G, et al. Electron-hole diffusion lengths exceeding 1 micrometer in an organometal trihalide perovskite absorber. *Science (80-)*. 2013;342(6156):341-344. doi:10.1126/science.1243982
10. Lee MM, Teuscher J, Miyasaka T, Murakami TN, Snaith HJ. Efficient hybrid solar cells based on meso-superstructured organometal halide perovskites. *Science (80-)*. 2012;338(6107):643-647. doi:10.1126/science.1228604
11. Lin Q, Armin A, Nagiri RCR, Burn PL, Meredith P. Electro-optics of perovskite solar cells. *Nat Photonics*. 2015;9(2):106-112. doi:10.1038/nphoton.2014.284
12. Song Z, McElvany CL, Phillips AB, et al. A technoeconomic analysis of perovskite solar module manufacturing with low-cost materials and

techniques. *Energy Environ Sci*. 2017;10(6):1297-1305. doi:10.1039/c7ee00757d

13. Momblona C, Gil-Escrig L, Bandiello E, et al. Efficient vacuum deposited p-i-n and n-i-p perovskite solar cells employing doped charge transport layers. *Energy Environ Sci*. 2016;9(11):3456-3463. doi:10.1039/c6ee02100j

14. Fu F, Kranz L, Yoon S, et al. Controlled growth of PbI_2 nanoplates for rapid preparation of $CH_3NH_3PbI_3$ in planar perovskite solar cells. *Phys Status Solidi Appl Mater Sci*. 2015;212(12):2708-2717. doi:10.1002/pssa.201532442

15. Grancini G, Roldán-Carmona C, Zimmermann I, et al. One-Year stable perovskite solar cells by 2D/3D interface engineering. *Nat Commun*. 2017;8. doi:10.1038/ncomms15684

16. Jung MC, Raga SR, Ono LK, Qi Y. Substantial improvement of perovskite solar cells stability by pinhole-free hole transport layer with doping engineering. *Sci Rep*. 2015;5(1):1-5. doi:10.1038/srep09863

17. You J, Meng L, Song T Bin, et al. Improved air stability of perovskite solar cells via solution-processed metal oxide transport layers. *Nat Nanotechnol*. 2016;11(1):75-81. doi:10.1038/nnano.2015.230

18. Cao J, Wu B, Chen R, et al. Efficient, Hysteresis-Free, and Stable Perovskite Solar Cells with ZnO as Electron-Transport Layer: Effect of Surface Passivation. *Adv Mater*. 2018;30(11):1705596. doi:10.1002/adma.201705596

19. Cheng H, Li Y, Zhao G, Zhao K, Wang Z-S. Pyridine-Terminated Conjugated Organic Molecules as an Interfacial Hole Transfer Bridge for NiO_x-Based Perovskite Solar Cells. *ACS Appl Mater Interfaces*. 2019;11(32):28960-28967. doi:10.1021/acsami.9b09530

20. Du Y, Xin C, Huang W, et al. Polymeric Surface Modification of NiO_x-Based Inverted Planar Perovskite Solar Cells with Enhanced Performance. *ACS Sustain Chem Eng*. 2018;6(12):16806-16812. doi:10.1021/acssuschemeng.8b04078

21. Saranin D, Gostischev P, Tatarinov D, et al. Copper Iodide Interlayer for Improved Charge Extraction and Stability of Inverted Perovskite Solar Cells. *Materials (Basel)*. 2019;12(9):1406. doi:10.3390/ma12091406

22. Liu M, Johnston MB, Snaith HJ. Efficient planar heterojunction perovskite solar cells by vapour deposition. *Nature*. 2013;501(7467):395-398. doi:10.1038/nature12509

23. Babaei A, Soltanpoor W, Tesa-Serrate MA, Yerci S, Sessolo M, Bolink HJ. Preparation and Characterization of Mixed Halide $MAPbI_{3-x}Cl_x$ Perovskite Thin Films by Three-Source Vacuum Deposition. *Energy Technol*. September 2019:1900784. doi:10.1002/ente.201900784

24. Ono LK, Wang S, Kato Y, Raga SR, Qi Y. Fabrication of semi-transparent perovskite films with centimeter-scale superior uniformity by the hybrid deposition method. *Energy Environ Sci*. 2014;7(12):3989-3993. doi:10.1039/c4ee02539c

25. Wang S, Ono LK, Leyden MR, et al. Smooth perovskite thin films and efficient perovskite solar cells prepared by the hybrid deposition method. *J Mater Chem A*. 2015;3(28):14631-14641. doi:10.1039/c5ta03593g

26. Jacobsson TJ, Schwan LJ, Ottosson M, Hagfeldt A, Edvinsson T. Determination of Thermal Expansion Coefficients and Locating the Temperature-Induced Phase Transition in Methylammonium Lead Perovskites Using X-ray Diffraction. *Inorg Chem*. 2015;54(22):10678-10685. doi:10.1021/acs.inorgchem.5b01481

27. Wang Y, Li L, Huang X, Li Q, Li G. New insights into fluorinated TiO2 (brookite, anatase and rutile) nanoparticles as efficient photocatalytic redox catalysts. *RSC Adv*. 2015;5(43):34302-34313. doi:10.1039/c4ra17076h

28. Xu Y, Gao C, Tang S, et al. Comprehensive understanding of $TiCl_4$ treatment on the compact TiO_2 layer in planar perovskite solar cells with efficiencies over 20%. *J Alloys Compd*. 2019;787:1082-1088. doi:10.1016/j.jallcom.2019.02.027

29. Adli HK, Harada T, Nakanishi S, Ikeda S. Effects of $TiCl_4$ treatment on the structural and electrochemical properties of a porous TiO_2 layer in $CH_3NH_3PbI_3$ perovskite solar cells. *Phys Chem Chem Phys*. 2017;19(39):26898-26905. doi:10.1039/c7cp04132b

30. Nia NY, Matteocci F, Cina L, Di Carlo A. High-Efficiency Perovskite Solar Cell Based on Poly(3-Hexylthiophene): Influence of Molecular Weight and Mesoscopic Scaffold Layer. *ChemSusChem*. 2017;10(19):3854-3860. doi:10.1002/cssc.201700635

31. Way A, Luke J, Evans AD, et al. Fluorine doped tin oxide as an alternative of indium tin oxide for bottom electrode of semi-transparent organic photovoltaic devices ARTICLES YOU MAY BE INTERESTED IN. 2019. doi:10.1063/1.5104333

32. Islam MB, Yanagida M, Shirai Y, Nabetani Y, Miyano K. NiOx Hole Transport Layer for Perovskite Solar Cells with Improved Stability and Reproducibility. *ACS Omega*. 2017;2(5):2291-2299. doi:10.1021/acsomega.7b00538

33. Vogel M, Doka S, Breyer C, Ch Lux-Steiner M, Fostiropoulos K. Cite as. *Appl Phys Lett*. 2006;89:163501. doi:10.1063/1.2362624

34. Bartynski AN, Trinh C, Panda A, et al. A Fullerene-Based Organic Exciton Blocking Layer with High Electron Conductivity. *Nano Lett*.

2013;13(7):3315-3320. doi:10.1021/nl401531t

35. Liu D, Wang Q, Traverse CJ, et al. Impact of Ultrathin C_{60} on Perovskite Photovoltaic Devices. *ACS Nano*. 2018;12(1):876-883. doi:10.1021/acsnano.7b08561

36. Zanoni KPS, Pérez-del-Rey D, Dreessen C, et al. Use of Hydrogen Molybdenum Bronze in Vacuum-Deposited Perovskite Solar Cells. *Energy Technol*. September 2019:1900734. doi:10.1002/ente.201900734

37. Green MA, Dunlop ED, Levi DH, Hohl-Ebinger J, Yoshita M, Ho-Baillie AWY. Solar cell efficiency tables (version 54). *Prog Photovoltaics Res Appl*. 2019;27(7):565-575. doi:10.1002/pip.3171

38. Noh JH, Im SH, Heo JH, Mandal TN, Seok S Il. Chemical management for colorful, efficient, and stable inorganic-organic hybrid nanostructured solar cells. *Nano Lett*. 2013;13(4):1764-1769. doi:10.1021/nl400349b

39. Smith MD, Connor BA, Karunadasa HI. Tuning the Luminescence of Layered Halide Perovskites. *Chem Rev*. 2019;119(5):3104-3139. doi:10.1021/acs.chemrev.8b00477

40. Miyata A, Mitioglu A, Plochocka P, et al. Direct measurement of the exciton binding energy and effective masses for charge carriers in organic-inorganic tri-halide perovskites. *Nat Phys*. 2015;11(7):582-587. doi:10.1038/nphys3357

41. Lee J-W, Kim D-H, Kim H-S, Seo S-W, Cho SM, Park N-G. Formamidinium and Cesium Hybridization for Photo- and Moisture-Stable Perovskite Solar Cell. *Adv Energy Mater*. 2015;5(20):1501310. doi:10.1002/aenm.201501310

42. Saliba M, Matsui T, Seo JY, et al. Cesium-containing triple cation perovskite solar cells: Improved stability, reproducibility and high efficiency. *Energy Environ Sci*. 2016;9(6):1989-1997. doi:10.1039/c5ee03874j

43. Yi C, Luo J, Meloni S, et al. Entropic stabilization of mixed A-cation ABX_3 metal halide perovskites for high performance perovskite solar cells. *Energy Environ Sci*. 2016;9(2):656-662. doi:10.1039/c5ee03255e

44. Rehman W, McMeekin DP, Patel JB, et al. Photovoltaic mixed-cation lead mixed-halide perovskites: Links between crystallinity, photo-stability and electronic properties. *Energy Environ Sci*. 2017;10(1):361-369. doi:10.1039/c6ee03014a

45. Swarnkar A, Mir WJ, Nag A. Can B-Site Doping or Alloying Improve Thermal- and Phase-Stability of All-Inorganic $CsPbX_3$ (X = Cl, Br, I) Perovskites? *ACS Energy Lett*. 2018;3(2):286-289. doi:10.1021/acsenergylett.7b01197

46. Xiao M, Huang F, Huang W, et al. A Fast Deposition-Crystallization Procedure for Highly Efficient Lead Iodide Perovskite Thin-Film Solar Cells.

Angew Chemie Int Ed. 2014;53(37):9898-9903. doi:10.1002/anie.201405334

47. Li Z, Klein TR, Kim DH, et al. Scalable fabrication of perovskite solar cells. *Nat Rev Mater*. 2018;3. doi:10.1038/natrevmats.2018.17

48. Im JH, Jang IH, Pellet N, Grätzel M, Park NG. Growth of $CH_3NH_3PbI_3$ cuboids with controlled size for high-efficiency perovskite solar cells. *Nat Nanotechnol*. 2014;9(11):927-932. doi:10.1038/nnano.2014.181

49. Yantara N, Sabba D, Yanan F, et al. Loading of mesoporous titania films by $CH_3NH_3PbI_3$ perovskite, single step vs. sequential deposition. *Chem Commun*. 2015;51(22):4603-4606. doi:10.1039/C4CC09556A

50. Pérez-del-Rey D, Boix PP, Sessolo M, Hadipour A, Bolink HJ. Interfacial Modification for High-Efficiency Vapor-Phase-Deposited Perovskite Solar Cells Based on a Metal Oxide Buffer Layer. *J Phys Chem Lett*. 2018;9(5):1041-1046. doi:10.1021/acs.jpclett.7b03361

51. Hsiao S-Y, Lin H-L, Lee W-H, et al. Efficient All-Vacuum Deposited Perovskite Solar Cells by Controlling Reagent Partial Pressure in High Vacuum. *Adv Mater*. 2016;28(32):7013-7019. doi:10.1002/adma.201601505

52. Chen C-W, Kang H-W, Hsiao S-Y, Yang P-F, Chiang K-M, Lin H-W. Efficient and Uniform Planar-Type Perovskite Solar Cells by Simple Sequential Vacuum Deposition. *Adv Mater*. 2014;26(38):6647-6652. doi:10.1002/adma.201402461

53. Duan J, Liu Z, Zhang Y, et al. Planar perovskite $FA_xMA_{1-x}PbI_3$ solar cell by two-step deposition method in air ambient. *Opt Mater (Amst)*. 2018;85:55-60. doi:10.1016/j.optmat.2018.07.072

54. Bing J, Kim J, Zhang M, et al. The Impact of a Dynamic Two-Step Solution Process on Film Formation of $Cs_{0.15}(MA_{0.7}FA_{0.3})_{0.85}PbI_3$ Perovskite and Solar Cell Performance. *Small*. 2019;15(9):1804858. doi:10.1002/smll.201804858

55. Hwang K, Jung Y-S, Heo Y-J, et al. Toward Large Scale Roll-to-Roll Production of Fully Printed Perovskite Solar Cells. *Adv Mater*. 2015;27(7):1241-1247. doi:10.1002/adma.201404598

56. Huang H, Shi J, Zhu L, Li D, Luo Y, Meng Q. Two-step ultrasonic spray deposition of CH3NH3PbI3 for efficient and large-area perovskite solar cell. *Nano Energy*. 2016;27:352-358. doi:10.1016/j.nanoen.2016.07.026

57. Rafizadeh S, Wienands K, Schulze PSC, et al. Efficiency Enhancement and Hysteresis Mitigation by Manipulation of Grain Growth Conditions in Hybrid Evaporated−Spin-coated Perovskite Solar Cells. 2018. doi:10.1021/acsami.8b16963

58. Unger EL, Hoke ET, Bailie CD, et al. Hysteresis and transient behavior in current-voltage measurements of hybrid-perovskite absorber solar cells.

Energy Environ Sci. 2014;7(11):3690-3698. doi:10.1039/c4ee02465f

59. Yang D, Zhou X, Yang R, et al. Surface optimization to eliminate hysteresis for record efficiency planar perovskite solar cells. *Energy Environ Sci*. 2016;9(10):3071-3078. doi:10.1039/c6ee02139e

60. Byranvand MM, Kim T, Song S, Kang G, Ryu SU, Park T. p-Type CuI Islands on TiO_2 Electron Transport Layer for a Highly Efficient Planar-Perovskite Solar Cell with Negligible Hysteresis. *Adv Energy Mater*. 2018;8(5):1702235. doi:10.1002/aenm.201702235

61. Li Y, Zhao Y, Chen Q, et al. Multifunctional Fullerene Derivative for Interface Engineering in Perovskite Solar Cells. *J Am Chem Soc*. 2015;137(49):15540-15547. doi:10.1021/jacs.5b10614

62. Sidhik S, Panikar SS, Pérez CR, et al. Interfacial Engineering of TiO_2 by Graphene Nanoplatelets for High-Efficiency Hysteresis-free Perovskite Solar Cells. *ACS Sustain Chem Eng*. 2018;6(11):15391-15401. doi:10.1021/acssuschemeng.8b03826

63. Luo J, Wan Z, Han F, et al. Origin of increased efficiency and decreased hysteresis of perovskite solar cells by using 4-tert-butyl pyridine as interfacial modifier for TiO_2. *J Power Sources*. 2019;415:197-206. doi:10.1016/j.jpowsour.2019.01.064

64. Sun Z, Huang W, Ma H, Lv Y, Wang J, Zhang H. Influence of Cl Incorporation in Perovskite Precursor on the Crystal Growth and Storage Stability of Perovskite Solar Cells. *ACS Appl Mater Interfaces*. 2019. doi:10.1021/acsami.8b19390

65. Jiang Q, Chu Z, Wang P, et al. Planar-Structure Perovskite Solar Cells with Efficiency beyond 21%. *Adv Mater*. 2017;29(46):1-7. doi:10.1002/adma.201703852

66. Song L, Wang W, Körstgens V, et al. In situ study of spray deposited titania photoanodes for scalable fabrication of solid-state dye-sensitized solar cells. *Nano Energy*. 2017;40:317-326. doi:10.1016/J.NANOEN.2017.08.023

67. Ummadisingu A, Grätzel M. Revealing the detailed path of sequential deposition for metal halide perovskite formation. *Sci Adv*. 2018;4(2):e1701402. doi:10.1126/sciadv.1701402

68. Tripathi N, Yanagida M, Shirai Y, Miyano K. Improved performance of planar perovskite devices via inclusion of ammonium acid iodide (AAI) derivatives using a two step inter-diffusion process. *J Mater Chem C*. 2019;7(12):3447-3451. doi:10.1039/c8tc05328f

69. Li M, Yan X, Kang Z, et al. Enhanced Efficiency and Stability of Perovskite Solar Cells via Anti-Solvent Treatment in Two-Step Deposition Method. 2017. doi:10.1021/acsami.7b01136

70. Chen H, Wei Z, He H, Zheng X, Wong KS, Yang S. Solvent Engineering Boosts the Efficiency of Paintable Carbon-Based Perovskite Solar Cells to Beyond 14%. *Adv Energy Mater*. 2016;6(8):1502087. doi:10.1002/aenm.201502087

71. Dong Q, Yuan Y, Shao Y, Fang Y, Wang Q, Huang J. Abnormal crystal growth in $CH_3NH_3PbI_{3-x}Cl_x$ using a multi-cycle solution coating process. *Energy Environ Sci*. 2015;8(8):2464-2470. doi:10.1039/C5EE01179E

72. Burschka J, Pellet N, Moon SJ, et al. Sequential deposition as a route to high-performance perovskite-sensitized solar cells. *Nature*. 2013;499(7458):316-319. doi:10.1038/nature12340

73. Yang L, Barrows AT, Lidzey DG. PbI 2 platelets for inverted planar organolead Halide Perovskite solar cells via ultrasonic spray deposition Related content Recent progress and challenges of organometal halide perovskite solar cells. 2017. doi:10.1088/1361-6641/aa6e47

74. Xie F, Chen CC, Wu Y, et al. Vertical recrystallization for highly efficient and stable formamidinium-based inverted-structure perovskite solar cells. *Energy Environ Sci*. 2017;10(9):1942-1949. doi:10.1039/c7ee01675a

75. Zhang T, Guo N, Li G, Qian X, Zhao Y. A controllable fabrication of grain boundary PbI2 nanoplates passivated lead halide perovskites for high performance solar cells. *Nano Energy*. 2016;26:50-56. doi:10.1016/J.NANOEN.2016.05.003

76. Liu D, Gangishetty MK, Kelly TL. Effect of $CH_3NH_3PbI_3$ thickness on device efficiency in planar heterojunction perovskite solar cells. *J Mater Chem A*. 2014;2(46):19873-19881. doi:10.1039/C4TA02637C

77. Chen Q, Zhou H, Fang Y, et al. The optoelectronic role of chlorine in CH3NH3PbI3 (Cl)-based perovskite solar cells. *Nat Commun*. 2015;6. doi:10.1038/ncomms8269

78. Ono LK, Juarez-Perez EJ, Qi Y. Progress on Perovskite Materials and Solar Cells with Mixed Cations and Halide Anions. *ACS Appl Mater Interfaces*. 2017;9(36):30197-30246. doi:10.1021/acsami.7b06001

79. Yoon SJ, Stamplecoskie KG, Kamat P V. How Lead Halide Complex Chemistry Dictates the Composition of Mixed Halide Perovskites. *J Phys Chem Lett*. 2016;7(7):1368-1373. doi:10.1021/acs.jpclett.6b00433

80. Xu L, Chen X, Jin J, et al. Inverted perovskite solar cells employing doped NiO hole transport layers: A review. *Nano Energy*. 2019;63. doi:10.1016/j.nanoen.2019.103860

81. Kim JH, Liang P-W, Williams ST, et al. High-Performance and Environmentally Stable Planar Heterojunction Perovskite Solar Cells Based on a Solution-Processed Copper-Doped Nickel Oxide Hole-Transporting

Layer. *Adv Mater*. 2015;27(4):695-701. doi:10.1002/adma.201404189

82. Liu A, Zhu H, Guo Z, et al. Solution Combustion Synthesis: Low-Temperature Processing for p-Type Cu:NiO Thin Films for Transparent Electronics. *Adv Mater*. 2017;29(34):1701599. doi:10.1002/adma.201701599

83. Seo S, Park IJ, Kim M, et al. An ultra-thin, un-doped NiO hole transporting layer of highly efficient (16.4%) organic-inorganic hybrid perovskite solar cells. *Nanoscale*. 2016;8(22):11403-11412. doi:10.1039/c6nr01601d

84. Park JH, Seo J, Park S, et al. Efficient $CH_3NH_3PbI_3$ Perovskite Solar Cells Employing Nanostructured p-Type NiO Electrode Formed by a Pulsed Laser Deposition. *Adv Mater*. 2015;27(27):4013-4019. doi:10.1002/adma.201500523

85. Zhao L, Su G, Liu W, et al. Optical and electrochemical properties of Cu-doped NiO films prepared by electrochemical deposition. *Appl Surf Sci*. 2011;257(9):3974-3979. doi:10.1016/j.apsusc.2010.11.160

86. Abzieher T, Moghadamzadeh S, Schackmar F, et al. Electron-Beam-Evaporated Nickel Oxide Hole Transport Layers for Perovskite-Based Photovoltaics. *Adv Energy Mater*. 2019;9(12):1802995. doi:10.1002/aenm.201802995

87. Aydin E, Troughton J, De Bastiani M, et al. Room-Temperature-Sputtered Nanocrystalline Nickel Oxide as Hole Transport Layer for p–i–n Perovskite Solar Cells. *ACS Appl Energy Mater*. 2018;1(11):6227-6233. doi:10.1021/acsaem.8b01263

88. Islam MB, Pant N, Yanagida M, Shirai Y, Miyano K. Effect of hydroxyl groups in NiO_x on the open circuit voltage of lead iodide perovskite solar cells. In: *Japanese Journal of Applied Physics*. Vol 57. Japan Society of Applied Physics; 2018. doi:10.7567/JJAP.57.08RE06

89. Lee JH, Noh YW, Jin IS, Park SH, Jung JW. Facile Surface Engineering of Nickel Oxide Thin Film for Enhanced Power Conversion Efficiency of Planar Heterojunction Perovskite Solar Cells. *ACS Sustain Chem Eng*. 2019;7(18):15495-15503. doi:10.1021/acssuschemeng.9b03148

90. Chen W, Zhou Y, Wang L, et al. Molecule-Doped Nickel Oxide: Verified Charge Transfer and Planar Inverted Mixed Cation Perovskite Solar Cell. *Adv Mater*. 2018;30(20):1800515. doi:10.1002/adma.201800515

91. Han W, Ren G, Li Z, Dong M, Liu C, Guo W. Improving the performance of perovskite solar cells by surface passivation. *J Energy Chem*. doi:10.1016/j.jechem.2019.11.004

92. Cheng Y, Li M, Liu X, et al. Impact of surface dipole in NiOx on the crystallization and photovoltaic performance of organometal halide perovskite solar cells. *Nano Energy*. 2019;61:496-504.

doi:10.1016/j.nanoen.2019.05.004

93. Wang T, Xie M, Abbasi S, Cheng Z, Liu H, Shen W. High efficiency perovskite solar cells with tailorable surface wettability by surfactant. *J Power Sources*. 2020;448. doi:10.1016/j.jpowsour.2019.227584

94. Xue Q, Bai Y, Liu M, et al. Dual Interfacial Modifications Enable High Performance Semitransparent Perovskite Solar Cells with Large Open Circuit Voltage and Fill Factor. *Adv Energy Mater*. 2017;7(9):1602333. doi:10.1002/aenm.201602333

95. Głowienka D, Zhang D, Di Giacomo F, et al. Role of surface recombination in perovskite solar cells at the interface of HTL/$CH_3NH_3PbI_3$. *Nano Energy*. 2019. doi:10.1016/j.nanoen.2019.104186

96. Koç M, Soltanpoor W, Bektaş G, Bolink HJ, Yerci S. Guideline for Optical Optimization of Planar Perovskite Solar Cells. *Adv Opt Mater*. 2019;7(23):1900944. doi:10.1002/adom.201900944

97. Manders JR, Tsang S-W, Hartel MJ, et al. Solution-Processed Nickel Oxide Hole Transport Layers in High Efficiency Polymer Photovoltaic Cells. *Adv Funct Mater*. 2013;23(23):2993-3001. doi:10.1002/adfm.201202269

98. Preda I, Mossanek RJO, Abbate M, et al. Surface contributions to the XPS spectra of nanostructured NiO deposited on HOPG. *Surf Sci*. 2012;606(17-18):1426-1430. doi:10.1016/j.susc.2012.05.005

99. Soriano L, Preda I, Gutiérrez A, Palacín S, Abbate M, Vollmer A. Surface effects in the Ni 2p x-ray photoemission spectra of NiO. *Phys Rev B - Condens Matter Mater Phys*. 2007;75(23). doi:10.1103/PhysRevB.75.233417

100. Hwang J-D, Chen H-Y, Chen Y-H, et al. *The Influence of Defects on the Ni 2p and O 1s XPS of NiO Related Content Recent Citations The Influence of Defects on the Ni 2p and 0 1s XPS of NiO*. Vol 4.; 1992.

101. Chen W, Zhou Y, Chen G, et al. Alkali Chlorides for the Suppression of the Interfacial Recombination in Inverted Planar Perovskite Solar Cells. *Adv Energy Mater*. 2019;9(19):1803872. doi:10.1002/aenm.201803872

102. Chen SC, Kuo TY, Lin YC, Lin HC. Preparation and properties of p-type transparent conductive Cu-doped NiO films. In: *Thin Solid Films*. Vol 519. ; 2011:4944-4947. doi:10.1016/j.tsf.2011.01.058

103. He Q, Yao K, Wang X, Xia X, Leng S, Li F. Room-Temperature and Solution-Processable Cu-Doped Nickel Oxide Nanoparticles for Efficient Hole-Transport Layers of Flexible Large-Area Perovskite Solar Cells. *ACS Appl Mater Interfaces*. 2017;9(48):41887-41897. doi:10.1021/acsami.7b13621

104. Zhang YD, Zhao L. Enhanced electroluminescence performance of all-inorganic quantum dot light-emitting diodes: A promising candidate for hole

transport layer of Cu-doped NiO nanocrystals. *J Mater Res*. 2019;34(16):2757-2764. doi:10.1557/jmr.2019.130

105. Razza S, Di Giacomo F, Matteocci F, et al. Perovskite solar cells and large area modules (100 cm2) based on an air flow-assisted PbI_2 blade coating deposition process. *J Power Sources*. 2015;277:286-291. doi:10.1016/j.jpowsour.2014.12.008

106. Longo G, Momblona C, La-Placa M-G, Gil-Escrig L, Sessolo M, Bolink HJ. Fully Vacuum-Processed Wide Band Gap Mixed-Halide Perovskite Solar Cells. *ACS Energy Lett*. 2018;3(1):214-219. doi:10.1021/acsenergylett.7b01217

CURRICULUM VITAE

PERSONAL INFORMATION

Surname, Name	: Soltanpoor, Wiria
Nationality	: Iranian (IR)
Date and Place of Birth	: 21 March 1985, Oroumieh
Phone	: +90 5395142679
E-mail	: wiria.soltanpoor@metu.edu.tr

EDUCATION

MS	University of Mohaghegh Ardabili University, Theoretical Physics	2011
BS	Urmia University Nuclear Physics	2008
High School	Shahid Chamran, Urmia	2003

WORK EXPERIENCE

Year	Place	Enrollment
2004-2012	J.D.L.I Urmia	English Teacher

FOREIGN LANGUAGES

Advanced English, Pre-intermediate Spanish, Fluent Persian, Fluent Kurdish, Fluent Azeri, Fluent Turkish.

PUBLICATIONS

1. Mehmet Koç, Wiria Soltanpoor, Gence Bektaş, Henk J. Bolink, Selcuk Yerci, "Guideline for Optical Optimization of Planar Perovskite Solar Cells", Advanced Optical Materials, 7(23), 1900944 (2019).

2. Azin Babaei, Wiria Soltanpoor, Maria A. Tesa-Serrate, Selcuk Yerci, Michele Sessolo, Henk J. Bolink, "Preparation and Characterization of Mixed Halide $MAPbI_{3-x}Cl_x$ Perovskite Thin Films by Three-Source Vacuum Deposition", Energy Technology, 1900784, 2019.

3. Wiria Soltanpoor, Chris Lennart Dreessen, Mehmet Cem Şahiner, Isidora Susic, Amir Zarean Afshord, Vladimir Chirvony, Pablo P. Boix, Görkem Günbaş, Selçuk Yerci, Henk J. Bolink, "Hybrid vapor-solution sequentially deposited mixed-halide perovskite solar cells" under submission.

4. Sohrab Behnia, Amin Jafari, Wiria Soltanpoor and Okhtay Jahanbakhsh, "Nonlinear transitions of a single spherical cavitation bubble", Chaos, Solitons & Fractals, 41(2), 30 July 2009, Pages 818-828. (Science Direct Top 25 Hottest Articles)

5. Sohrab Behnia, Amin Jafari Sojahrood, Wiria Soltanpoor and Okhtay Jahanbakhsh "Suppressing chaotic oscillations of a spherical cavitation bubble through applying a periodic perturbation", Ultrasonics Sonochemistry, 16(4), 2009, 502-511.

6. Sohrab Behnia, Amin Jafari, Wiria Soltanpoor and Leila Sarkhosh, "Towards classification of the bifurcation structure of a spherical cavitation bubble", Ultrasonics, 49(8), December 2009, Pages 605-610.

7. Sohrab Behnia, Amin Jafari, Wiria Soltanpoor and, Okhtay Jahanbakhsh "Feasibility of controlling nonlinear oscillations of a spherical cavitation bubble", In: Proceedings of the 9th International Conference on Motion and Vibration Control (MOVIC) 2008, Munich 15-18. September 2008, paper ID. 1220, (10 pages).

8. Sohrab Behnia, Peyman Ayubi, Wiria Soltanpoor "Image Encryption Based on Quantum Chaotic Map and FSM Transforms", In Telecommunications Network Strategy and Planning Symposium (NETWORKS), 2012 XVth International, Rome 15-18 October 2012, (6 pages)

HOBBIES

Fitness, Reading, Swimming, Photography.